Integrating Methods for Characterizing the Passive Treatment of Mercury and Selenium in Groundwater and Sediment

by

Blair Donald Gibson

A thesis
presented to the University of Waterloo
in fulfilment of the
thesis requirement for the degree of
Doctor of Philosophy
in Earth Sciences

Waterloo, Ontario, Canada, 2011

Author's Declaration

I hereby declare that I am the sole author of this thesis. This is a true copy of the thesis, including any required final revisions, as accepted by my examiners.

I understand that my thesis may be made electronically available to the public.

Abstract

Standard geochemical analysis methods, such as aqueous geochemistry analysis and mineralogical analysis, frequently are utilized to evaluate the effectiveness of passive treatment systems, though they do not necessarily provide information regarding the mechanism of removal. Two emerging analytical techniques have shown promise by providing additional information to improve characterization of treatment systems: X-ray absorption spectroscopy (XAS) and stable isotope analysis. In this thesis, these novel analytical techniques were integrated with standard geochemical measurements to better characterize contaminated sites as well as potential treatment technologies used to mitigate aqueous contaminant mobility.

Laboratory experiments were used to evaluate the removal of Se(VI) form simulated groundwater using granular Fe^0 (GI) and organic carbon (OC). Greater than 90 % removal of Se(VI) was observed for systems containing GI after 5 days of reaction time and only 15 % removal was observed in systems containing OC. Synchrotron radiation-based XAS analysis of the treatment materials indicated the presence of both Se(IV) and Se(0) on the edges of GI grains after 6 hours reaction time, with no evidence of oxidized Se after 5 days of reaction.

Several analytical techniques were integrated to characterize sediment contaminated with Hg and other contaminants through previous industrial practices. Analysis of the sediment by XAS indicated the possible presence of mercury selenide and copper sulfide. Resuspension tests were performed in oxic and anoxic conditions to simulate the effects of changing geochemical conditions of Hg release from sediments during dredging operations. The results indicated a higher release of Hg under oxic conditions in some sediment

locations, suggesting that oxidative degradation of organic carbon or oxidative dissolution of Hg sulfides contributed to Hg release.

The treatment of aqueous Hg(II) was evaluated with a variety of treatment media, including clay and GI. Treatment with GI was rapid, with 90 % removal observed after 2 hours reaction time. Extended X-ray absorption fine structure (EXAFS) analysis indicated the presence of Hg-O bonding on GI, suggesting that Hg was bound to Fe oxides formed on the surface of corroded GI.

A new conceptual model for tracking the stable isotope fractionation of sulfur was coupled to the reactive transport model MIN3P to determine the effects of secondary transformations on sulfur cycling in passive treatment systems. Minor differences were noted when comparing the transport model-derived fractionation factor to calculations using a simplified Rayleigh distillation model, possibly indicating the effect of SO_4 precipitation. The incorporation of stable isotope modeling provides a framework for the modeling of other isotope systems in treatment technologies.

Acknowledgements

I thank my co-supervisors Dr. David Blowes and Dr. Carol Ptacek for their support and guidance over the course of my degree, and for providing me with unique opportunities to gain knowledge in the lab and in the field. I also thank my committee members Dr. Shaun Frape and Dr. Vassili Karanassios for their insightful discussions over the years, and Dr. Charlie Alpers for his constructive comments on this thesis. I thank Doug Gould (CANMET) for supplying the thiadiazole compounds used in the mercury treatment experiments.

I also thank Richard Landis, Jim Dyer, Nancy Grosso, and others at the E. I. du Pont de Nemours and Company for helping to support portions of my research project. Laboratory experiments and related analyses were assisted by Shannon Daugherty, Krista Desrochers, Laura Groza, Matt Lindsay, James Tordiff, and Melissa Hollingham, and I am grateful for their help. Special thanks are extended to the remaining members of the research group, including Brenda Bailey, Jeff Bain, Julia Jamieson-Hanes, Corina McDonald, Ashley Stanton and others, for the many lively discussions and for creating an enjoyable atmosphere in which to work.

Dedication

This thesis is dedicated to my wife, Elizabeth, for all of her friendship, love, support, and patience over the years.

Table of Contents

List of Tables

List of Figures

List of Abbreviations

Alk.	Alkalinity (in units of mg L^{-1} of $CaCO_3$)
APS	Advanced Photon Source
ATP	attapulgite
CA	cellulose acetate
CDT	Canyon Diablo Troilite
CV-AAS	cold vapour – atomic absorption spectrometry
CV-AFS	cold vapour – atomic fluorescence spectrometry
DI	deionized
DOC	dissolved organic carbon
DOE	Department of Energy
EPA	Environmental Protection Agency
EXAFS	extended X-ray absorption fine structure
GAC	granular activated carbon
GI	granular iron
GI+OC	granular iron + organic carbon
HR-ICP-MS	high resolution – inductively coupled plasma – mass spectrometry
ICP-OES	inductively couple plasma – optical emission spectrometry
ICP-MS	inductively couple plasma – mass spectrometry
MDL	method detection limit
MRL	method reporting limit
N/A	not analyzed

N/D	not detected
OC	organic carbon
O/R	over range
PRB	permeable reactive barrier
PTFE	polytetrafluroethylene
PZE	point of zero energy
QA/QC	quality assurance/quality control
RPD	relative percent difference
RSD	relative standard deviation
RSS	residual sum of squares
SRB	sulfate reducing bacteria
SeRB	selenate reducing bacteria
SPLP	synthetic precipitation leaching procedure
TOC	total organic carbon
TKN	total Kjeldahl nitrogen
TP	total phosphorus
XANES	X-ray absorption near edge structure
XAS	X-ray absorption spectroscopy
XRD	X-ray diffraction
XRF	X-ray fluorescence

Chapter 1:

Introduction

1.1 Background

Anthropogenic activities including mining operations, chemical manufacturing, and agricultural practices can lead to extensive contamination of groundwater, soils, and sediments. There have been several cases of Hg contamination in lakes and rivers due to industrial practices. A prominent case of Hg sediment contamination involved the Chisso Corporation in Minamata, Japan. The company used mercury sulfate as a catalyst in the production of acetaldehyde. A change in production practices resulted in the formation of methylmercury (CH_3Hg) in the waste stream, and a common practice for the company was to release waste products into the nearby bay. This resulted in the widespread release of CH_3Hg into the surrounding water and sediment (Tsuda et al., 2009). In 1956, residents in the area displayed symptoms of an unknown neurological disorder that was eventually linked to the ingestion of Hg-contaminated fish. Several hundred people died as a result of Hg poisoning and several thousand more suffered chronic health effects. Analysis of the sediment near the plant found Hg concentrations as high as 2000 $\mu g\ g^{-1}$. (Tomiyasu et al., 2006). Mercury compounds were manufactured in the early part of the 1900's as a high explosive used in primers and blasting caps. There are now several cases of Hg contamination near or adjacent to these manufacturing facilities.

The East Fork Poplar Creek floodplain in Oak Ridge, TN, was contaminated due to releases from a nearby weapons manufacturing facility that utilized elemental Hg to separate Li isotopes for nuclear weapons. Barnett et al. (1995) measured Hg concentrations in the floodplain soils of 438 μg g^{-1}. Mining operations may also release Hg to the environment. A now inactive Hg and S mine in Clearlake Oaks, CA, was estimated to have contributed > 100000 kg of Hg to a local lake ecosystem between 1873 and 1957. Remediation efforts have reduced this contribution to approximately 300 kg Hg annually (Suchanek et al., 2009).

Anthropogenic activities in geological regions containing naturally elevated concentrations of toxic elements can sometimes lead to human health issues. Soils derived from marine sedimentary rocks may contain high levels of Se, and irrigation in these areas can result in Se release to groundwater and drainage waters (Seiler, 1995). Although Se is an important cofactor in the production of antioxidant enzymes, it is toxic to mammals, fish, and bird wildlife in large doses (Plant et al., 2003). Selenium is chemically similar to S and thus is typically found in environments where S is common, such as sulfide-bearing rocks. Mine tailings impoundments often contain sulfide-rich minerals such as pyrite [FeS_2] and pyrrhotite [$Fe_{1-x}S$], in addition to other metal-bearing sulfides *e.g.*, sphalerite [ZnS], galena, [PbS], arsenopyrite [FeAsS], and cinnabar [α-HgS]. When pyrite is exposed to water and air, the sulfide-mineral oxidation reaction produces aqueous H^+, which causes a decrease in pH and the increased mobilization of other potentially harmful metals (Blowes et al., 2003). As Se is often associated with S, the oxidation of sulfide-bearing minerals often leads to the release of Se (Howard III, 1977).

1.2 Treatment Strategies for Hg and Se Contamination

1.2.1 General Treatment Strategies

Contaminated source zones in soil or sediment can occur through anthropogenic causes (e.g., the continued spill of a contaminant over time) or natural causes (e.g., naturally occurring soil/sediment with high levels of toxic elements). Ground or surface water flow conditions can enhance the migration of the contaminant, producing lower concentration plumes of much higher mobility. Treatment technologies can be characterized as "active" or "passive" (Johnson and Hallberg, 2005). Active treatment systems require continual monitoring and addition of reagents to remove contaminants through sorption or precipitation mechanisms, and may require continual pumping of groundwater for subsequent treatment at the surface. Passive systems allow for natural surface or groundwater conditions to be re-established as the contaminated water passes through treatment media, or as natural groundwater passes through chemically amended soil or sediment. A permeable reactive barrier (PRB) is a passive system that is placed in the path of a contaminated groundwater plume and is often used in the treatment of acid mine drainage and industrial plumes (Blowes et al., 2000). Zero valent iron is a common component in PRBs due to its propensity for oxidation and concomitant reduction and precipitation of dissolved metals that pass through the upstream margin of the barrier. Another common reactive medium used in PRBs is organic carbon (OC), which promotes the growth of bacteria, including denitrifying bacteria (Robertson et al., 2000) and SO_4-reducing bacteria (SRB) (Benner et al., 1999). Acid mine drainage typically contains elevated concentrations of SO_4 derived from the oxidation of sulfide minerals. In the presence of organic carbon as an electron donor, bacteria can utilize SO_4 as an electron acceptor through the following reaction:

(*1.1*) $$2CH_2O_{(s)} + SO_4^{2-}{}_{(aq)} \rightarrow 2HCO_{3(aq)}^{-} + H_2S_{(aq)}$$

This reaction consumes acid through the production of aqueous hydrogen sulfide (H_2S), which can further react with aqueous metals:

(*1.2*) $$Me^{2+}{}_{(aq)} + H_2S_{(aq)} \rightarrow MeS_{(s)} + 2H^{+}{}_{(aq)}$$

At contaminated sites requiring remediation, the selection of an appropriate treatment technology for either source zone or migration zone control depends on both the nature and the extent of the contamination. For very large source zones, such as mine waste sites or contaminated agricultural land, it may be unfeasible to treat the entire source area by removing the contaminant. Rather, treatment strategies may focus on containment strategies or amendments to the soil or sediment to prevent the future migration of the contaminant. Treatment strategies may be more or less effective depending on the nature of the contaminant. Current treatment methods for Se and Hg are summarized further.

1.2.2 Overview of Se Treatment Methods

Due to the low solubility of the reduced forms of Se, treatment methods often involve the reduction of soluble, oxidized Se(VI) or Se(IV) to insoluble and reduced Se(0) and/or Se(-II). This process can be mediated through chemical or biological methods. For biological methods, Se can be metabolized by prokaryotes through a number of different metabolic functions, such as assimilation, detoxification, and respiration (Stolz and Oremland, 1999). Zehr and Oremland

(1987) suggested that SRB can reduce Se(VI) to Se(-II) through respiration since Se acts as an analogue for S, though the contribution of naturally occurring SRB to the cycling of Se(VI) in the environment is unclear as high concentrations of Se(VI) disrupt SRB growth. Hockin and Gadd (2006) investigated the reduction of Se(VI) by sulfate-reducing biofilms intended for use in engineered bioreactor systems, and observed an enzymatic reduction pathway under high initial sulfate concentrations. Several selenium-specific bacterial strains have been isolated that are able to use either Se(VI) as selenate (SeO_4^{2-}) or Se(IV) as selenite (SeO_3^{-}) as terminal electron acceptors for respiration, resulting in reduction to Se(0) or Se(-II) (Oremland et al., 2004; Siddique et al., 2006; Narasingarao and Häggblom, 2007).

Abiotic methods also can be used to remove Se from aqueous systems. Both zero valent iron (ZVI) and partly oxidized forms of Fe have been employed as Se reducing agents. Myneni et al. (1997) observed that the addition of green rust (a mixed Fe(II)-Fe(III) oxide) to aqueous Se(VI) results in reduction to Se(IV) and Se(0). Sasaki et al. (2008a) used a mixture of granular iron, compost, and wood chips in column experiments designed to treat aqueous Se(VI), and observed the formation of Se^0 and an Fe selenide phase (Sasaki et al., 2008b). Zhang et al. (2005) employed ZVI to remove aqueous Se(VI) in open and closed oxic systems, and observed reduction of Se(VI) to Se(IV) by Fe(II) oxidation from ZVI, followed by adsorption of Se(IV) onto Fe oxyhydroxides formed during corrosion of ZVI. Other studies have investigated the removal of aqueous forms of Se through adsorption mechanisms. Balistrieri and Chao (1987, 1990) investigated the use of goethite [FeO(OH)] and amorphous Fe oxyhydroxides to adsorb Se(VI) and Se(IV), and found that Se(IV) adsorbs more strongly than Se(VI) and that the adsorption decreases with increasing pH. Lo and Chen (1997) investigated Se(VI) and Se(IV) adsorption onto an Fe-oxide coated sand and observed an increased

adsorption at lower pH. This was attributed to a higher density of positive surface charge on the iron oxides at low pH, which will attract oxyanions such as SeO_4^{2-} and SeO_3^{2-}.

1.2.3 Overview of Hg Treatment Methods

In contrast to Se, elemental Hg can pose a threat to the environment due to its relatively high vapour pressure. The consequence is that the reduction of Hg(II) to Hg(0) is not necessarily sufficient to minimize future mobility. However, the high vapour pressure can be of practical use in some treatment methods. Thermal treatment methods have been employed to recover Hg from contaminated areas through the generation and collection of Hg vapour. Kucharski et al. (2005) developed a thermal heating chamber to treat Hg contaminated topsoil and used a solution of 2% $KMnO_4$ in 10% H_2SO_4 as an absorber solution for the Hg vapour produced from thermal evaporation. In situ thermal desorption (ISTD) techniques employ both thermal treatment and vacuum systems to remove Hg vapour from contaminated soil without the need for excavation (Chang and Yen, 2006; Kunkel et al., 2006). Navarro et al. (2009) developed a more cost effective thermal desorption system for treatment of Hg contaminated soils that is powered by solar energy.

Groundwater flow barriers can be used to restrict the movement of aqueous Hg in contaminated groundwater. Physical groundwater flow barriers can be used to reduce water flow through the contaminated area. Meschede and Vogelsberger (1995) used a top and bottom cover consisting of layers of concrete and elemental S to prevent aqueous Hg mobilization from contaminated sediment. Chemical or reactive barriers allow for groundwater to flow through the system naturally while acting as a barrier to contaminants in the water. Weisener et al. (2005) demonstrated the use of ZVI to remove aqueous Hg(II) from groundwater through

field column studies. Synchrotron radiation studies of column precipitates suggest that aqueous Hg(II) was removed as an insoluble Hg sulfide phase that was an intermediate between cinnabar [HgS] and metacinnabar [β-HgS]. DeHobre et al. (2006) discussed the field installation of a PRB containing activated carbon and quartz sand to treat a Hg plume with concentrations as high as 1 mg L^{-1}.

Solidification and/or chemical stabilization are techniques used to treat the soil rather than the contaminated aqueous phase (U.S. EPA, 1993). For solidification methods, the soil is mixed with a physical binding agent such as cement, asphalt, or fly ash to bind the contaminated soil for either excavation and off site disposal, or for on site disposal in confined pits. Chemical stabilization involves mixing the soil with reagents that will convert the contaminant of interest to a chemically stable form that is less soluble and less toxic. Zhuang et al. (2003a) investigated the use of ferric chloride ($FeCl_3$) to immobilize Hg-humic/fulvic acid colloids (Hg-HFA) from a site in British Columbia. Hydrolysis of $FeCl_3$ leads to the formation of ferric flocs as $Fe(OH)_3$, which is termed 'ferric sludge'. This sludge has a high adsorption capacity for various metal-colloids such as Hg-HFA, and was used to treat and stabilize several hundred tons of Hg-contaminated soil and Hg-contaminated concrete fines. Zhuang et al. (2003b) also demonstrated the ability of water-soluble lignin derivatives to promote the formation of Hg-HFA colloids in the absence of naturally occurring humic/fulvic acids, followed by stabilization with ferric sludge. Fuhrmann et al. (2002) developed a sulfur polymer stabilization/solidification method to treat soil contaminated by radionuclides and mixed-waste containing mercury. The addition of sulfur polymer cement (SPC) to mixed Hg waste results in the formation of metacinnabar [β-HgS], and the further addition of sodium sulfide nonahydrate ($Na_2S•9H_2O$) as an additive results in the formation of cinnabar.

1.3 Characterization of Passive Treatment Mechanisms

Traditional geochemical measurements are generally employed to determine the effectiveness of passive treatment systems. These include quantitative analysis of both the target contaminant requiring treatment and the bulk water chemistry that may influence the effectiveness of the treatment system (e.g. cations and anions, and other controlling parameters such as pH, Eh, and alkalinity). Although these measurements give information regarding removal rates and the stability of potential species present in the water, they do not necessarily describe the actual pathway of removal where multiple pathways may be present (e.g., removal by adsorption vs. chemical precipitation). In this case, additional analytical techniques are required to gain the required information. Two such techniques that are gaining prominence to delineate contaminant remediation mechanisms are X-ray absorption spectroscopy techniques using synchrotron radiation and stable isotope analyses. These techniques and their applicability to remediation strategies are described in further detail.

1.3.1 Synchrotron Radiation-based X-ray Absorption Spectroscopy

X-ray absorption spectroscopy (XAS) is a technique used to determine the electronic structure of materials. If an atom in its elemental (or zero valent) state either loses an outer shell electron (i.e., becomes oxidized) or gains an outer shell electron (i.e., becomes reduced), the binding energy of the core level electrons will be affected. Generally, the loss of a valence shell electron will cause an increase in binding energy in the core level electrons, causing a shift in the absorption edge to a slightly higher energy. Conversely, the gain of a valence shell electron will cause a decrease in the binding energy and shift the absorption coefficient to slightly lower

energy. The analysis of the absorption edge of a material is referred to as X-ray Absorption Near Edge Structure (XANES), which can be used to characterize the elemental composition of a material through the measured X-ray fluorescence and to determine the oxidation state of the elements present. This type of analysis is useful for determining reaction mechanisms controlling inorganic contaminant removal, especially in the cases where redox changes are an important aspect of a remediation technology.

If X-ray energies well above the absorption edge of an element are applied, the excess energy is absorbed as kinetic energy by the ejected photoelectron. If enough excess energy is applied, the ejected photoelectron will leave the absorbing atom and interact with the nuclei of neighbouring atoms. The result is a scattering effect where the photoelectron interacts with adjacent nuclei and is then re-absorbed by the original atom. The scattering effect produces both constructive and deconstructive interference at the absorbing atom, resulting in a modulation of the observed absorption coefficient that resembles a decaying waveform. The spectrum produced in this high-energy region is referred to as Extended X-ray Absorption Fine Structure (EXAFS). The EXAFS equation describes the spectrum in terms of the sum of all scattering paths of the photoelectron (Sayers et al., 1971; Stern and Heald, 1983):

(*1.4*)
$$\chi(k) = \sum_i \chi_i(k)$$

(*1.5*)
$$\chi_i(k) \equiv \frac{\left(N_i S_0^2\right) F_{eff}(k)}{kR_i^2} \sin\left[2kR_i + \varphi_i(k)\right] e^{-2\sigma_i^2 k^2} e^{\frac{-2R_i}{\lambda(k)}}$$

where: χ_i is the EXAFS contribution from scattering path i

N_i is the number of coordinating atoms or number of identical scattering paths

S_0^2 is a term accounting for the relaxation of the remaining electrons in the absorbing atom due to the missing core electron

F_{eff} is the effective scattering amplitude of the photoelectron

R_i is the half path length of the photoelectron

φ_I is the phase shift of the photoelectron

σ_i^2 is the mean square displacement of the bond length between the absorbing atom and the adjacent atoms

λ is the mean free path of the photoelectron

k is the measured energy as a function of the photoelectron wavenumber

A Fourier transform applied to the EXAFS equation results in peaks at distances equal to the half path length of each scattering path, R_i. The half path length is the distance between the absorbing atom and the scattering atom, and is equivalent to the bond length between the two atoms. The EXAFS region contains information relating to the atomic structure of the absorbing atom, which can be important for determining how a contaminant is removed from groundwater. For example, the EXAFS region for a chemical species adsorbed to clay will be different than a species that is removed from solution through precipitation reactions. Combining the information obtained from the XANES and EXAFS regions can be useful for elucidating treatment mechanisms, as both the oxidation state and chemical form of a contaminant of interest can be determined.

1.3.2 Stable Isotope Ratio Analysis

Mass dependent isotope fractionation occurs when the lighter isotope in a chemical system tends to react faster than the heavier isotope due to a mass dependence on the translational, rotational, and vibrational energies of the molecule. Either equilibrium or kinetic processes control mass dependent fractionation. When an equilibrium reaction occurs, an isotopic exchange reaction will occur concurrently. For example, the evaporation of water can be described by the following reaction:

(*1.8*) $$H_2O_{liq} \leftrightarrow H_2O_{vap}$$

This reaction will result in an isotopic exchange of oxygen isotopes between the two phases as follows:

(*1.9*) $$^{1}H_2{}^{16}O_{liq} + {}^{1}H_2{}^{18}O_{vap} \leftrightarrow {}^{1}H_2{}^{18}O_{liq} + {}^{1}H_2{}^{16}O_{vap}$$

The amount of fractionation can be defined by the fractionation factor, α (Clark and Fritz, 1997):

(*1.10*) $$\alpha = \frac{\left({}^{heavy}X/{}_{light}X\right)_A}{\left({}^{heavy}X/{}_{light}X\right)_B}$$

where: α is the fractionation factor (unitless)

$({}^{heavy}X/{}^{light}X)_A$ is the ratio of heavy to light isotope in phase A

$(^{heavy}X/^{light}X)_B$ is the ratio of heavy to light isotope in phase B

The equilibrium fractionation factor can also be related to the equilibrium constant of the isotope exchange reaction as follows:

(*1.11*) $$\alpha = \left(K^{ex}\right)^{1/n}$$

where: K^{ex} is the equilibrium constant for isotopic exchange

n is the number of atoms exchanged during a reaction

Isotope ratio measurements are typically reported in delta notation (Clark and Fritz, 1997):

(*1.11*) $$\delta^h X = \left(\frac{R_{sam} - R_{std}}{R_{std}}\right) * 10^3$$

where: $\delta^h X$ is the delta value of sample, referenced to the heavy isotope (units of ‰)

R_{sam} is the isotope ratio of heavy to light isotopes in the sample

R_{std} is the isotope ratio of heavy to light isotopes in the standard

The purpose of the delta notation is to give a standard method for reporting isotope ratios in different samples. A delta value of 0 shows that there is no enrichment of the heavy isotope in the sample relative to the standard; thus no fractionation is occurring. If $\alpha > 1$, then $\delta^h X$ measured in phase A will be larger than the $\delta^h X$ measured in phase B.

Kinetic fractionation occurs when there is a kinetic control on the reaction, such as in fast, incomplete, or irreversible reactions. Typically, the product formed during the initial reaction is removed from the sample pool through further precipitation or losses from evaporation. As a result, reverse isotopic exchange does not occur and the measured fractionation tends to be larger. Since the sample pool is continually decreasing, this process can be defined by a Rayleigh distillation process. In this case, the relationship between the isotope ratios and the kinetic fractionation factor is as follows (Clark and Fritz, 1997):

(*1.12*)
$$\frac{R}{R_0} = f^{(\alpha-1)}$$

where: R is the isotope ratio at any point in time

R_0 is the isotope ratio in the initial sample pool

f is the fraction of reactant remaining (between 0 and 1)

α is the kinetic fractionation factor

For kinetic fractionation, the alpha factor is related to the ratio of the reaction rate constants of the two isotopes:

(*1.13*)
$$\alpha = \frac{k_{heavy}}{k_{light}}$$

where: k_{heavy} is the rate constant for the heavy isotope

k_{light} is the rate constant for the light isotope

Kinetic alpha values are typically less than unity, indicating that the rate constant for the lighter isotope is larger than the heavy isotope and thus reacts faster.

In passive treatment studies where reactions are typically kinetically controlled, isotope ratio measurements may help determine what processes are controlling contaminant removal. Bacterially mediated SO_4 reduction occurring in nature is known to induce a fractionation in $^{34}S/^{32}S$ isotopes (Habicht and Canfield, 1997), and this fractionation has also been observed in PRB treatment studies engineered to promote SRB activity (Waybrant et al., 2002; Lindsay et al., 2009; Guo and Blowes 2009). Tracking the change in $^{34}S/^{32}S$ isotopes during treatment studies may help to monitor the activity of SRB and track the reaction progress.

1.4 Research Objectives

The purpose of this thesis research is to evaluate passive treatment methods using traditional characterization tools in addition to synchrotron-based XAS and stable isotope methods. The overall research objectives are as follows:

- Evaluate the effectiveness of different reactive materials for their ability to treat an artificial groundwater containing Se(VI)
- Characterize a sediment contaminated with Hg and determine the potential for Hg release into the aqueous phase
- Evaluate the effectiveness of different reactive materials for treating an artificial groundwater contaminated with aqueous Hg(II)
- Characterize the solid phase forms of Se and Hg in reactive materials using X-ray absorption near-edge spectroscopy (XANES) and extended X-ray absorption fine structure (EXAFS) techniques

- Incorporate isotope fractionation modeling into the geochemical reactive transport model MIN3P to track the sulfur fractionation occurring in previously performed column treatment experiments

1.5 Thesis Layout

This thesis was written in the form of manuscripts with the intention that each chapter (excluding the introduction and conclusion) will become the basis of a published journal article. Chapter 2 discusses experiments conducted to evaluate the removal of Se from groundwater in contact with a range of solid-phase reactive materials used in PRB systems and the subsequent characterization of the reaction products using X-ray absorption spectroscopy methods. Chapter 3 describes the reaction mechanism leading to release of Hg from lake sediment contaminated with Hg and other elements from legacy industrial activities. Different physical and chemical methods were employed to determine the potential for Hg release into surrounding water during proposed sediment removal practices. X-ray absorption methods were used to assist in the characterization of the form and distribution of Hg, Se, and Cu in these sediments. Chapter 4 describes an investigation of the treatment of a simulated groundwater containing aqueous Hg(II). Characterization of the Hg bound to the reactive materials was achieved with X-ray absorption methods. Chapter 5 investigates the addition of stable isotope fractionation to a geochemical reactive transport model. This chapter focuses on modeling the stable isotopes of S in previous column studies that used organic carbon to promote SRB activity as a treatment for simulated acid mine drainage. Finally, Chapter 6 summarizes the conclusions reached from each chapter and gives recommendations for future work. As some of the target journals do not allow for a conclusions section in published

papers, a summary is given at the end of the chapter for the benefit of the reader. Additional experimental information pertaining to each chapter, including additional quality assurance/quality control (QA/QC) data where available, may be found in the Appendix

Chapter 2:

Removal of Selenate from Groundwater by Granular Iron and Organic Carbon: A XANES Study

2.1 Executive Summary

The treatment of aqueous Se(VI) from a simulated groundwater by granular zero valent iron (GI), organic carbon (OC), and a mixture of these reactive materials (GI-OC) was evaluated in laboratory batch experiments. The experiments were performed under anaerobic conditions to simulate subsurface treatment of groundwater. Simulated groundwater used for the experiments contained 300 mg L^{-1} of Se(VI) as SeO_4^{2-}. After 120 h, concentrations of Se decreased by more than 90% in the system containing GI, whereas 15% Se removal was observed in the OC system and 35% removal was observed for the GI-OC mixture. Analysis of the materials after contact with Se using synchrotron-radiation based X-ray absorption near edge structure (XANES) spectroscopy indicated the presence of both Se(IV) and Se(0) on the margins of GI grains after 6 h, whereas Se(VI) was not observed at that time. After 72 h, Se(0) was the only form of Se present in the GI experiments. In the OC system, the XANES analysis indicated binding consistent with sorption of aqueous Se(VI) onto the OC with only minor reduction to Se(IV) and Se(0) after 120 h. Selenium K-edge XANES spectra collected for the GI-OC mixture were consistent with spectra for Se(IV) and Se(0) on both the margins of granular iron grains and carbon-bearing particles, suggesting that the presence of dissolved Fe may have mediated the reduction of sorbed Se(VI).

2.2 Introduction

Selenium is an essential trace element required for the production of glutathione peroxidase enzymes in mammals, though it is toxic in larger amounts. The range between essential and toxic concentrations in humans is narrow; < 40 μg d^{-1} will result in Se deficiency whereas > 400 μg d^{-1} can be toxic (WHO, 1996). Contamination of water resources by Se may result from

natural processes (e.g., weathering of seleniferous rocks) or anthropogenic activities (e.g., combustion of Se-bearing coal and irrigation of seleniferous soil; Shamberger, 1981). Substitution into sulfide minerals is common because Se is strongly chalcophilic (Plant et al., 2003), and the oxidation of these minerals may contribute to increased concentrations of Se in groundwater systems. Drinking water limits for Se range from 10 μg L^{-1}, as recommended by the World Health Organization and adopted by Australia, Japan and Canada, to 50 μg L^{-1} as mandated by the U.S. EPA (U.S. EPA, 2009). Selenium occurs in four stable oxidation states (i.e., -2, 0, +4 and +6) and in several organic forms. The reduced forms of Se, either Se(-II) or Se(0), exhibit very low solubilities and are stable under anoxic conditions in the subsurface. Oxidized forms of Se commonly occur as aqueous species and thus are more mobile and potentially more toxic. The development of systems for effective remediation of groundwater contaminated by Se is essential for limiting potential impacts on human and ecosystem health.

Treatment of water contaminated by Se has been evaluated using a variety of (bio)geochemical processes. Some approaches are based on promotion of adsorption reactions onto amorphous Fe(III) hydroxide and Mn(IV) dioxide (Balistrieri and Chao, 1990) or Fe(III) oxide coated sand (Lo and Chen, 1997) to control aqueous Se concentrations. These studies demonstrated that adsorption of aqueous Se(VI) is less effective than Se(IV). The reduction of Se(VI) to Se(0) or Se(-II) may be achieved via biological or abiotic mechanisms. Formation of these forms of Se is favorable as they exhibit low solubility and generally remain stable under anaerobic conditions (Masscheleyn et al., 1990). Due to the chemical similarity of Se(VI) and S(VI), sulfate-reducing bacteria are capable of directly utilizing small amounts of Se(VI) as an alternate electron acceptor for anaerobic respiration (Zehr and Oremland, 1987; Nelson et al., 1996; Hockin and Gadd, 2003). Selenate-reducing bacteria also may contribute to reduction of

oxidized forms of Se in natural systems (Oremland et al., 1989; Stolz and Oremland, 1999; Siddique et al., 2006; Narasingarao and Häggblom, 2007). Unlike sulfate reduction, Se(VI) reduction coupled with Fe(II) oxidation has been demonstrated using Fe(II,III) (oxy)hydroxides to generate Se(IV) and/or Se(0) (Myneni et al., 1997; Hayashi et al., 2009). The anaerobic corrosion of GI has been shown to generate Fe(II, III) (oxy)hydroxides, which can in turn facilitate Se(VI) reduction (Zhang et al., 2005; Zhang and Frankenberger Jr., 2006).

Effective treatment of groundwater contaminated by Se requires that conditions favorable to selenate reduction are generated. However, studies that evaluate treatment of aqueous Se(VI) under anaerobic conditions are limited. Sasaki et al. (2008a) conducted laboratory column experiments to evaluate anaerobic treatment of Se(VI) in acid mine drainage using reactive materials commonly employed in permeable reactive barriers (PRBs). They reported mass removal of 95% after 1 week and > 99.9% removal after 1 month using a mixture of granular iron, leaf compost, sawdust, and wood chips. Analysis of the reaction products by X-ray photoelectron spectroscopy and scanning electron microscopy showed evidence of Se(0) and an iron selenide phase, which may have been FeSe or $FeSe_2$ (Sasaki et al., 2008b).

In the current study, batch experiments were employed to evaluate removal of aqueous Se(VI) under anaerobic conditions using granular iron (GI), organic carbon (OC), and a mixture of these reactive materials (GI-OC). Synchrotron-radiation based micro-X-ray fluorescence (μ-XRF) and micro-X-ray absorption (μ-XAS) techniques were used to characterize the reaction products. These techniques can provide information on the distribution and chemical form of Se, and may be used to gain insight into mechanisms of Se(VI) removal in passive anaerobic conditions.

2.3 Materials and Methods

2.3.1 Anaerobic Batch Experiments

Rates and mechanisms of Se(VI) treatment in simulated groundwater were evaluated through a series of anaerobic batch experiments. These experiments examined Se removal using GI and OC, which are commonly used as reactive materials in PRBs. The input solution consisted of a mixture of 1000 mg L^{-1} sulfate (SO_4^{2-}) and 300 mg L^{-1} selenate (SeO_4^{2-}) prepared by dissolving Na_2SO_4 and Na_2SeO_4 in $Ar_{2(g)}$-purged and $CaCO_3$-saturated deionized water. Three sets of reactive material were used: granular iron (GI; Connelly-GPM, Inc., Chicago, IL), organic carbon (OC; composted leaf mulch, Region of Waterloo Landfill, Waterloo, ON), and a 1:1 (w/w) mixture of granular iron and organic carbon (GI-OC). The OC material consisted of a 50:50 w/w mixture of leaf mulch and sawdust. The leaf mulch and sawdust were prepared by grinding and sieving to between 500 and 250 μm (35 to 60 mesh). The GI was sieved between 1000 and 500 μm (18 to 35 mesh), and oxidation products on the iron surfaces were removed prior to use by washing with 6 M hydrochloric acid followed by 1 M hydroxylamine hydrochloride and three rinses with 18 MΩ cm deionized water.

The batch mixtures consisted of 10 g of reactive material and 100 mL of input solution. Six serum bottles were used for each set of reactive materials. An additional 1g of creek sediment, collected from the anaerobic zone of a local creek (Laurel Creek, Waterloo, ON), was added as a microbial source for the mixtures containing organic carbon. The solution and the reactive materials were combined in acid-washed 100 mL amber-glass serum bottles under an inert atmosphere (< 3 vol. % $H_{2(g)}$ balance $N_{2(g)}$) in a glove box (Coy Laboratory Products, USA). These batches were sampled sacrificially to monitor aqueous and solid-phase

geochemistry with time. To prevent exposure to the glove box atmosphere, the serum bottles were sealed with 20 mm butyl-rubber stoppers using Al crimp seals. During the reaction stage of the experiment, the septa were pierced with sterile syringe needles connected to tubing that were vented under water to allow for the venting of gases generated during the experiment.

2.3.2 Water Sampling and Analysis

One bottle from each set was randomly selected and sampled at 6, 24, 48, 72, 96, and 120 h for determinations of pH, Eh, and alkalinity. Measurements of pH were performed with an Orion Ross combination electrode (model 815600, Thermo Fisher Scientific Inc., Waltham, MA) and redox potential was measured using an Orion Pt redox electrode (model 96-78BN, Thermo Fisher Scientific). The pH electrode was calibrated with standard pH 4, 7, and 10 buffer solutions and performance of the redox electrode was checked with ZoBell's solution following the procedure of Nordstrom (1977). Measured redox potentials were corrected to the standard hydrogen electrode and are reported as Eh. These measurements were made in the anaerobic chamber on unfiltered samples immediately following collection, and electrode performance was checked before and after each reading. Subsequent samples were passed through sterile 0.45 μm Acrodisc syringe filters. Alkalinity was determined by titration with a Hach digital titrator using 0.16 N H_2SO_4 and bromocresol green/methyl red indicator. Samples collected for determination of total Se and major cations were acidified to pH < 2 using trace-metal grade HNO_3, and anion samples were not acidified. All samples were refrigerated at 4°C until analysis. Total Se was measured using high resolution-inductively coupled plasma-mass spectrometry (HR-ICP-MS; Thermo Scientific Element2) and concentrations of the major cations (Ca, Mg, Na, Fe) were determined by inductively coupled plasma-optical emission

spectroscopy (ICP-OES; Thermo Scientific iCAP 6000). Blank samples were analyzed between sets of 5 to 6 analyses and analyte signals were corrected by blank subtraction. The concentrations of inorganic anions (Cl, NO_3, SO_4) were determined by ion chromatography (IC; Dionex ED50).

2.3.3 Solid-phase Sampling and Analysis

Solids from batches sampled at 6, 72, and 120 h, were vacuum filtered through 0.45 μm cellulose acetate (CA) membranes (type 111, 50mm; Sartorius Stedim Biotech S.A.) and then vacuum desiccated in the glove box. Samples were prepared as 26 x 46 mm thin sections polished on one side using kerosene to prevent the dissolution of water-soluble phases (Vancouver Petrographics Ltd., Langley, B.C.). Synchrotron-radiation based micro-X-ray fluorescence (μ-XRF) mapping and micro-X-ray absorption near edge structure (μ-XANES) spectroscopy were performed on Beamline 13-BMD-GSECARS at the Advanced Photon Source (APS; Argonne National Laboratory, Argonne, IL). This beamline is equipped with a Si(111) monochromator, 16-element Ge fluorescence detector, incident and transmission ion chambers, and has a working energy range of 7 to 70 keV. A focused beam of 10 x 30 μm and the fluorescence detector were used for μ-XRF and μ-XANES measurements on the thin sections. A defocused beam (10 x 1000 μm) was used to collect XANES spectra for the bulk reference materials in transmission mode. Element distribution maps were obtained by μ-XRF for the GI and OC thin sections collected at 6 and 120 h, and μ-XANES were obtained on spots characterized by elevated Se concentrations. Additional μ-XANES spectra were obtained for all available thin sections, based on locations with elevated fluorescence measurements at the Se Kα emission line, which is located at 11222.4 eV.

Selenium reference compounds were purchased from Sigma-Aldrich and included Na_2SeO_4, Na_2SeO_3, metallic Se^0, Cu_2Se, ZnSe, and SeS_2. Monoclinic (red) Se^0 was synthesized according to previously described methods (Zhang et al., 2005; Combs et al., 1996). This method involved combining 15 mL of a Na_2SeO_3 solution containing 1000 mg Se(IV) L^{-1} and 5 mg of ascorbic acid, and mixing by hand for 60 s to form a red precipitate. This precipitate was recovered by vacuum filtering the solution through a 0.45 μm CA membrane until dry. The precipitate was scraped off the filter paper with a micro-spatula and collected in a 5 mL glass sample vial. Reference materials for X-ray absorption measurements were prepared by applying a thin layer of powdered material between layers of adhesive tape (Scotch® brand Magic™ tape).

2.3.4 Data Analysis

The equilibrium speciation code MINTEQA2 (Allison et al., 1990) was used to assist with the interpretation of the aqueous chemistry measurements. The database was modified to ensure consistency with the WATEQ4F database (Ball and Nordstrom, 1991). The HSe^-/SeO_4^{2-} redox pair was used for Se speciation and to facilitate calculation of saturation indices for mineral phases containing reduced forms of Se.

Processing of XANES data was performed using the program ATHENA, a component of the IFEFFIT software package (Ravel and Newville, 2005). Data quality analysis identified radiation induced reduction of attenuated Se(VI) for samples collected from the OC batches. This phenomenon can occur when chemical species are subjected to ionizing radiation and subsequently undergo chemical reduction. Similar reduction of Se(VI) was not observed on replicates scans of granular iron grains or on the carbon-rich areas in the GI-OC mixtures.

Therefore, all K-edge determinations involving spectra from the OC batches utilized only the initial scan, whereas the replicate spectra were averaged for samples from the GI and GI-OC batches.

2.4 Results and Discussion

2.4.1 Aqueous Geochemistry

Values of pH were observed to increase with time for all three batch mixtures (Fig. 2.1). The mixtures containing organic carbon (OC and GI-OC) showed a rapid initial rise in pH between 7.5 and 7.9 after 6 h, which stabilized at ~8.1 following 120 h reaction time. The pH in the GI mixture increased to pH 8.75 following 120 h reaction time. Values of Eh decreased rapidly in all three mixtures and reducing conditions were maintained throughout the experiments. Minimal variations in alkalinity were observed in the GI batches, whereas relatively large increases were observed for the OC batches. The alkalinity in the GI-OC mixture increased at approximately half of the rate observed in the OC batches. This difference suggests that anaerobic oxidation of organic carbon likely contributed alkalinity to solution.

Sulfate concentrations remained unchanged in the organic carbon (OC) batch, indicating that sulfate-reducing conditions were not established during the experiment. However, sulfate removal was observed for the GI and GI-OC batches. Abiotic sulfate reduction generally does not occur readily; therefore the decrease in sulfate can possibly be attributed to the formation of an Fe hydroxysulfate phase. A similar phase was observed in previous batch treatment experiments containing granular iron (Lindsay et al., 2008). Aqueous Fe concentrations in the GI experiments increased rapidly and then decreased gradually with time. In contrast, the GI-OC mixture exhibited a small initial increase in aqueous Fe and

concentrations measured at subsequent times remained relatively constant. Increases in aqueous Fe(II) concentrations are attributed to anaerobic corrosion of GI (Matheson and Tratnyek, 1994).

Varying amounts of aqueous Se(VI) were removed in the three treatments over the duration of the experiment (Fig. 2.2). A 15 wt. % removal of Se was observed after 6h of treatment with OC. No additional removal was observed at longer reactions times, indicating that the OC had a limited capacity to remove Se. Selenium concentrations in the GI-OC mixture gradually decreased with increasing reaction time, with a 35 wt. % removal observed after 120 h. Concentrations of Se decreased more rapidly in the GI batch and a 92 wt. % removal of Se was observed by the end of the experiment. Rate constants were calculated from the observed aqueous Se concentrations assuming a pseudo-first-order rate law (Fig. 2.3). The rates of Se removal in the Fe-bearing treatments (0.0192 h^{-1} for GI and 0.0032 h^{-1} for GI-OC) were similar to the range of 0.008 to 0.017 h^{-1} reported by Myneni et al. (1997) for the abiotic Se(VI) reduction in the presence of green rust. However, these rates were lower than those reported by Zhang et al. (2005) for the treatment of a 1 mg L^{-1} solution of Se(VI) with Peerless granular iron (40 to 60 mesh) under aerobic conditions. The calculated removal rate in the OC batch was 0.0007 h^{-1}. The Zhang et al. (2005) study reported rates of 0.093, 0.043, and 0.033 h^{-1} for solutions containing 480 mg L^{-1}, 960 mg L^{-1}, and 4800 mg L^{-1} sulfate, respectively. In the current study, the sulfate concentration in the input solution was within the range of those evaluated by Zhang et al. (2005), though the Se(VI) concentration in the current test was much higher at 300 mg L^{-1}. Variations in removal rates between the experiments were likely due to differences in the initial Se(VI) concentration, the particle size and, therefore, surface area, or variations in surface coatings among GI materials.

Masscheleyn et al. (1990) examined Se speciation and solubility in selenium-contaminated evaporation pond sediment under different redox and pH conditions. They reported limited Se mobility under reduced conditions (-200 mV) which they attribute to a solubility control on Se by an FeSe phase. The total dissolved Se was 80-100% Se(-II) and Se(0) under these conditions. Increasing the redox potential resulted in increased concentrations of aqueous Se, as Se(-II) and Se(0) are rapidly converted first to Se(IV) then to Se(VI) following the oxidation of Fe(II)-sulfide phases. Increased Se solubility is observed at elevated redox conditions (450 mV) under both slightly acidic and slightly basic conditions. The adsorption of aqueous Se(IV) and Se(VI) decreases with increasing pH in experiments with soils (Dhillon and Dhillon, 1999; Goh and Lim, 2004) and the presence of Fe(III) and Mn(IV) (oxy)hydroxides (Balistrieri and Chao, 1990; Duc et al., 2006). Under low Eh and slightly alkaline pH conditions observed for the current experiments, the potential for adsorption of Se(IV) or Se(VI) and the overall solubility of Se was expected to be limited.

The initial increase in aqueous Fe concentrations was characteristic of all GI batches and corresponded to decreased SIs for Fe(III)-bearing minerals, such as goethite [FeOOH], hematite [Fe_2O_3] and magnetite [Fe_3O_4] (Fig. 2.4). The water became supersaturated with respect to these minerals with increasing time. In the OC experiments, the water became supersaturated with respect to the Fe(III)-bearing minerals after 3 h, whereas the development of supersaturated conditions was slower for the GI-OC mixture. The water for all batches was either saturated or slightly supersaturated with respect to siderite [$FeCO_3$]. Undersaturation of the water with respect to calcite [$CaCO_3$] and dolomite [$CaMg(CO_3)_2$] was observed for the GI mixture, and likely resulted from limited carbonate alkalinity in these batches. In contrast,

alkalinity production in the presence of OC resulted in saturation of the water with respect to calcite and dolomite.

Saturation indices also were calculated for crystalline and amorphous elemental Se, ferroselite [$FeSe_2$] and FeSe. The formation of ferroselite and FeSe were thermodynamically-favored in all three experiments; however, Se removal generally resulted in decreases in SI values at later times. Saturation with respect to both crystalline and amorphous elemental Se was observed for the input solution. Slight undersaturation of both forms of Se(0) was observed after 6 h in the GI and GI-OC batches, whereas SI values were > 0 in the OC batches throughout the experiments. Declines in SI values were generally correlated with observed declines in total aqueous Se concentrations (Fig. 2.2).

2.4.2 XANES Characterization of Solid Phase Samples

Selenium K-edge energies (E_0) for Se reference materials were determined as the maxima of the first derivative for the absorption spectra (Table 2.1). The spectra for trigonal (grey) and monoclinic (red) elemental Se were shifted to the theoretical value of 12658 eV, and all other spectra were normalized to this value. Micro-XRF maps of the Fe Kα and Se Kα fluorescence lines were obtained for samples collected from the GI batches after 6 h (Fig. 2.5a) and 120 h (Fig. 2.5b). These maps indicated that Se was concentrated at the margins of GI grains, and several locations were selected along these margins for collection of XANES spectra. At 6 h reaction time, the three separate normalized XANES spectra showed either two distinct peaks or one peak at higher energy with a shoulder present at slightly lower energy. The derivative plot showed that these peaks occurred at 12658 eV, indicating the presence of Se(0) or Se(-II), and at 12663 eV indicating the presence of Se(IV). A peak corresponding to Se(VI) was not

observed at these locations. At 120 h reaction time, the two separate normalized XANES spectra exhibited one peak with a Se K-edge value of 12658 eV. The lack of peaks at higher energies indicated that only reduced Se species, Se(0) or Se(-II), were present. The presence of Se(IV) at early reaction time suggests that the removal of aqueous Se(VI) by granular iron suggests a stepwise reaction process involving Se(IV) as an intermediate to the eventual formation of a more reduced form of Se. Although the overlap in Se K-edges between elemental and reduced Se made it difficult to identify the form of Se associated with the Fe oxidation rims, the relatively low solubility of Se in either reduced oxidation state indicates that the precipitate was likely stable under anaerobic conditions.

These results are comparable to similar studies reported in the literature. The anaerobic Se(VI) reduction experiments by Myneni et al. (1997) were performed at pH values of 3.8, 6.8, and 9.3 and Se speciation was characterized by XANES and extended X-ray absorption fine structure (EXAFS) spectroscopy. At pH 3.8, the formation of green rust was not observed and Se(VI) reduction was not observed after 60 h reaction time. The presence of both Se(IV) and Se(0) was observed after 36 h at pH 6.8, and similar results were observed at higher pH values. Zingaro et al. (1997) investigated Se(VI) and Se(IV) removal by Fe(II) hydroxide under alkaline conditions (pH 8.8) and confirmed the presence of metallic grey Se. In the anaerobic conditions present in the current experiments, it is likely that GI promoted the reduction of water to form aqueous Fe(II) and subsequently iron(II) hydroxide or iron(II) hydroxycarbonate through reactions of the form:

(*2.1*) $$\mathrm{Fe^0_{(s)} + 2H_2O_{(l)} \rightarrow Fe^{2+}_{(aq)} + H_{2(g)} + 2OH^-_{(aq)}}$$

(*2.2*) $$Fe^{2+}_{(aq)} + 2OH^{-}_{(aq)} \rightarrow Fe(OH)_{2(s)}$$

The iron(II) hydroxide produced through anaerobic GI corrosion has potential to reduce aqueous Se(VI) to form Se(IV) and Se(0). The likely presence of a Se(IV) intermediate at early times is consistent with results described by Myneni et al.(1997).

Additional μ-XRF maps were obtained on the thin sections from the OC experiments at 6 h (Fig. 2.6a) and 120 h (Fig. 2.6b). At both reaction times, Se appeared to be dispersed throughout OC particles. At 6 h, the normalized XANES spectrum revealed a single Se K-edge peak at 12666 eV. A small shoulder observed at 12663 eV suggests that a minor amount of Se(IV) was present at this time. Multiple Se K-edge peaks were apparent on the normalized XANES spectrum after 120 h. The corresponding derivative plot exhibited a distinct peak at 12658 eV and a broad peak ranging from 12663 to 12666 eV. These results suggest that a reduced form of Se (either Se(0) or Se(-II)), Se(IV) and Se(VI) were present at this location. The mass of Se removed was observed to increase initially, then reach a plateau, suggesting that the Se removal capacity was reached shortly after initiation of the experiment. The absence of improved treatment with increasing reaction time suggests that a mechanism such as Se(VI) absorption onto organic material may have been the primary Se removal mechanism. Subsequent reduction of Se(VI) associated with OC particles did not result in additional decreases in aqueous Se(VI) concentrations. Selenate will compete with sulfate for respiration by sulfate-reducing bacteria, though inhibition of selenate reduction is observed at millimolar or greater levels of selenate or sulfate (Zehr and Oremland, 1987). Selenate reduction also can occur independently of sulfate reduction through respiration by selenate-reducing bacteria (SeRB). Siddique et al. (2006) characterized SeRB in a pond sediment and evaluated the

efficacy of reduction by mixing aqueous selenate with 5 % and 25 % sediment slurry concentrations, both with and without an additional organic carbon source. Both selenate concentrations and redox conditions decreased in the slurries that were amended with organic carbon over the duration of the experiment. Removal of 93 % of the initial selenate was observed after 9 days of incubation in a 5% sediment slurry. Bacterially-mediated reduction of selenate results in the formation of monoclinic (red) Se(0) (Oremland et al., 1989; Roux et al., 2001). In the current experiments, the sharper peak shape of the XANES spectra for the organic carbon batch at 120 h (Fig. 2.6b) appeared to be more consistent with the spectra observed for trigonal (grey) Se(0) than the monoclinic form, suggesting that the reduction mechanism was not likely bacterially mediated. Another factor that may have affected potential bacterial reduction was the relatively large selenate concentrations (300 mg L^{-1}) employed for the current experiments, which could inhibit bacterial activity.

Individual XANES spectra were obtained for the 6, 72, and 120 h samples on the edges of GI and OC particles (Fig. 2.7). XANES spectra collected at the margins of GI particles were similar to those shown in Fig. 2.5. Reduced forms of Se, including Se(0) or Se(-II), and Se(IV) were present after 6 h and less Se(IV) was observed in samples collected at subsequent times. In contrast, the spectra obtained for OC particles in the GI-OC experiments differed from those obtained from similar grains in the experiments containing only organic carbon. The spectra showed varying levels of Se(VI) reduction to Se(IV) and Se(0) or Se(-II), with no evidence of Se(VI). The removal of aqueous Se(VI) was enhanced in the GI batch, either by sorption of Se(VI) followed by reduction to Se(IV), or by reduction of aqueous Se(VI) to Se(IV), followed by sorption onto the organic carbon. Elevated concentrations of Fe(II) in solution may explain

this difference in solid-phase Se speciation on OC particles from the GI-OC mixtures compared the OC batches.

2.4.3 Observation of Radiation-induced Reduction

Apparent radiation-induced reduction was observed on spectra obtained from the OC experiments. During six consecutive scans (~2.3 h total scan time) on the OC material after 6 h reaction time, a decrease is seen on the main peak in the normalized energy plot while a shoulder at lower energy gradually appears and increases in intensity (Fig. 2.8). These peaks correspond to E_0 values at 12666 eV and 12658 eV, respectively, showing the reduction of absorbed Se(VI) directly to Se(0) or Se(-II) with no Se(IV) intermediate. Six consecutive scans on a carbon-rich particle in the GI-OC mixture show no change in intensity at the peaks observed at 12658 eV and 12663 eV, indicating that the presence of organic carbon was likely not the cause of the reduction. Replicate scans obtained on Fe-rich grains in both Fe amended tests (not shown) also remain unchanged.

Zavarin (1999) described synchrotron radiation-induced reduction of Se(VI) to Se(IV) in the presence of $CaCO_{3(s)}$. Little-to-no reduction was observed in samples with no $CaCO_{3(s)}$ present (including the $CaSeO_{4(s)}$ reference standard). Zavarin (1999) hypothesized that the glue from Mylar or Kapton tape was providing an electron source and/or oxygen sink for Se(VI) reduction. Ryser et al. (2006) performed a radiation-induced reduction experiment with Se(VI) and Se(IV) sorbed to goethite and reported rapid reduction of Se(VI) to Se(IV) and elemental Se under Kapton tape and minimal reduction under Mylar film. Minimal reduction of Se(IV) was observed under Kapton tape. In the current experiments, the treatment media was embedded in an epoxy resin and mounted on a glass slide and thus no Kapton or Mylar tape or

film was used. In addition, the Se(VI) sorbed to the organic carbon reduced directly to elemental or reduced Se without evidence of an Se(IV) intermediate. Whereas the mechanism of reduction is unknown, it appears to only affect Se(VI) and not Se(IV). The amount of reduction is also relatively small over the long scans times and thus more rapid scans across the XANES region could potentially be used to obtain multiple scans prior to the onset of radiation induced reduction.

2.5 Conclusions

Concentrations of aqueous Se(VI) decreased in batch systems containing granular iron under anaerobic conditions, with approximately 90 % removal of Se observed after 120 h reaction time. Solid phase analysis of the residual Fe using synchrotron radiation based X-ray fluorescence and absorption techniques showed that Se was present around the edges of the Fe grains. Reduction to both Se(IV) and elemental or reduced Se occurred within a short time period (6 hours) with no indication of adsorbed Se(VI). After 120 h, the major form of Se was elemental or reduced Se, with minor amounts of Se(IV) present. Less effective removal of aqueous Se(VI) was observed in the batch systems containing organic carbon. The removal that was observed initially was rapid, but then reached a plateau at 15 % removal at longer reaction times. Removal was not attributed to respiration by SRB because there was no indication of substantial sulfate reduction over the short duration of the experiment. Solid phase analysis showed that the main form of Se was Se(VI) with very minor amounts of Se(IV). One analysis location on the 120 h sample showed evidence of Se(VI), Se(IV), and elemental/reduced Se. Comparison of the absorption spectra with the reference materials showed that the reduced Se spectra was not consistent with the spectra of monoclinic (red)

Se(0), suggesting that reduction probably was not catalyzed by SeRB. Amendment with carbon mixed with granular iron resulted in ~ 35 % removal after 120 h. Both Se(IV) and elemental/reduced Se were observed on both iron grains and organic carbon particles, indicating that removal of Se(VI) was enhanced in this combined system in the absence of sulfate reducing conditions.

Selenium removal rates were similar to or slightly lower than other treatment studies involving iron under aerobic conditions to induce formation of "green rust". The experiments in the current work were designed to more closely simulate groundwater conditions that are expected to be more anoxic; thus green rust formation was not expected to be significant. However, an observed reduction in sulfate concentrations in abiotic conditions suggests the possible formation of an iron-hydroxysulfate phase.

TABLE 2.1

Se K-edge energies (obtained from maxima of normalized 1st derivative XANES plots) for reference materials.

Standard	Energy (eV)
Na_2SeO_4	12666
Na_2SeO_3	12663
trigonal Se^0 (grey)	12658
monoclinic Se^0 (red)	12658
Cu_2Se	12658
ZnSe	12659
SeS_2	12658

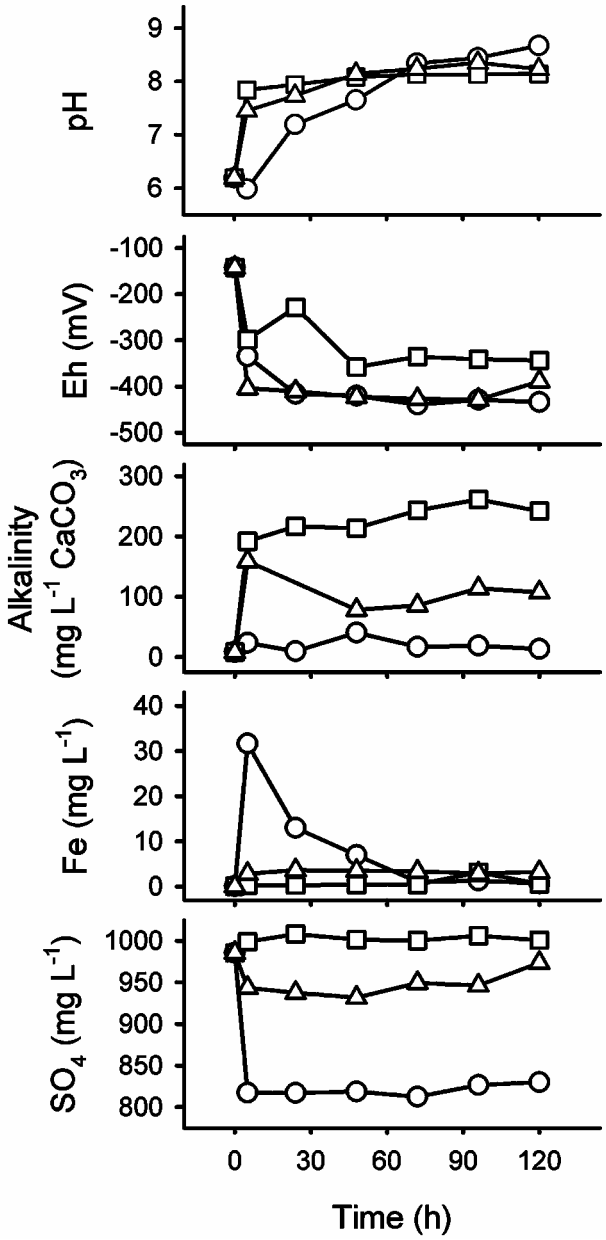

FIGURE 2.1 Geochemistry results versus reaction time for reaction mixtures consisting of granular iron only (○), organic carbon only (□), and a mixture of granular iron and organic carbon (△).

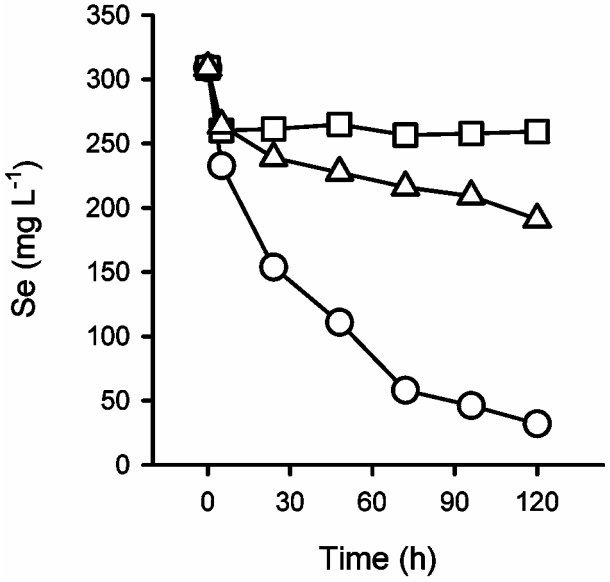

FIGURE 2.2 Comparisons of total selenium concentrations versus reaction time for reaction mixtures consisting of granular iron only (○), organic carbon only (□), and a mixture of iron and carbon (△).

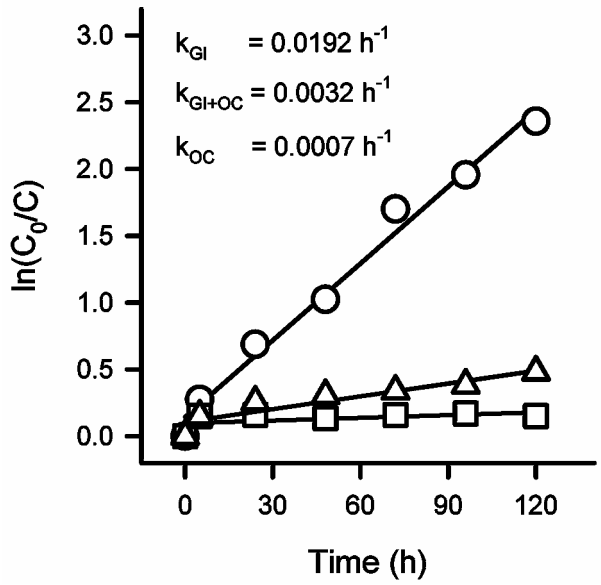

FIGURE 2.3 Rate constant determinations for the granular iron (○), organic carbon (□), and iron and carbon (△) mixtures.

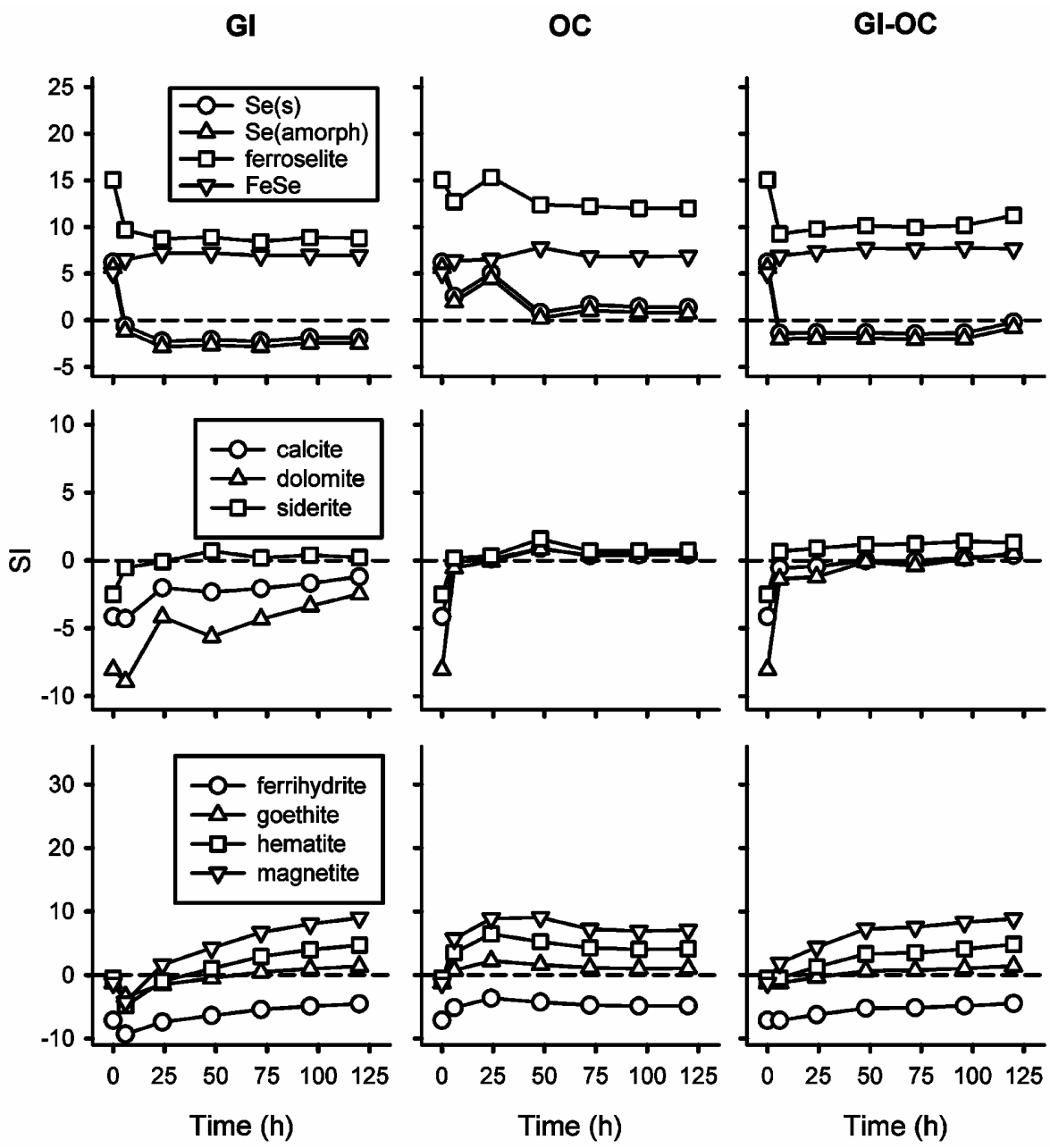

FIGURE 2.4 Saturation indices calculated from MINTEQA2 over time for the three batch treatment experiments; granular iron (GI), organic carbon (OC), and a mixture of iron and carbon (GI-OC).

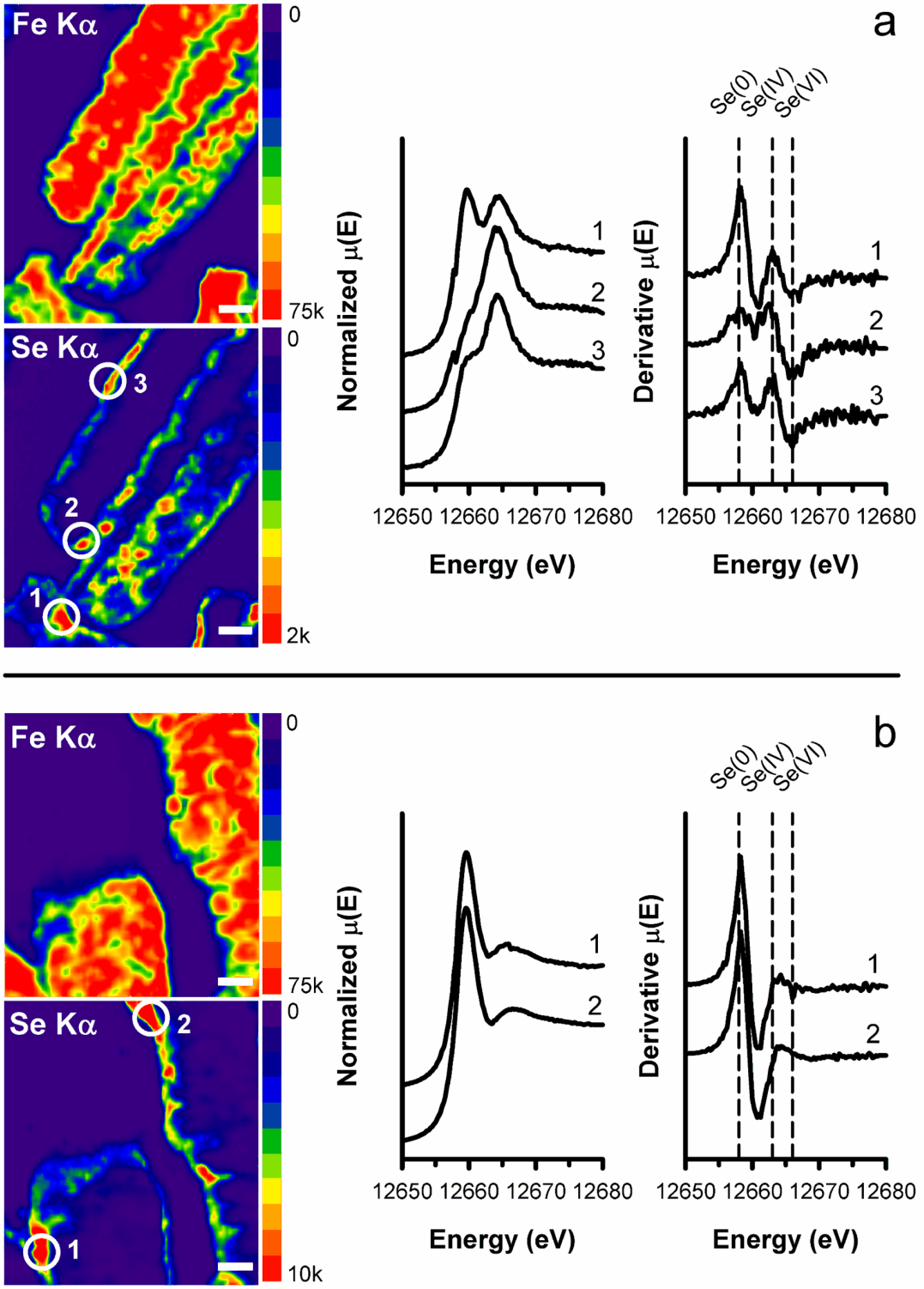

FIGURE 2.5 Micro-XRF maps of Fe and Se Kα in separate granular iron treatment batches after (a) 6 h and (b) 120 h. Scale bars represent 100 μm. Circled spots on Se map correspond to normalized and derivative XANES data. Derivative spectra are compared to K-edge energies obtained from reference spectra.

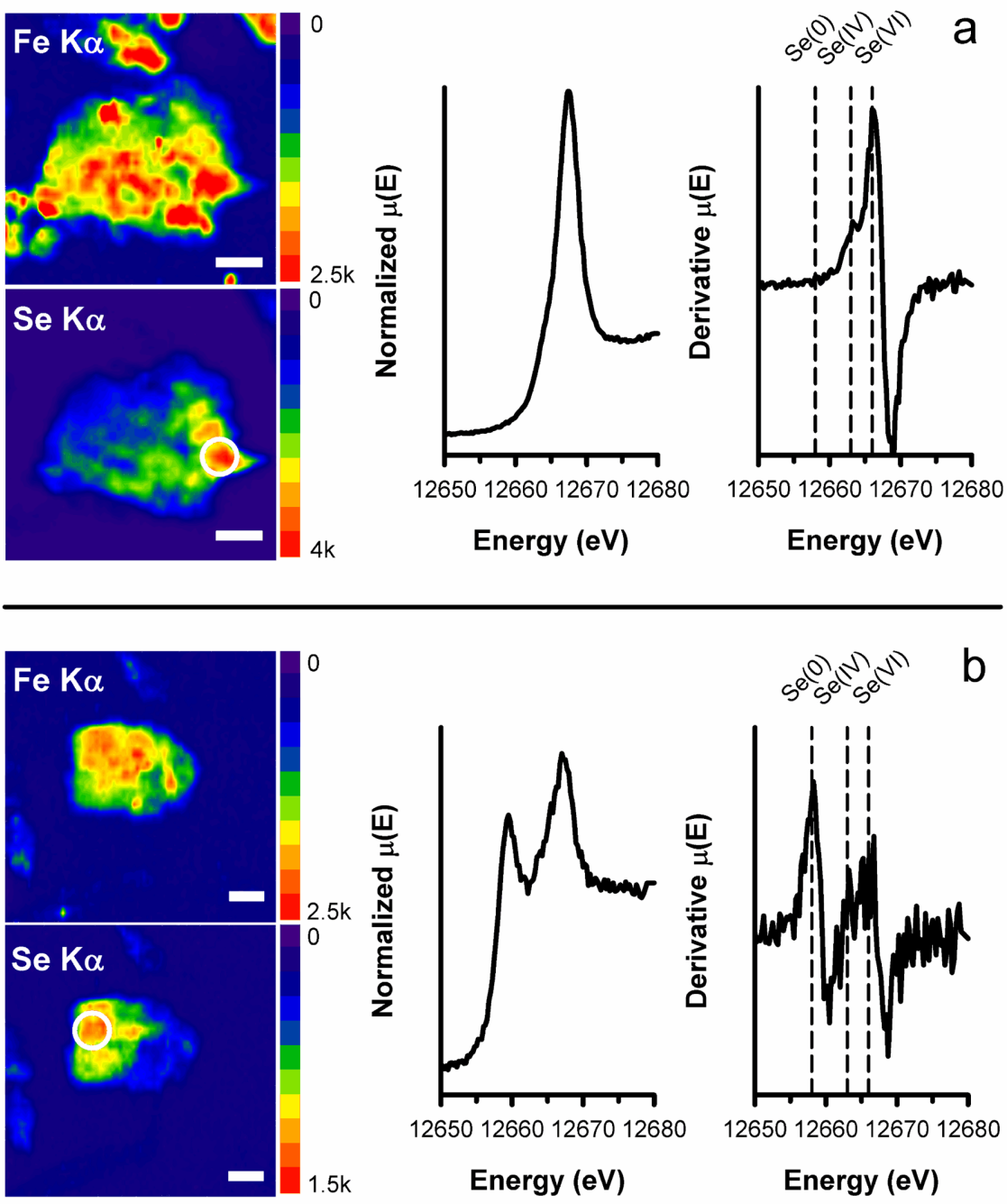

FIGURE 2.6 Micro-XRF maps of Fe and Se Kα in separate organic carbon treatment batches after (a) 6 h and (b) 120 h. Scale bars represent 100 μm. Circled spots on Se map correspond to normalized and derivative XANES data. Derivative spectra are compared to K-edge energies obtained from reference spectra.

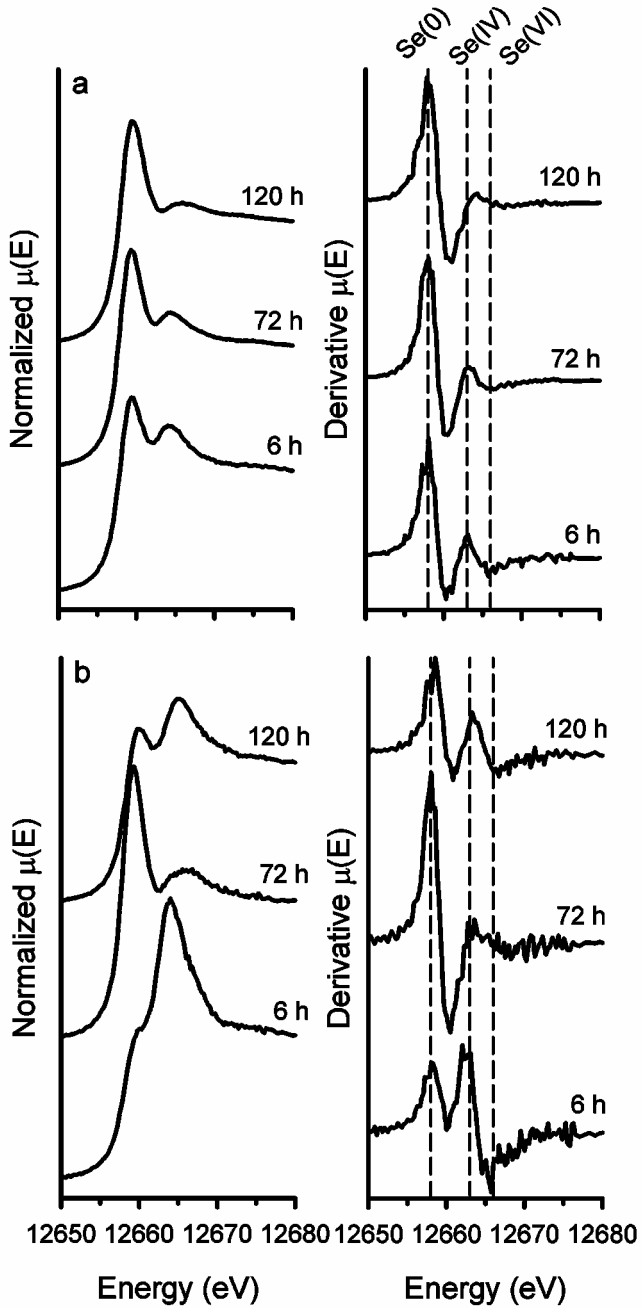

FIGURE 2.7 Normalized and derivative XANES spectra for the iron:carbon mixture treatment at 6, 72, and 120 h reaction times. Spectra were obtained from (a) granular iron (GI) and (b) organic carbon (OC) particles. Derivative spectra are compared to K-edge energies obtained from reference spectra.

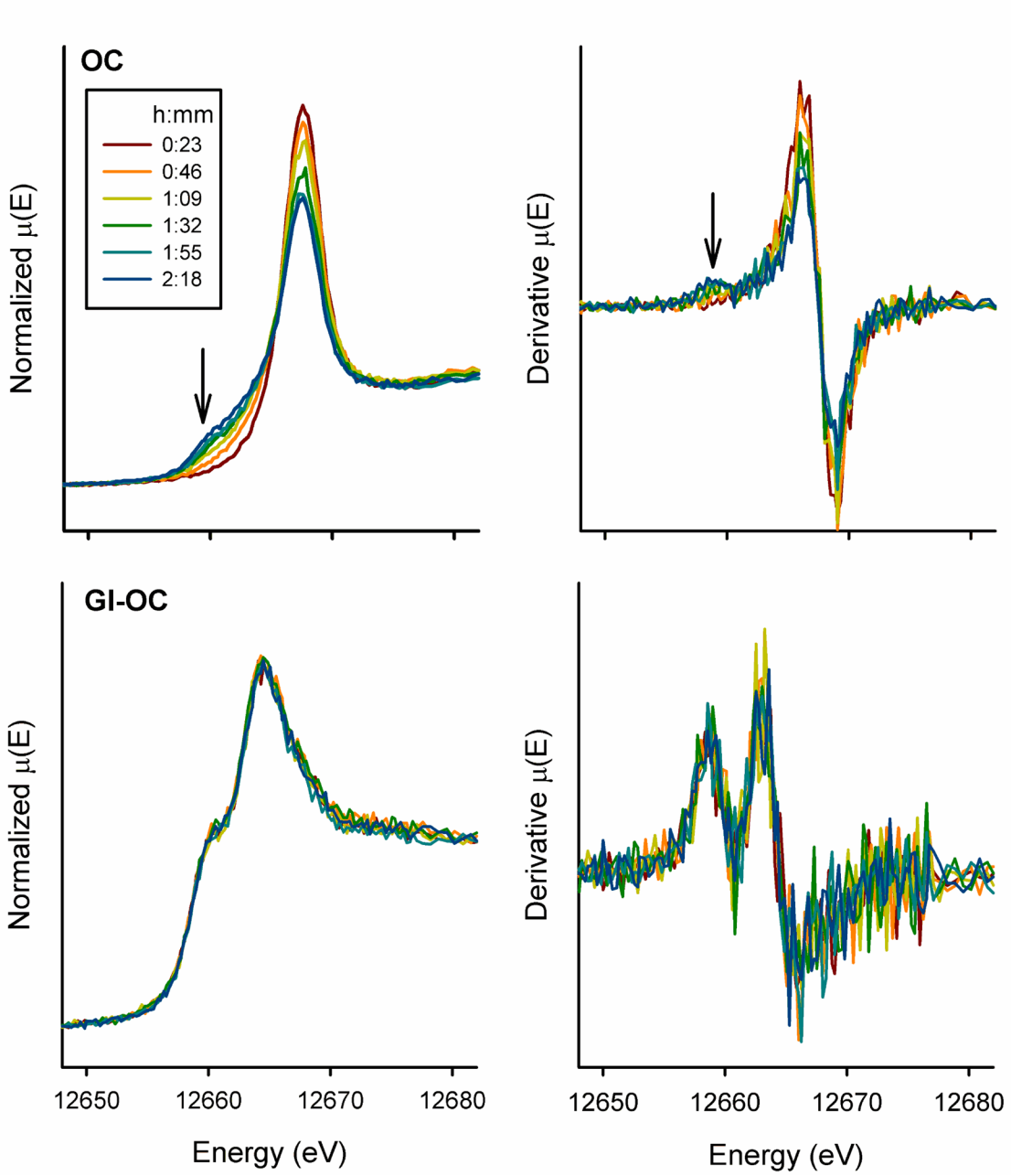

FIGURE 2.8 Replicate XANES spectra obtained over time from carbon-rich particles in the organic carbon (OC) treatment and the granular iron:organic carbon mixture (GI-OC). Evidence of radiation induced reduction of Se(VI) to Se(0) is observed in the carbon only experiment, whereas no reduction of Se(IV) to Se(0) is observed on carbon in the presence of granular iron.

Chapter 3:

Characterization of a Mercury-contaminated Sediment and Implications for Remediation

3.1 Executive Summary

Releases from a legacy manufacturing facility resulted in elevated concentrations of Hg, Pb, and Se in sediments in a nearby freshwater lake. Core samples were taken from locations within the lake and initial physical and chemical properties were obtained through analytical testing procedures including sediment digestion, particle size analysis, and mineralogical analysis. Results indicate that contaminant concentrations are is higher in the regions close to the point of discharge into the lake, with lower concentrations spread out at more distal locations within the lake. Sequential extraction analyses show that Hg is mainly found in a geochemical form of an organo-chelate, Hg^0, or Hg sulfide/selenide, whereas only trace amounts were found as a water or "human stomach acid" soluble form of Hg. Synchrotron-based micro-X-ray absorption near edge spectrometry (μ-XANES) and micro-X-ray fluorescence (μ-XRF) analyses suggest the existence of Hg selenide and show a strong correlation between Hg, Se, and Cu. Resuspension tests were performed under oxic and anoxic conditions to evaluate the effects of air entrainment during a simulated dredging operation. Oxic mixing generally caused a larger release of Hg into solution compared to anoxic mixing, presumably due to the oxidation of Hg-chelates and/or Hg sulfide/selenide. Remedial technologies should avoid excessive resuspension of the sediment to help minimize the release of Hg into the water column.

3.2 Introduction

Mercury (Hg) is a rare element in the Earth's crust, though it tends to be found in concentrated deposits as cinnabar [α-HgS] due to its affinity for binding with sulfur. Mercury can be transported through the environment by natural and anthropogenic means. Natural sources of

Hg include volcanic eruptions and volatilization from oceans, whereas anthropogenic sources include coal combustion, mining, and waste products from industrial practices (Fitzgerald and Clarkson, 1991). The transport and cycling of Hg in the environment can lead to increased levels in the food chain, where it can be passed on to humans. The methylated forms of Hg are especially mobile in humans due to complexation reactions with cysteine, which increases the transport of Hg throughout the body. Mercury exposure affects the human central nervous system and can lead to symptoms such as personality changes, tremors, motor control loss, and possibly death (Clarkson and Magos, 2006). Mercury also affects reproduction and survival rates in both birds and fish (Scheuhammer et al., 2007). Tracking the transport and cycling of Hg in the environment is needed to minimize potential human and ecosystem health effects.

When Hg is present in lake sediment, it can undergo different cycling pathways. Sulfate reducing bacteria (SRB), commonly found in anoxic sediments, have been implicated as a principal methylator of Hg in freshwater, estuarine, and marine sediments (Compeau and Bartha, 1985; Gilmour et al., 1992; King et al., 2000, King et al., 2001), though additional studies in molybdate-inhibited sediments have shown that iron reducing bacteria (IRB) may also play an important role in methylation (Kerin et al. 2006; Fleming et al., 2006). Sulfate reducing bacteria also can be involved with oxidative demethylation reactions, competing with methanogenic bacteria in anoxic freshwater sediment (Oremland et al., 1991, Oremland et al., 1995, Pak and Bartha, 1998, Marvin-DiPasquale and Oremland, 1998; Marvin-DiPasquale et al., 2000). Gilmour and Henry (1991) observed a relationship exists between aqueous sulfate concentrations and methylation rates in freshwater, estuarine, and marine sediments. Methylation is reduced in both sulfide-inhibited and sulfate-limited conditions, thus showing the importance of sulfur as a control on Hg cycling and transport. Mercury may cycle from the

aqueous phase to the atmosphere due to volatilization of dissolved gaseous Hg (DGM) produced by photoreduction reactions (Amyot et al., 1994). Dissolved gaseous Hg production is enhanced in the presence of photochemically reactive Fe(III) (Zhang and Lindberg, 2001).

A number of techniques are available to mitigate and remediate contaminated lake sediment, depending on the type and the extent of contamination. General mitigation strategies include monitored natural attenuation, in situ capping, and sediment removal by dredging operations (Herbich, 1995; Wang et al., 2004). Natural attenuation may be effective in cases where the contaminant either degrades quickly or is otherwise buried by natural deposition, though cycling of the contaminant may still occur until it is fully isolated from the food chain. Although volatilization of DGM may be an important natural attenuation mechanism in aqueous systems, it is not feasible for heavily contaminated sites. In situ capping involves the placement of a confining layer above the sediment, typically composed of sand or sand mixed with various sorptive or reactive materials, to prevent contaminant migration into the overlying water column. Several factors can affect the efficiency of sediment caps, including tidal flow and bioturbation effects, hyporheic and groundwater flow conditions, consolidation-induced convective flow, and scour due to propeller wash, ice dams, and surface water flows (Liu et al., 2001; Moo-Young et al., 2001; Simpson et al., 2002; Alshawabkeh et al., 2005). Sediment dredging involves the physical removal of the contaminated sediment to minimize future releases into the overlying water. Dredging operations generally fall into two categories: mechanical dredging, which involves a physical excavation of the sediment with minimal entrained water removal, and hydraulic dredging, where large amounts of water are mixed with the sediment to form a slurry for subsequent removal. In either case the dredged sediment is typically disposed of, and treated off site by ex situ capping/treatment technologies. The main

disadvantages of dredging operations are the potential release of contaminants from resuspended or residual sediments. The resuspension of anoxic sediment can result in the release of heavy metals due to oxidative dissolution processes (Caetano et al., 2003), thus a comprehensive site characterization first should be completed to assess the potential for contaminant release during dredging operations.

The focus of this study is on a freshwater lake reservoir (Figure 3.1) with additional ungauged flow from a small brook to the northwest. Releases from a former manufacturing plant adjacent to the point of discharge to the lake (not shown) resulted in elevated concentrations of Hg, Pb, and Se in the lake sediment. The first part of this study involved whole sediment analysis from several different areas of the lake, labeled A through J (Fig. 3.1). Sediment digestion, grain-size analysis, and semi-quantitative mineral identification by X-ray diffraction (XRD) were employed to characterize the initial physical and chemical properties of the sediment and to determine the relative concentrations and distribution of Hg and other toxic constituents. Speciation analyses, including sequential extraction methods and synchrotron-based X-ray fluorescence (XRF) and X-ray absorption near edge spectroscopy (XANES), were employed to determine the chemical form and association of Hg and other constituents in the sediment. Finally, sediment leaching procedures, including the synthetic precipitation leaching procedure (SPLP) and sediment resuspension tests were employed to evaluate the leaching potential under variable geochemical conditions. Combined, these methods were used to gain an improved understanding of binding mechanisms controlling Hg distribution and potential release under a range of physical and geochemical conditions.

3.3 Materials and Methods

3.3.1 Initial Chemical Conditions

Ten sediment cores collected from a Hg contaminated site (Figure 3.1) were shipped in individual 4 L containers containing water-saturated sediment and approximately 2-3 cm of standing water. The containers were maintained at 4 ^{o}C after collection and upon arrival at the University of Waterloo. Prior to homogenization of the sediments, portions of the standing water were collected from each container and analyzed for total Hg by cold-vapour atomic absorption spectrometry (CV-AAS) by SGS Lakefield Laboratories (Lakefield, ON, Canada) to determine if Hg leaching had occurred during transport. The detection limit by this technique was reported as 100 ng L^{-1}. The core samples (sediment plus pore water) were homogenized by manual mixing in an anoxic glovebox (COY Laboratory Products, Ann Arbor, MI) with a 3 % H_2: 97 % N_2 gas atmosphere to minimize oxidation of the sediment prior to subsampling for the various experiments and analyses. After homogenization of the sediment and porewater, portions of the sediment were collected and analyzed for total Hg, major, minor, and trace elements by ICP-AES and ICP-MS at SGS Lakefield Laboratories. An aqua-regia digestion step was used to prepare the sediment for elemental analysis. Total carbon (inorganic and organic) and sulfur concentrations were measured following combustion with a carbon sulfur determinator (Eltra Inc. CS-2000) at the University of Waterloo.

3.3.2 Mineral Identification by X-ray Diffraction

Sediment samples were dried at 110 ºC and analysed for mineral identification by X-ray diffraction (XRD) by Activation Laboratories (Ancaster, ON, Canada). The X'Pert High Score software was used for "semi-quantitative" analysis through the reference intensity ratio (RIR) method, where the RIR values were based on the ratio of the relative peak height of the phase to the strongest line of corundum and matched to the Powder Diffraction File (PDF) database. The detection limits ranged from 0.5 to 5 weight % based on phase crystallinity. The procedure provides an indication of the bulk mineralogy, and qualitative analysis of the clay components.

3.3.3 Particle Size Distribution

Sediment samples were dried at 110 ºC and analysed for particle size distribution by a particle size analyzer (SGS Lakefield Laboratories, Lakefield Ontario). The external laboratory reported that the presence of organic matter in the sediment interfered with the analysis of particles smaller than 1 μm.

3.3.4 Mercury Speciation by X-ray Absorption Spectroscopy

Four of the sediment samples (A, D, I, and J) were dried at room temperature in a vacuum desiccator placed in an anoxic glovebox. Polished thin sections (24 x 46 mm) were prepared without the use of water by Vancouver Petrographics Ltd. (Langley, BC, Canada). Thin sections allow analyses to be performed through mineral and other sediment particles, providing information on the grain interior and surface distribution of target elements. The thin sections were analyzed by synchrotron radiation on Beamline 13-BM-D-GSECARS at the Advanced Photon Source (APS) at the Argonne National Laboratory (ANL) in Argonne, IL. A

focused X-ray beam of ~10 μm diameter was used to analyze the thin sections by X-ray absorption near-edge spectroscopy (XANES) and X-ray fluorescence (XRF) spectroscopy. These techniques provide information on the distribution and binding of the elements of interest. XANES data were processed using the program ATHENA (Ravel and Newville, 2005).

3.3.5 Mercury Speciation by Sequential Extraction Analysis

Sequential extraction analyses were conducted on 100 g samples following the protocol developed by Bloom et al. (2003) at Battelle Laboratories – Pacific Northwest Laboratories Division (Sequim, WA). This protocol was developed to assess the bioavailability of Hg in sediments through a five-step extraction process: deionized water (targets $HgCl_2$, $HgSO_4$), F2 - 0.01M HCl (targets $HgSO_4$, HgO, adsorbed Hg), F3 - 1M KOH (targets organo-chelated Hg, Hg_2Cl_2), F4 - 12M HNO_3 (targets Hg^0, thiol-bound Hg), and F5 - aqua regia (targets HgS, HgSe, HgAu). A Tekran Model 2500 Cold Vapor Atomic Fluorescence Spectrophotometer (CV-AFS) was used for total Hg determinations in each extract following EPA Method 1631 (U.S. EPA, 2002).

3.3.6 Synthetic Precipitation Leaching Procedure (SPLP)

The synthetic precipitation leaching procedure (SPLP) is designed to evaluate the potential for groundwater contamination from land deposited solid wastes. This is accomplished through the application of slightly acidic water to a sample of the waste to simulate leaching caused by acidic precipitation. This procedure is similar to the toxic characterization leaching procedure (TCLP) used to evaluate contaminant release due to landfill leachate. The main difference

between the tests is that the SPLP uses a mixture of strong acids (HNO_3 and H_2SO_4) at pH 5.0 or 4.2, whereas the TCLP uses weak acid (CH_3COOH) extraction at pH 4.9 or 2.9. Approximately 250 mL of each sediment sample was analysed for leaching potential of Hg by Brooks Rand Laboratories (Seattle, WA) following the synthetic precipitation leaching procedure (SPLP) outlined in EPA Method 1312 (U.S. EPA, 1996a). The procedure was modified slightly to reduce the volume of sediment from 1 L required in the EPA method. Sediment leachates were analyzed for total Hg by EPA Method 1631 (U.S. EPA, 2002), major/minor/trace elements by EPA Method 1638 (U.S. EPA, 1996b), and % total solids by EPA Method 160.3 (U.S. EPA, 1983).

3.3.7 Resuspension Tests

A series of resuspension tests were conducted to evaluate the potential release of Hg and changes in geochemical parameters during mixing of the sediment and water. The procedure used was a modified version of the elutriate test; a standard testing protocol developed by the EPA to simulate the impact of dredging contaminated sediments (U.S. EPA, 1996c). The EPA method requires vigorous mixing of 1 L of sediment and 4 L of site water for 30 min, and then sampling after a 1 h settling time. For this study, modifications to the EPA method were made to reduce the volume of sediment and to use a local source of water due to limitations on the available volumes of lake sediment and site water. The amounts of sediment and water used were reduced while maintaining the 1:4 ratio described in the EPA method. Local water, obtained from the Laurel Creek headwaters located ~8 km west of the University of Waterloo, was used as a surrogate for the site water requirement. This local water is similar in chemical composition to the site water, however, differences in pH, temperature, and bacterial content

are likely present. Two additional modifications were made to the method to gain information about the fate of Hg in response to changing geochemical conditions. Additional mixing times at 6 h and 24 h were added to the initial 30 min mixing time to evaluate the temporal effects of mixing on the leaching of Hg and other contaminants in the water. The tests were conducted under both well-oxygenated (oxic) and oxygen-limited (anoxic) conditions to assess the effects of mineral dissolution and desorption reactions in the presence or absence of oxygen.

For each sediment core sample, a 40 g portion of homogenized sediment and 160 g of surrogate site water were added to three separate pre-cleaned 250 mL amber glass bottles (VWR® TraceClean™ with PTFE-lined caps). For the anoxic tests, the surrogate water was first purged with Ar_2 for ~1 h to remove dissolved oxygen and the tests were performed in an anoxic glovebox. For the oxic tests, the samples were mixed in a fume hood to enhance contact with atmospheric oxygen. For both tests, the bottles were loosely covered, placed on a magnetic stirrer, and mixed vigorously for 30 min, 6 h or 24 h.

At each sampling interval, one of the 250 mL sample bottles was randomly chosen and removed from the magnetic stirrer for measurements of pH and Eh on unfiltered samples and alkalinity and cation/anions on filtered samples. For the filtered samples, it was necessary to add a centrifugation step prior to filtering to enhance settling of the sediment. The sediment slurry was transferred into Oak Ridge polypropylene copolymer centrifuge tubes and centrifuged at 6000 rpm (~3900 g at 9.75 cm rotor length) for 15 min. A centrifugation step was necessary because the sediment stayed in suspension after an extended settling time (e.g., 2-3 hours). The resulting supernatant was transferred into a NORM-JECT® latex-free 24 mL single-use syringe and filtered using Acrodisc® 32 mm single-use syringe filters with 0.45 μm Supor® membranes. The pH was measured using an Orion Ross combination electrode (model

815600) calibrated using standard buffer solutions at pH 4, 7, and 10, and Eh was measured using an Orion platinum redox electrode (model 96-78BN) checked against ZoBell's solution following the procedure of Nordstrom (1977). Alkalinity measurements were made on filtered samples using a Hach digital titrator with bromocresol green/methyl red indicator and 0.16 N H_2SO_4. Samples for Hg analysis were placed in Supelco pre-cleaned 15mL amber screw cap vials and preserved with a mixture of $K_2Cr_2O_7$ and HNO_3. Total cation samples were acidified to a pH of <2 with 16 N trace-metal grade HNO_3 while anion samples were left unacidified. All samples were immediately refrigerated until analysis. Two method blank samples were included to track potential Hg contamination. Surrogate site water alone was added to the bottles and mixed, centrifuged, and sampled following the procedure described above.

3.3.8 Oxidation Tests

An additional test was designed to simulate geochemical conditions that might occur when dredged sediments are placed on land for dewatering purposes, disposal in a landfill, or re-used as fill. These conditions (moderate moisture contents combined with unlimited oxygen) could potentially lead to increased Hg oxidation within the sample, thereby promoting Hg release. A portion of the sediment (~150 g) was dried in contact with atmospheric oxygen under a fume hood. After 2 h of drying, the sediment was homogenized and sampled for the 30 min oxic resuspension protocol described above. The drying, homogenization, and sampling procedures were repeated at 6 h and 24 h total drying time, followed by the 30 min resuspension protocol at these additional times.

3.3.9 Analysis of Water Samples

Water samples were analysed to determine concentrations of anions (Cl, NO_3, and SO_4) using ion chromatography (Dionex Ion Chromatograph) and trace cations using quadrupole ICP-MS (Thermo Scientific X-Series 2). Concentrations of total Hg were determined using high-resolution ICP-MS (Thermo Scientific Element 2). Methanol (4 %) was added to each Hg sample following the procedure of Paul et al. (2003) to minimize sample carryover while maximizing sensitivity. The lower limit of quantitation for the Hg analyses following this procedure was typically at 10 ng L^{-1}, although background contamination in the analyses for the anoxic samples increased this limit to 50 ng L^{-1}. For all ICP-MS analyses, new blanks were analyzed every 5 samples and new calibration standards were analyzed every 15 samples to track potential carryover and instrument drift effects. Additional total Hg samples were sent to Battelle Laboratories (Sequim, WA) for quality control purposes. These samples were analyzed following EPA Method 1631, and the reported method detection limit was 0.121 ng L^{-1}. The statistical package in Sigmaplot Version 11.0 (Systat Software, Inc.) was used for Spearman correlation analysis.

3.4 Results and Discussion

3.4.1 Initial Chemical Conditions

Samples of the standing water in each sediment core container were below the detection limit of 100 ng L^{-1} as reported by the external laboratory. Results from the sediment digestion and total carbon and sulfur analysis indicate that the highest Hg concentrations were found in samples A, B, C, D, E, and G. Samples A, D, and E also were relatively high in other toxic elements, such as As, Cd, Pb, and Se. Samples A, C, and J were relatively high in total carbon,

and samples A and J also were relatively high in total sulfur. The total carbon measurements include both organic and inorganic carbon, thus it is possible that there is some amount of organic matter in the sediment though this test does not give a quantitative measurement of organic carbon. Mercury concentrations for the 10 sediment samples exhibited a positive correlation ($p < 0.05$) with Cu ($r = 0.77$), Pb ($r = 0.93$), and Se ($r = 0.79$). No statistical correlation existed between Hg and S or C.

The reported range of Hg concentrations (22 to 335 $\mu g\ g^{-1}$, dry weight) is comparable to those observed at other contaminated sites. Clear Lake, in Clearlake Oaks, CA, is an EPA Superfund site with contamination from a nearby sulfur and Hg mine. Recent studies by Suchanek et al. (2009) reported Hg concentrations up to 438 $\mu g\ g^{-1}$. The East Fork Poplar Creek (EFPC) floodplain in Oak Ridge, TN, was contaminated with elemental Hg during the 1950s due to releases from a nearby DOE facility. Barnett et al. (1995) report concentrations in the floodplain soils ranging from 42 to 2400 $\mu g\ g^{-1}$. Campbell et al. (1998) measured concentrations ranging from 0.63 to 140 $\mu g\ g^{-1}$ downstream from the EFPC headwaters. Earlier studies by Elwood (1984) found concentrations ranging from < 0.1 to 300 $\mu g\ g^{-1}$.

3.4.2 Semi-quantitative Mineral Identification by XRD

The sediment consists mainly of quartz, albite, microcline, and clay species that were qualitatively identified as muscovite and chlorite (Table 3.2). The total clay composition ranged from 22 % (sample G) to 54 % in samples H and J. There was also a varying amount of amorphous material, which could include materials such as organic matter or amorphous iron oxides. The presence of clay minerals, organic matter, or metal (hydr)oxides can affect the bioavailability of aqueous Hg through adsorption processes (Bonnissel-Gissinger et al., 1999;

Dmytriw et al., 1995; Tiffreau et al., 1995; Schuster, 1991), or through methylation/demethylation reactions (Jackson, 1989; Oremland et al., 1991; Ullrich et al., 2001).

3.4.3 Particle Size Distribution

A sediment texture triangle based on a revised classification developed by Flemming (2000) was prepared from the particle size distribution curves (Figure 3.2). This classification is valid for gravel-free muddy sediment, with a silt/clay boundary of 2 μm and a sand/silt boundary of 62.5 μm. The samples can be classified as extremely silty slightly sandy mud (G, H, I), extremely silty sandy mud (A, C, D, E, F), and very silty sand (B, J). Higher concentrations of Hg tended to be found in sediment classified as extremely silty sandy mud. As noted in the methods section, the particle size analysis was limited to 1 μm due to interferences with organic matter in the sediment. The observations from both the total sediment digestion (Table 3.1) and XRD analysis (Table 3.2) were consistent with the presence of a variable amount of organic carbon.

Boszke et al. (2004) investigated the distribution of Hg in different grain size fractions of river bed and bank sediment. They reported a general decrease in Hg concentrations with increasing grain size for the bed sediment, and generally higher concentrations in finer sediments (200 μm) from the river banks. A similar relationship was found by Loring (1975) in sediment in the Gulf of St. Lawrence, who also report that organic matter increased with decreasing grain size. Suchanek et al. (1998) reported that low ratios of methyl:total Hg in a lake sediment adjacent to an abandoned Hg mine are possibly related to a coarser sediment fraction that had a lower potential to support methylation. Mercury concentrations were also

found to be approximately 30 times higher in silt and clay (< 0.063 mm particle size) compared to larger particles in areas impacted by historical gold mining (Hunerlach et al., 2004; Alpers et al., 2006). The reports from the literature thus suggest that grain size may be an important indicator for determining the distribution of Hg in sediment, though no statistical correlation was found between sediment Hg concentrations and % silt or % clay in the current work.

3.4.4 Mercury Speciation by X-ray Absorption Spectroscopy

With the micro-X-ray beam analyses, Hg was easily detected on sample D but difficult to locate on the other three thin sections, likely due to the relatively low Hg concentrations in these samples. The micro-X-ray fluorescence maps of Hg, Fe, Se, and Cu on one area of the sample D thin section indicate that Hg is mainly concentrated in two areas (Figure 3.3). The smaller, more concentrated area (circled in white) also had strong fluorescence responses for both Se and Cu. Correlation plots of the μ-XRF data in this spot (Figure 3.3) show that Hg was positively correlated ($\rho < 0.05$) with Se ($r = 0.93$) and Cu ($r = 0.73$), while Se and Cu also had a positive correlation ($r = 0.77$). Because Hg, Se, and Cu are all chalcophilic elements, the correlation results support the possible presence of a sulfide phase at this location. X-ray absorption near edge spectroscopy (XANES) analyses for the Hg L_{III} and the Se K_{α} edges were performed on this spot and compared to a signal obtained from a tiemannite (HgSe) mineral specimen (obtained from Excalibur Mineral Corp., Peekskill, NY). The XANES results suggest that Hg is present in a reduced form, potentially as HgSe (Figure 3.4). Although no other statistically significant correlations were observed among the whole elemental datasets, linear relationships were observed between Hg and Fe at high Hg counts, and Fe and Se at high Se counts. These correlations could be due to Hg sorption onto Fe-oxides and Se incorporation

into pyrite (FeS_2) grains, respectively, although no other data were available to corroborate the observations.

A second XRF map was collected at a different position on the sample D thin section (Figure 3.5). Again, correlation plots showed a strong correlation between Hg and Cu ($r = 0.84$) and Se and Cu ($r = 0.89$). XANES analyses were obtained for Cu in the area circled on Figure 3.5 and compared to a CuS mineral standard (Figure 3.6). The results suggest that Cu is likely present as CuS in this area. Although beamline focusing problems prevented the acquisition of Hg XANES data in this location, the presence of Hg and CuS in the same location suggests that Hg is likely present as HgS.

Synchrotron-based X-ray techniques were applied by Xia et al. (1999) and Skyllberg et al. (2006) to investigate the complexation of Hg(II) in soil organic matter. They reported that Hg(II) was preferentially complexed to soil humic acid containing reduced organic sulfur groups, with some complexation to oxygen/nitrogen groups after the high affinity sulfur sites had been saturated. Bernhaus et al. (2006) utilized XANES and μ-XRF techniques to characterize Hg and other heavy metals in a soil near a chlor-alkali plant. Principal component analysis of the XANES data showed that a majority of the samples consisted mainly of cinnabar [HgS] and corderoite [$Hg_3S_2Cl_2$], with lesser amounts of HgO and $HgSO_4$. The dominant mineral phases were attributed to elevated levels of S (0.051 %) and Cl (5 mg kg^{-1}) in the soil. A μ-XRF map of a 100 μm^2 section showed linear correlations between Hg and Ni ($r^2 = 0.99$) and Hg and Cu ($r^2 = 0.90$) though no correlations were found with S, indicating that associations with sulfide were not likely present in this particular sample. Bernhaus et al. (2006) proposed that a solid solution of Hg, Ni, and Cu within the same crystal structure could explain the correlations, although no other data were available to support this hypothesis. The

reported sulfur concentration in the soil (0.05 %) is lower than the concentrations reported in the current study (Table 3.1). Thus, it is expected that interactions between Hg and S would be important in the lake sediment studied here. Although the beamline energy used in this study was too high to detect the presence of sulfur-bearing compounds, the possible existence of HgSe and the strong correlation between Hg, Cu, and Se in the same location suggest that sulfide minerals also were present.

3.4.5 Mercury Speciation by Sequential Extraction Analysis

The results of the sequential extraction procedure (Table 3.3) are compared to the total bulk concentrations listed in Table 3.1. For all but one of the samples (J), the largest percentage of Hg was observed in either the F4 or F5 extractions, with the F4 (Hg^0 and thiol-bound Hg) fraction being the dominant source of Hg in samples A, C, F, G, H and I. Similar extraction profiles were observed for samples A and C, although sample A had a higher total solid phase concentration. Samples B, D, and E were dominated by HgS and/or related forms of Hg. This supports the previous XAS findings for sample D, which implied the formation of Hg sulfide/selenide. For sample J, the largest percentage (68 %) of Hg was observed in the F3 extraction, which targets organo-chelated Hg and Hg_2Cl_2. This fraction ranged from 12 to 20 % in the other sample locations. Mercury methylation potential has been shown to be strongly correlated with this fraction (Bloom et al., 2003). Devices such as benthic flux chambers may be used to monitor groundwater and surface water interactions at the sediment interface (Menheer, 2004), and previous flux chamber data obtained at this site indicated positive methylmercury fluxes at sample location J ranging from 22.1 to 24.8 ng m^{-2} day^{-1}. Concentrations of water-soluble Hg were low in all samples, ranging from 0.03 to 0.15 %.

Concentrations of acid-soluble Hg ranged from 10^{-3} to 10^{-5} %, indicating that there was very little HgO or adsorbed Hg species present in any of the samples.

The sequential extraction results are comparable to other reports using the same or similar extraction procedures. Boszke et al. (2006) applied a procedure using chloroform, deionized water, 0.5 M HCl, 0.2 M NaOH, and aqua regia to a tsunami-deposited sediment in Thailand. Mercury was mainly bound to sulfides (~75 %), organomercury compounds (~14 %) and humic matter (~9 %), with low contributions (<1 %) from water- and acid-soluble Hg. The concentration range of Hg was 66 to 230 ng g^{-1}. Boszke et al. (2008) applied the same procedure to soil near an industrial plant that used elemental Hg in the manufacturing of thermometers and areometers. Mercury was bound to sulfides (~56 %), humic matter (~22 %) and present as elemental Hg (~17 %). Lesser amounts were found as organomercury (~2.3 %), acid soluble (~1.5 %) and water-soluble Hg (~1.0 %). The concentration range was 62 to 393 μg g^{-1}. Liu et al. (2006) applied the extraction method of Bloom et al. (2003) to soil surrounding the Y-12 National Security Complex in Oak Ridge, TN. More than 50 % of the total Hg was extracted in the F3 fraction, representing organo Hg. The next highest fraction (20-30 % of the total) was removed in the F4 fraction, which targets Hg^0, Hg amalgams, and Hg associated with Fe/Mn oxides. A lesser portion of Hg (10 %) was extracted in the F5 fraction with minor amounts extracted in the F1 and F2 fractions. Kocman et al. (2004) also applied the extraction method by Bloom et al. (2003) to soils in an Hg mine area. They observed lower percentages of organic matter in samples with higher amounts of Hg removed by the F3 fraction. Although this fraction is commonly linked to Hg bound to humic matter, their results suggested that other forms of Hg may have been extracted instead.

3.4.6 Synthetic Precipitation Leaching Procedure (SPLP)

The highest potential for Hg release by the SPLP analysis was observed for samples A, B, D, and E (0.69 to 1.46 μg L^{-1}), whereas lower concentrations were observed for samples C, G and J (0.21 to 0.35 μg L^{-1}) (Table 3.4). The leaching procedure also resulted in release of several chalcophilic elements, with elevated concentrations of Cu, Pb, and Se in sample A and Cd, Cu, and Pb in sample D. In contrast, relatively low concentrations of metals were released from sample C, with the exception of Se. Spearman correlation analysis across all samples shows no statistical correlation ($p > 0.05$) between extractable Hg and Cu ($r = 0.52$), Pb ($r = 0.27$), or Se ($r = 0.52$), though positive correlations were found between Hg concentrations in the sediment (as listed in Table 3.1) and extractable Hg ($r = 0.88$), Cu ($r = 0.67$), and Se ($r = 0.70$).

The SPLP method is a useful indicator for leaching potential under acidic precipitation conditions, though Hg release is dependent on the chemical form in the sediment. Mercury sorption in the absence of complexation reactions with Cl^-, DOC, or sulfide tends to reach maximum values at pH < 7 because $HgOH^+$ is predicted to be the dominant aqueous species (Schuster, 1991). The addition of Cl^- shifts the pH of maximum sorption to higher values due to the formation of Hg-Cl complexes. Mercury-DOC and Hg-DOC-sulfide complexes will likely be dominant when high concentrations of DOC are present, or when the system is under sulfidic conditions (Ravichandran et al., 1999; Reddy et al., 2000; Ravichandran, 2004), Other literature reports present evidence of decreasing sorption of Hg with increasing pH on different materials, including waste rubber (Knocke and Hemphill, 1981), clay minerals (Farrah and Pickering, 1978), goethite (Barrow and Cox, 1992a), and a soil (Barrow and Cox, 1992b).

Based on this information, the addition of acidic water in the SPLP may have little effect on the release of Hg from the sediment if sorption effects are a dominant attenuation

mechanism. The sequential extraction analysis also predicted that the amount of adsorbed Hg in each sediment sample is insignificant compared to other forms of Hg (Table 3.3). The observation of acid leachable Hg in the current study may mean that Hg release in the sediment is dependent on the forms of Hg that are susceptible to strong acid effects. MacLeod et al. (1996) performed column experiments to evaluate the mobilization of Hg under simulated acid rain conditions. An aquifer sediment was artificially contaminated with a 1000 $\mu g\ L^{-1}$ Hg solution at a pH of 5 and was packed into a column with an underlying sand layer. A solution of 0.1 mM HNO_3 was passed through the column to assess the leaching potential. Although the acid displaced 22 % of the Hg from the sediment compared to <0.5 % for a 14 mM solution of $NaNO_3$, the difference in leaching potential was attributed to acid effects on mineral surfaces rather than displacement of Hg by H^+. Mikac et al. (2003) investigated the dissolution of cinnabar and metacinnabar by HNO_3 and observed that both minerals were insoluble in pure acid. The addition of Cl from $FeCl_3$ or from naturally saline sediments enhanced the solubility of HgS in HNO_3. The small amount of Cl present in typical freshwater sediment (10^{-5} M) was sufficient to enhance Hg extracted from soil and increase the solubility of metacinnabar. The addition of Cl to HNO_3 was thought to produce Cl_2, which induces HgS oxidation. One of the assumptions made in the sequential extraction analysis performed in this study is that HgS is insoluble in HNO_3, and thus Hg sulfides would not normally be removed in the F4 fraction. However, the observations by Mikac et al. (2003) may imply that a minor amount of HgS dissolution occurred during the F4 fraction, and thus the results in Table 3.3 may have overestimated the relative amounts of Hg species normally extracted by HNO_3.

3.4.7 Sediment Characterization - Resuspension and Oxidation Tests

Geochemical conditions varied between the oxic and anoxic resuspension tests (Figure 3.7). The pH was similar between the oxic and anoxic experiments with the exception of slightly lower pH values observed for sample C during the anoxic experiments. The pH values were observed to increase slightly in samples A and C relative to the surrogate site water (~7.5), whereas the values for the other samples decreased by up to a full pH unit over time. The difference between sediment samples suggests that there is a large site-to-site variability in sediment composition, which could affect the buffering capacity over the course of the experiments. The results of the oxic experiments showed nearly constant to slightly declining Eh values, whereas the anoxic experiments showed much lower initial Eh values that declined over time. These lower values are consistent with the expected values for anoxic systems. Values of alkalinity varied for the different sediment samples and were typical of hard water areas or groundwater-fed surface water bodies.

Changes in pH and Eh can affect Hg speciation and cycling. Compeau and Bartha (1984) determined Hg methylation and demethylation potentials in an estuarine sediment. Experimental results showed that under low redox potential (-220 mV) and low salinity (0.4 %), methylation was favoured and demethylation processes were inhibited. Higher salinity inhibited methylation whereas high redox potential promoted demethylation. Given the lower redox potentials in the anoxic resuspension tests, there could be an increased potential for methylation compared to the oxic tests. Lower pH values may also result in the increased uptake of Hg by H_2-utilizing bacteria (Kelly et al., 2003) and the increased bioavailability of Hg by decreasing the amount of complexation by DOC (Barkay et al., 1997). Cinnabar solubility also exhibits a dependence on both pH and the presence of sulfide/polysulfide

species, with increasing formation of aqueous Hg polysulfide complexes at increasing pH (Paquette and Helz, 1995; Jay et al., 2000). Given the slightly-acidic to neutral pH values measured in the current experiments, these processes are not expected to be important.

Large differences in Hg release between the oxic and anoxic tests were observed (Figure 3.8). For samples A, B, D, and E, Hg concentrations generally increased with increased mixing time, with maximum concentrations of several hundred μg L^{-1} per kg of dry sediment observed after either 8 or 24 hours of oxic mixing. The highest concentrations observed in these samples corresponded to aqueous phase concentrations of 2.8 to 7.1 μg L^{-1}, which exceed the Environmental Protection Agency (EPA) regulated Maximum Contaminant Level (MCL) of 2 μg L^{-1} for inorganic Hg (U.S. EPA, 2009). For the remaining samples, Hg concentrations were less than 200 μg L^{-1} per kg dry sediment. Samples with relatively high solid phase Hg concentrations (e.g., A, B, D, E, G) showed a relatively higher release of Hg during both oxic and anoxic resuspension experiments. An exception was sample C, which had approximately the same solid phase concentration as sample B (81 μg g^{-1} vs. 79 μg g^{-1}) yet did not release a significant amount of Hg. These results compare well with the SPLP results (Table 3.4), which showed that samples A, B, D, E, and G had a higher potential for Hg release under simulated precipitation conditions, with sample C having a relatively low potential for release. Mercury speciation results from the sequential extraction analysis (Table 3.3) indicate that sample C contained a large percentage of the F4 fraction (> 60 %) and a relatively low percentage of the F5 fraction (< 20 %) compared to samples B, D, E, and G, which could explain the differences in leaching potential. Filter size may also have had an effect on the observed variability in concentrations. A standard 0.45 μm filter was used to filter the aqueous samples for total "dissolved" Hg. However, if colloidal forms of Hg (e.g., < 0.45 μm) also passed through the

filter, then the total Hg concentrations obtained during analysis would include both dissolved and colloidal Hg and thus the Hg concentrations may be overestimating the actual dissolved Hg concentration. The importance of the colloidal forms of Hg was investigated by Stordal et al. (1996), who observed variable colloidal Hg fractions in various surface water samples ranging from 12 to 93 % of the total "dissolved" Hg. The resuspension experiments performed in this work may have induced the release of both dissolved and colloidal forms of Hg, though the measurement of Hg colloids were not evaluated in the current work.

Mercury concentrations were substantially lower in the anoxic resuspension tests, ranging from ~5 to 160 μg L^{-1} per kg dry sediment (Fig. 3.8). The lowest concentrations were observed for samples C, F, H and I, with samples F, H, and I having relatively low solid phase concentrations (~22 to 51 μg g^{-1}). These results suggest that oxidation reactions are enhancing Hg release. This is consistent with the results from the sediment oxidation experiments (Figure 3.9) which resulted in a general increase in Hg release vs. drying time. The release of Hg could be due to oxidative degradation of organic carbon present in the sediment as evidenced by the total sediment analysis (Table 3.1), XRD analysis (Table 3.2), and grain size analysis (Fig. 3.2), or by oxidative dissolution of Hg sulfide/selenide phases likely present in the sediment, as observed by the XRF/XANES analysis (Fig. 3.3-3.6) and sequential extraction procedure (Table 3.3). Hopkinson (1985) observed that sediment resuspension increased the transport of organic matter to the water column, and Wainright (1987) observed that bacterial growth increased during resuspension events, which contributed to mineralization of organic matter. Holley et al. (2007) reported environmentally significant Hg mobilization during oxidative dissolution of cinnabar and metacinnabar. Sulfate concentrations increased with increasing mixing time and the rate of Hg mobilization was two orders of magnitude lower than the rate

of sulfate production. This decrease in mobilization was partially attributed to re-adsorption of Hg(II) to Hg sulfide surfaces. The presence of dissolved organic matter (DOM) can increase the solubility of cinnabar independent of oxygen concentrations (Ravichandran et al., 1998; Waples et al., 2005). Components of DOM can both enhance and inhibit cinnabar dissolution, and the dissolution rates are thought to be due to competitive sorption of these components onto the cinnabar mineral surface. The presence of sulfide also can cause the reductive dissolution of iron oxyhydroxides, such as goethite. Studies have shown that the elemental sulfur and polysulfide species produced by this process can facilitate the dissolution of mercuric sulfides (Slowey and Brown, 2007).

Mucci et al. (1995) performed a field-scale resuspension test in a hydroelectric reservoir near James Bay. After 3 days of resuspension, mass transfers of ~57 % organic carbon, 4 % inorganic Hg, and 71 % methyl Hg from the soil to the water column were observed. A decrease in total dissolved Hg concentrations after 3 days also were observed, which was attributed to mass transfer of dissolved Hg to suspended particle matter. Caron and Lucotte (2008) investigated Hg inputs into Lake St. Pierre, Quebec. Total dissolved Hg concentrations averaged 1.14 ng L^{-1} with no concentration exceeding 2.78 ng L^{-1}, and suspended particulate matter (SPM)-bound total Hg ranged from 0.03 to 14.55 ng L^{-1} with an average of 1.16 ng L^{-1}. There was no strong correlation between dissolved Hg and SPM-bound Hg. However, there was a correlation between dissolved Hg and the fraction of terrestrial organic matter (TOM) in the SPM, suggesting that organic matter is an important scavenger of aqueous Hg during resuspension events. Hydrologic cycling can also induce resuspension events that mobilize Hg. Domagalski et al. (2004) measured Hg concentrations in the Cache

Creek watershed in California, and observed increased loading of both aqueous Hg and CH_3Hg during rainfall events.

The release of two other potentially toxic constituents, Se and Pb, were also monitored (Figure 3.10). Selenium concentrations generally were observed to increase over time in samples A and J, with sample J having higher Se concentrations in the oxic experiments. For sample A, the releases were similar during both the oxic and anoxic experiments, indicating that release was likely not controlled by oxidative dissolution in this location. Higher releases of Se were observed in the anoxic tests for samples B, F, and H, compared to the oxic tests. Concentrations of Pb increased significantly in sample A for the oxic conditions, compared to only a slight increase in the anoxic conditions. Changes in Pb concentrations were variable for the remaining samples, with no clear positive or negative trend versus mixing time or with redox environment. The results for sample A were similar to the SPLP results, which also showed an increased potential for the release of Se and Pb. Lead concentrations normalized to sediment mass for samples A, D, and E corresponded to aqueous concentrations ranging from 20 to 55 $\mu g\ L^{-1}$. Although the EPA has not set an MCL for lead in drinking water, a Treatment Technique (TT) action level of 15 $\mu g\ L^{-1}$ has been established, which these samples exceed. The increase in Pb concentrations could be due to the oxidative dissolution of PbS, which was implied to be present in samples A and D based on the SPLP extraction and XRF/XANES analysis.

The release of anions also varied with sediment location and between the oxic and anoxic tests. Nitrate concentrations were consistently low in all samples ($< 5\ mg\ L^{-1}$) and Cl^- concentrations were fairly consistent between locations, ranging from ~30 to 45 $mg\ L^{-1}$ with no change in concentration with mixing time. Concentrations of sulfate generally increased during

increased mixing time for samples A and J under oxic conditions, with higher release observed under anoxic conditions for sample J (Figure 3.11). Although sulfate concentrations are expected to increase during HgS dissolution (Holley et al., 2007), the concentrations observed in the current study during oxic and anoxic resuspension are much greater than the observed difference in Hg concentrations, and thus a change in sulfate due to oxidative dissolution of HgS or other sulfides such as FeS may not be noticeable.

3.5 Conclusions

Mercury contamination in the lake tends to be concentrated in areas adjacent to the point of discharge. Mercury releases during the synthetic precipitation and resuspension testing were generally correlated to sediment locations containing higher concentrations of Hg. During the oxic resuspension experiments, four of the sediment locations resulted in aqueous Hg concentrations that exceeded the EPA drinking water regulations and three locations resulted in elevated Pb concentrations. However, concentrations measured during the anoxic resuspension tests were much lower. The large differences between the two resuspension tests imply that there is an oxidative control on Hg and Pb release. Results from the sequential extraction and synchrotron-based XAS studies suggest the existence of reduced sulfur and selenium minerals, including CuS, HgS, and HgSe, and oxidative dissolution of these minerals may have contributed to the elevated metal concentrations. Oxidative degradation of organic matter may also have contributed to Hg release. The results suggest that Hg stability is enhanced under anoxic conditions. The resuspension tests indicate that undesirable concentrations of Hg may be released from sediment into the surrounding water at some locations during sediment disturbance events. Hydraulic dredges that are designed to remove sediment with minimal

disturbance would lessen release of Hg. However, the water removed along with the sediment would likely contain elevated levels of aqueous Hg and Pb and thus potential treatment strategies may need to be developed to both stabilize the contaminated sediment and treat the contaminated dredging water.

TABLE 3.1

Selected summary of bulk sediment concentrations from locations listed in Figure 3.1.

sample	Hg	As	Cd	Cr	Cu	Pb	Se	C	S
	μg g^{-1}, dry							%, dry	
A	120	2.5	1.4	66	480	310	11	23	1.2
B	79	1.1	0.4	43	89	180	0.8	8.4	0.3
C	81	3.2	1.2	78	360	210	3.5	13	0.8
D	340	3.3	2.5	65	1100	640	17	6.0	0.4
E	240	3.9	2.9	69	660	480	11	5.4	0.6
F	40	2.2	1.0	59	270	160	2.4	3.8	0.4
G	140	2.2	1.1	55	380	230	4.0	7.6	0.3
H	51	2.2	1.1	68	260	170	1.5	6.1	0.3
I	22	3.4	2.4	85	270	160	1.9	5.7	0.9
J	51	1.4	0.4	26	90	82	3.4	29	1.2

TABLE 3.2

Results of semi-quantitative mineral identification by x-ray diffraction analysis.

sample	Quartz	Albite	Albite(low)	Microcline	Muscovite	Chlorite	Amorphous material
	%, dry weight						
A	12	4	5	31	12	18	17
B	32	-	15	15	10	18	10
C	12	8	12	6	33	16	13
D	20	8	17	8	34	6	8
E	22	4	9	4	22	23	15
F	23	5	14	8	17	26	8
G	33	9	12	13	16	6	11
H	13	7	12	5	39	15	9
I	28	8	13	7	16	8	20
J	12	3	5	6	44	10	20

TABLE 3.3

Percent of total mercury extracted from contaminated lake sediment during sequential extraction procedure. Samples F and J were analyzed in duplicate.

sample	fraction rxtracted (%)					total Hg extracted ($\mu g\ g^{-1}$)	bulk sediment ($\mu g\ g^{-1}$)
	F1	F2	F3	F4	F5		
A	0.15	2.6e-4	20	61	19	99	120
B	0.08	2.8e-4	16	36	48	92	79
C	0.09	0.5e-4	18	67	15	77	81
D	0.03	6.4e-4	11	27	62	270	340
E	0.07	6.5e-4	15	35	50	210	240
F(1)	0.06	17e-4	17	71	12	31	40
F(2)	0.05	15e-4	18	59	23	34	
G	0.05	5.7e-4	18	41	42	230	140
H	0.03	14e-4	12	68	21	42	51
I	0.07	20e-4	15	82	3	19	22
J(1)	0.09	3.8e-4	68	29	2	66	51
J(2)	0.11	3.3e-4	68	29	3	65	

TABLE 3.4

Results of the Synthetic Precipitation Leaching Procedure (SPLP) analysis.

sample	Hg	Al	Ca	Cd	Cu	Fe	K	Mg	Mn	Na	Pb	Se
	μg L^{-1} in SPLP extract											
DWL	2	-	-	5	1300	-	-	-	-	-	15	50
A	0.74	190	16000	0.05	14	82	610	5200	6	48000	4.3	1.2
B	0.69	170	5300	0.04	1.7	140	1600	2200	110	3600	1.2	0.1
C	0.21	100	14000	0.02	6.0	59	310	6300	50	2500	1.1	1.2
D	1.1	250	7800	0.18	23	160	770	2700	160	4200	6.9	0.6
E	1.5	140	9700	0.05	9.4	120	390	2700	170	2900	2.7	0.4
F	0.07	50	11000	0.03	2.3	65	390	3600	280	2500	5.9	0.1
G	0.35	100	9800	0.04	4.2	73	490	4300	280	4600	0.8	0.3
H	0.17	270	5900	0.06	6.2	160	460	1500	280	2000	1.6	0.1
I	0.08	160	9500	0.03	3.8	140	490	3300	130	14000	1.0	0.1
J	0.30	70	14000	0.01	1.8	36	130	5900	8	2400	0.7	0.2

DWL = U.S. national primary drinking water regulation (U.S. EPA, 2009)

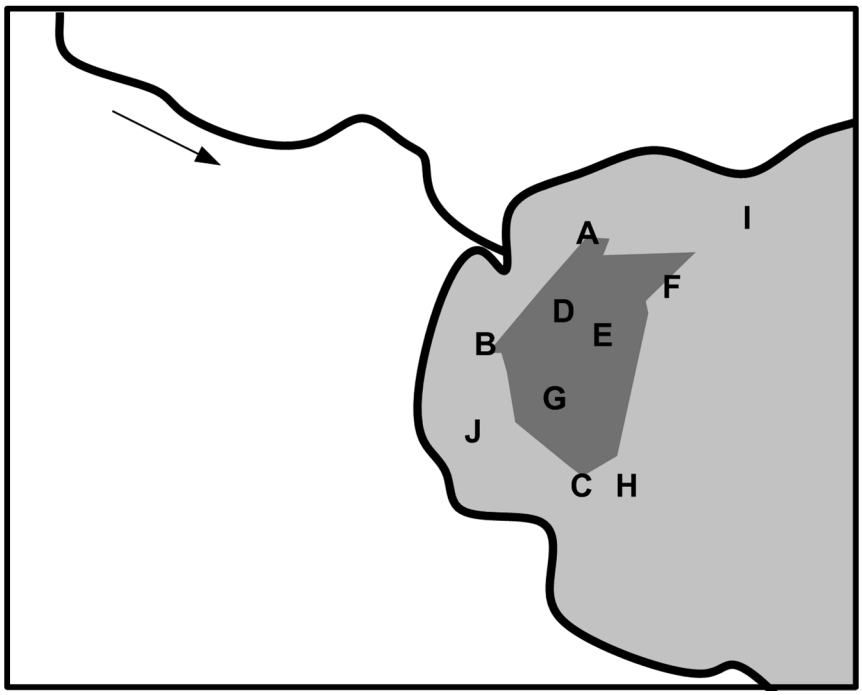

FIGURE 3.1 Map of experimental area with approximate positions of sampling locations. Dark grey area represents sediment Hg concentrations > 100 μg g^{-1}.

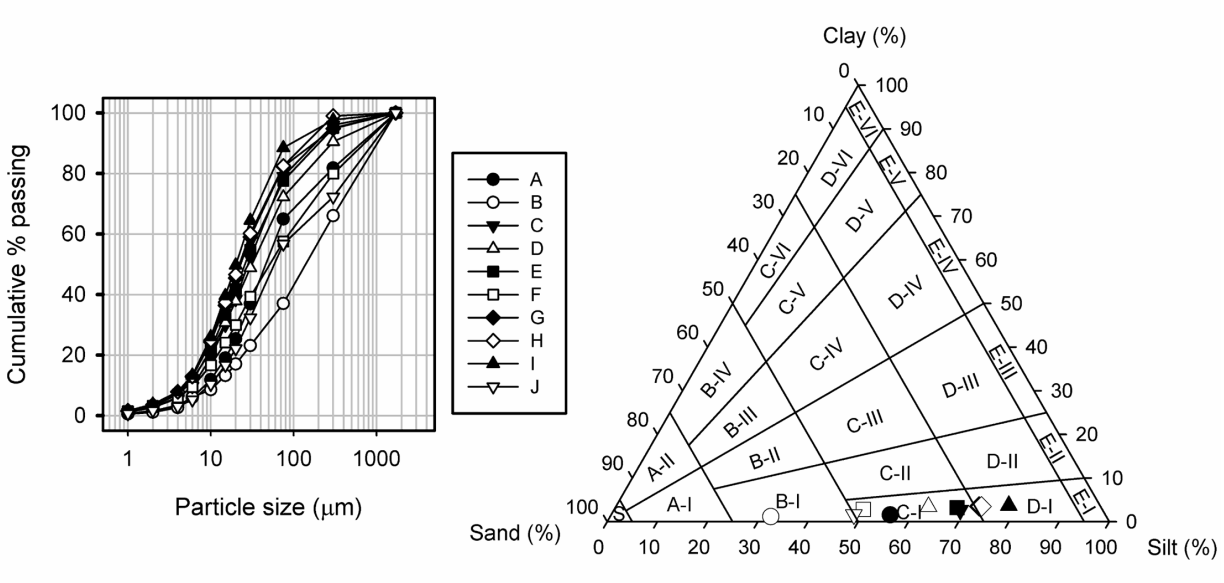

FIGURE 3.2 Particle size distribution curves and soil texture triangle for the ten sampling locations. Soil classification was based on the texture classification developed by Flemming (2000) for gravel-free muddy sediment. See text for discussion of classification zones.

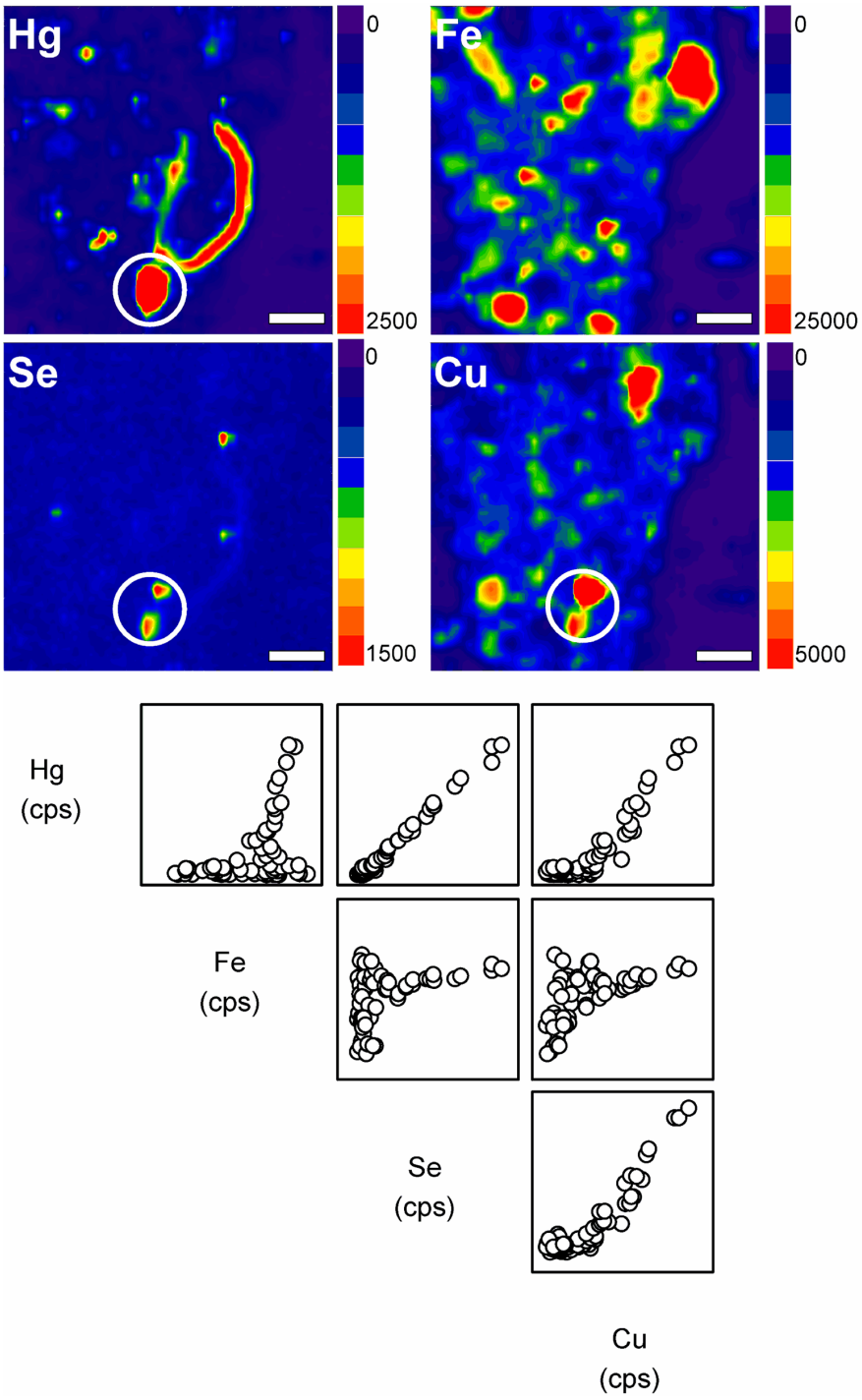

FIGURE 3.3 Micro-X-ray fluorescence maps for Hg, Fe, Se, and Cu obtained from a thin section prepared from sample D (top), and the corresponding XRF correlation plots (bottom). White scale bar on XRF maps is 100 µm, and the coloured scale bar is XRF in counts per second. Circled feature on XRF maps represents area further analyzed by µ-XANES.

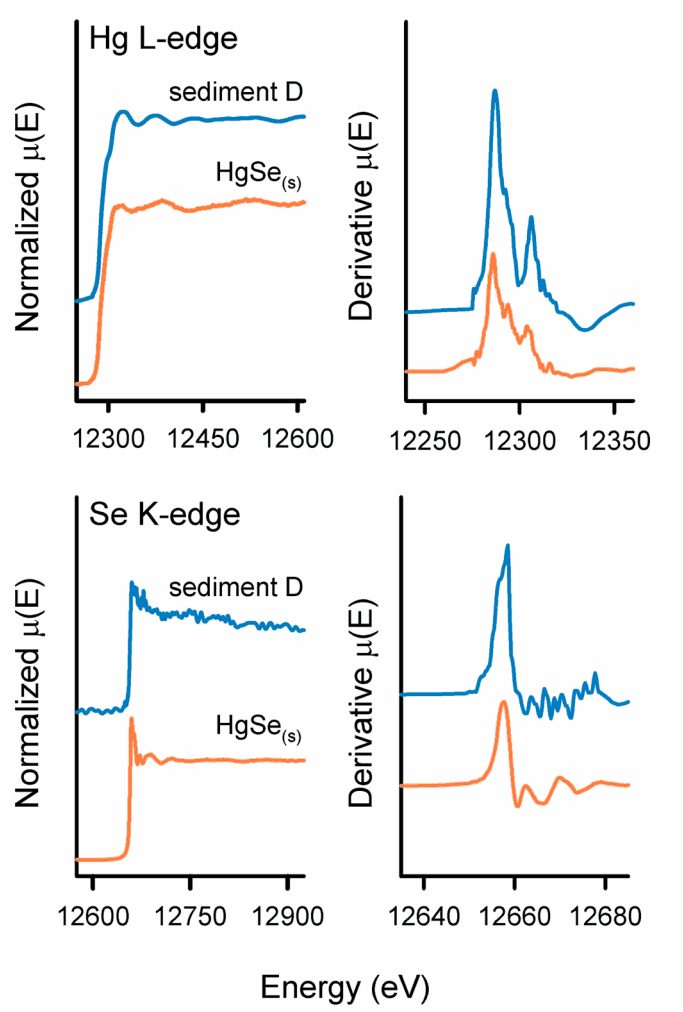

FIGURE 3.4 Micro-XANES plots for the Hg L3 (top) and Se K (bottom) absorption edges from the circled feature in Figure 3.3 (blue), compared to absorption edge data obtained from a tiemannite [HgSe] mineral standard (orange). Edge energies were taken at the maximum of the first derivative.

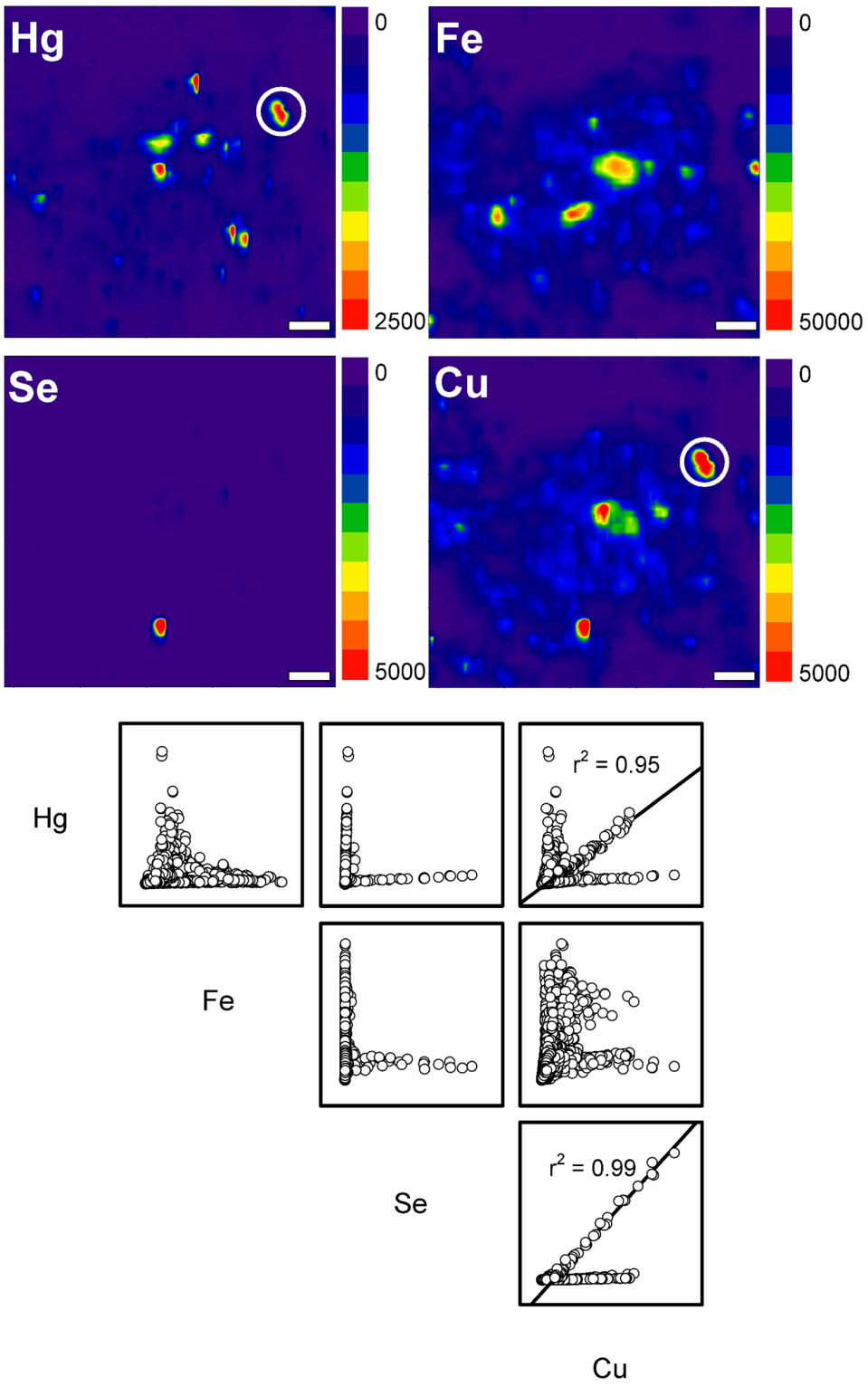

FIGURE 3.5 Micro-XRF maps for Hg, Fe, Se, and Cu obtained from a second area on on the sample D thin section (top), and the corresponding XRF correlation plots (bottom). White scale bar on maps is 100 μm, and the coloured scale bar is XRF in counts per second. Circled feature on maps represents area further analyzed by μ-XANES.

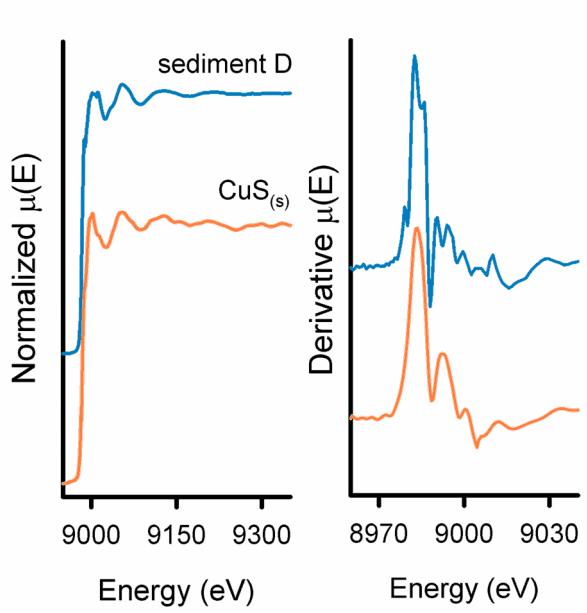

FIGURE 3.6 Micro-XANES plots for the Cu K absorption edge from the circled feature in Figure 3.5 (blue line) compared to a copper sulfide [CuS] standard (orange). Edge energies are taken at the maximum of the first derivative.

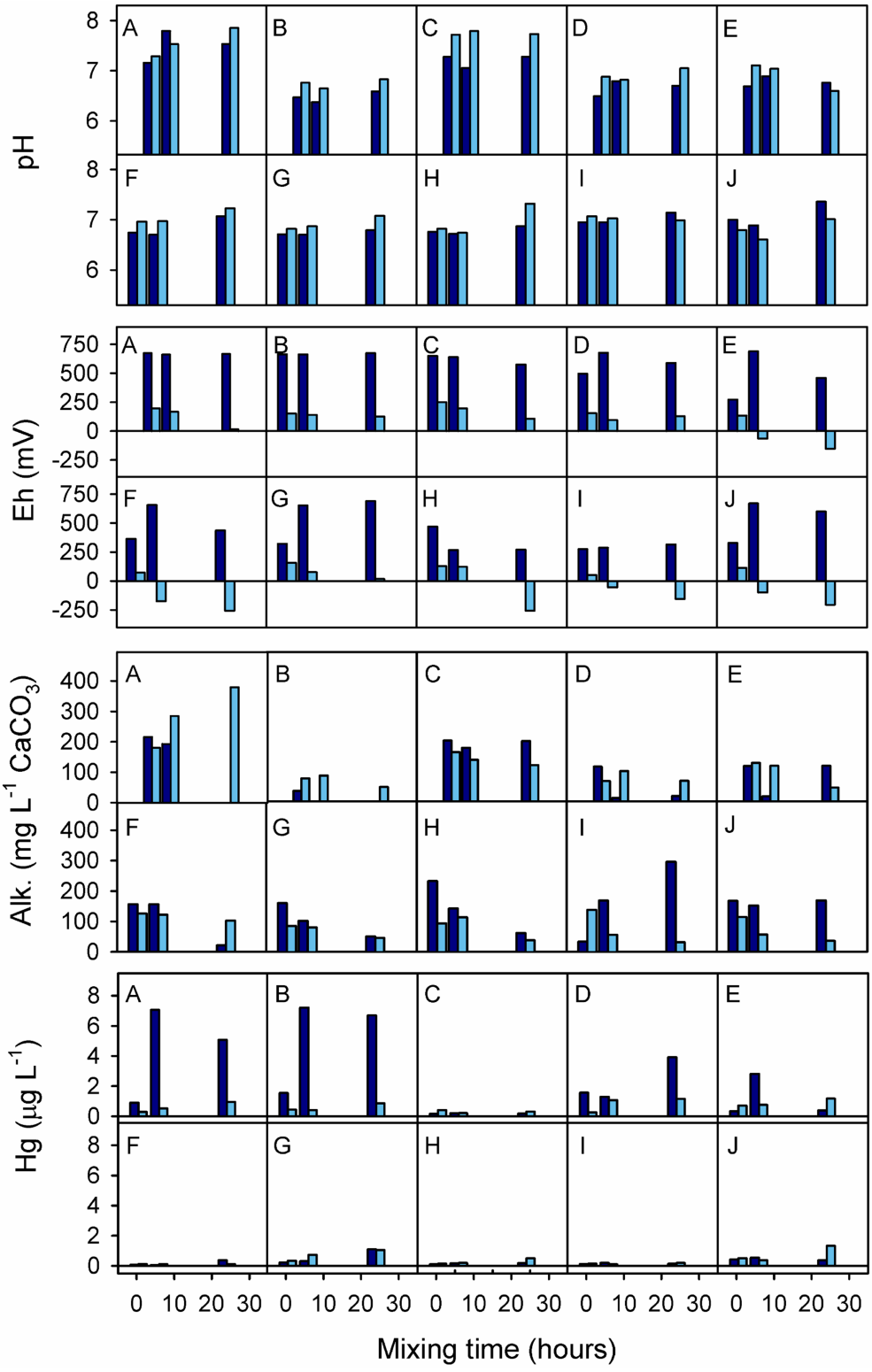

FIGURE 3.7 Aqueous geochemistry and Hg concentrations during oxic (dark blue) and anoxic (light blue) sediment resuspension tests.

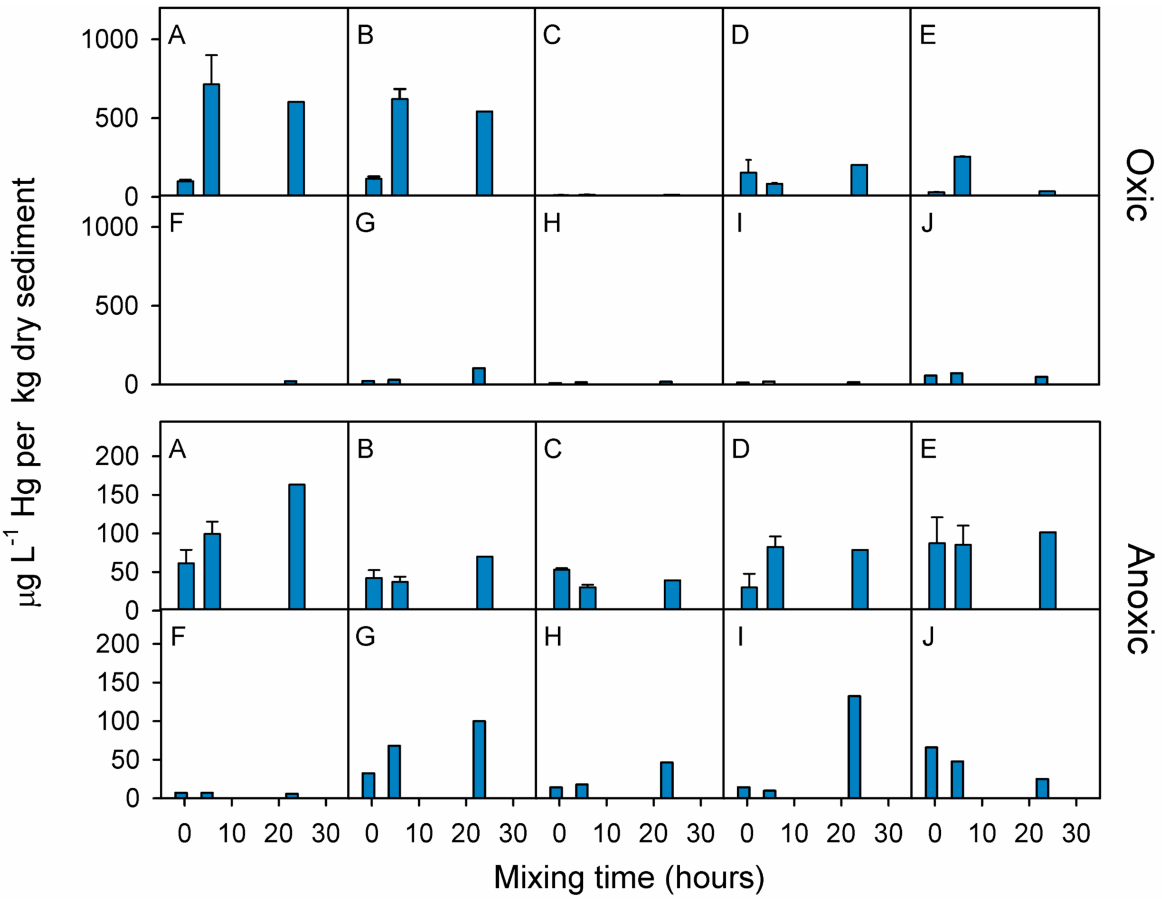

FIGURE 3.8 Mercury release during oxic (top) and anoxic (bottom) sediment resuspension tests. Reported concentrations are relative to the mass of sediment used in the tests. Error bars on selected samples represent the standard deviation between internal and external laboratory testing.

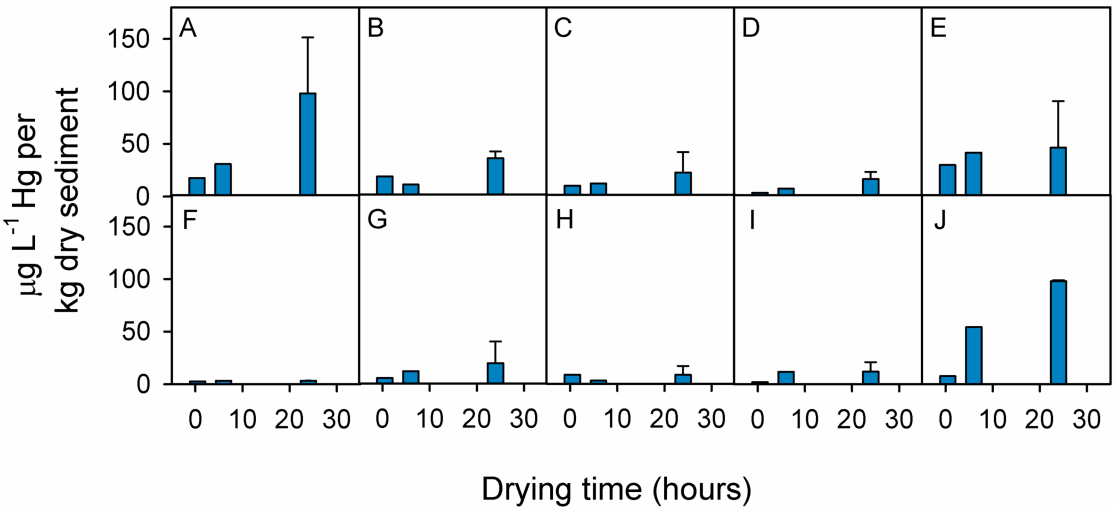

FIGURE 3.9 Mercury release during wet/dry sediment reoxidation tests, relative to the mass of sediment. Error bars on the 24 h samples represent the standard deviation between internal and external laboratory testing.

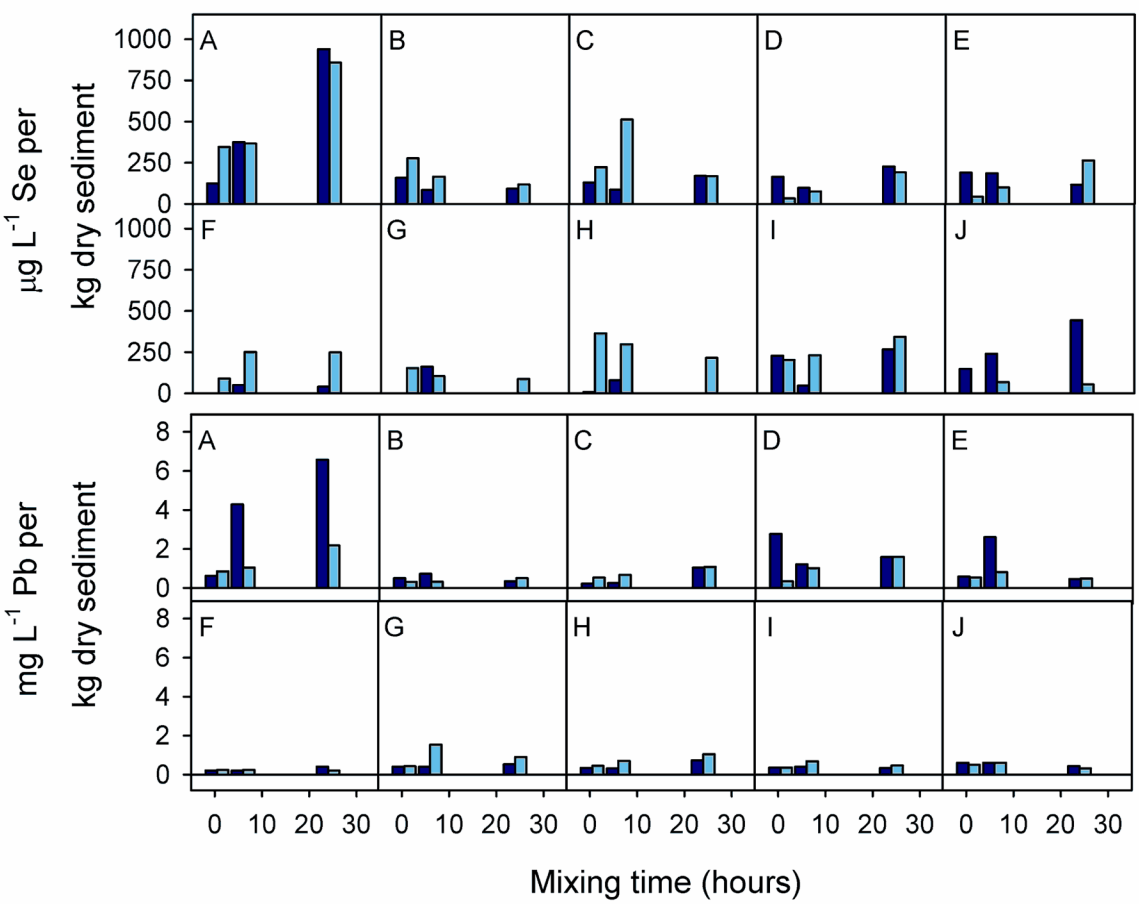

FIGURE 3.10 Trace ion release during oxic (dark blue) and anoxic (light blue) sediment resuspension tests, relative to the mass of sediment.

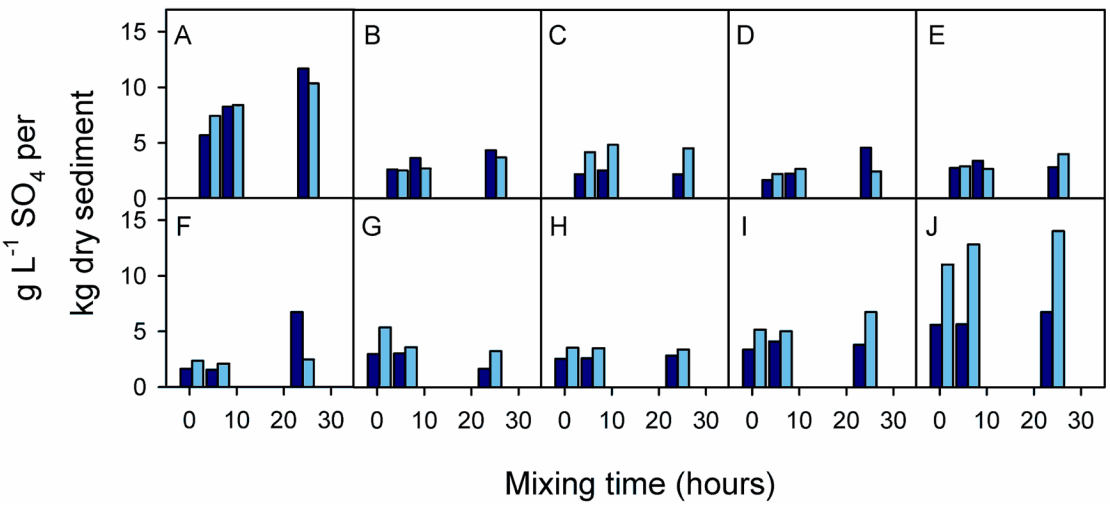

FIGURE 3.11 Sulfate release during oxic (dark blue) and anoxic (light blue) sediment resuspension tests, relative to mass of sediment.

Chapter 4:

Investigation of Reactive Materials for the Treatment of Aqueous Hg(II) – An EXAFS Study

4.1 Executive Summary

Laboratory batch experiments were conducted to evaluate the extent of removal of aqueous Hg(II) in an artificial groundwater using a variety of treatment materials, including granular Fe^0, activated carbon, attapulgite clay treated with two separate thiol-functionalized thiadiazole compounds (2-amino-5-thiol-1,3,4-thiadiazole and 2,5-dimercapto-1,3,4-thiadiazole), and metal-sulfur mixtures. Extended X-ray absorption fine structure (EXAFS) analysis was applied to the treatment materials to characterize the form of Hg on the treatment media. Mercury removal on the untreated clay was ~30 %, while pre-treatment with amino- and dimercapto-functionalized thiadiazole compounds increased removal to 69 % and >99 %, respectively. EXAFS analysis of the treated clays suggested the formation of a Hg-S bond, although the bond lengths were longer than would be expected for a cinnabar [α-HgS] structure. Treatment in the presence of granular Fe^0 and in the absence of aqueous sulfate resulted in 90 % removal, with mercury likely bonded to oxides on the margins of the iron grains. A 50:50 w/w mixture of Cu^0 and S^0 resulted in 90 % removal and EXAFS analysis showed the formation of Hg-S bonds similar to the structure of cinnabar, whereas a similar mixture of Fe^0 and S^0 resulted in similar removal of aqueous Hg(II) but likely as a Hg-oxide.

4.2 Introduction

Mercury is a toxic element that can affect the health of humans, fish, and other wildlife. Mercury contamination in the environment can be caused by anthropogenic activities such as mining (Hojdová et al., 2009), biomass burning (Friedli et al., 2009), and industrial activities such as ammunitions manufacturing (Arbestain et al., 2009) and chlor-alkali production (Reis et al., 2009). When mercury sources enter the aquatic environment, they can undergo changes

to highly toxic methylated forms (Ullrich et al., 2001). Consumption of fish containing elevated levels of methylmercury (CH_3Hg) can lead to neurological damage and eventually death (Tsuda et al., 2009).

The chemical nature of Hg contamination can create difficulties for many treatment technologies, primarily because the reduction of aqueous Hg(II) to its elemental form is not always sufficient for immobilization, due to the relatively high vapor pressure of Hg^0. Adsorption techniques using Fe(III) hydroxide sludge have been employed to immobilize Hg present in humic and fulvic acid colloids (Zhuang et al., 2003a). The presence of water-soluble lignin derivatives has been demonstrated to induce the formation of Hg-humic/fulvic acid colloids and subsequent removal by adsorption (Zhuang et al., 2003b). Activated carbon and clays have also been used to remove Hg from aqueous solutions. Oubagaranadin et al. (2007) compared the adsorption kinetics of aqueous Hg(II) on Fuller's earth with adsorption on activated carbon and found that although Hg formed stronger bonds on the clay, the adsorption capacity of activated carbon was much higher.

Other stabilization methods involve reactions with S^0, due to the high affinity between Hg and S. Lezzi et al. (1994) evaluated the affinity of aqueous Hg(II) to different chelating resins containing thiol-functional groups and reported a concentration decrease from 20 mg L^{-1} to 10 μg L^{-1} after 2 hours of treatment. Chen et al. (2004) described a mercaptan-functionalized mesostructured silicate for the removal of aqueous Hg(II). Weisener et al. (2005) used columns containing granular zero valent iron (Fe^0) to treat groundwater containing 40 μg L^{-1} Hg and 150 to 600 mg L^{-1} SO_4 and reported the formation of an intermediate phase between cinnabar [α-HgS] and metacinnabar [β-HgS] as the primary removal mechanism. Fuhrmann et al. (2002) developed a sulfur polymer stabilization method to treat radioactively contaminated soil

and mixed waste containing Hg. Initial experiments resulted in the formation of a black precipitate identified as metacinnabar [β-HgS]. The addition of sodium sulfide nonahydrate ($Na_2S{\cdot}9H_2O$) produced a red precipitate identified as cinnabar [α-HgS]. Synthetic dithiolates such as 1,3-benzenediamidoethanethiol ($BDETH_2$) have also shown to be versatile for removing aqueous Hg under a range in pH levels (Blue et al., 2010).

The chemical similarity between S and Se also produces a strong interaction between Hg and Se. Rudd et al. (1983) applied Se(IV) to a river system contaminated with Hg and noted a reduction in the accumulation rate of Hg into aquatic biota. In a similar experiment, Paulsson and Lundbergh (1989, 1991) applied rubber pellets containing sodium selenite (Na_2SeO_3) to several Hg contaminated lakes in Sweden. They observed changes in the Hg levels in fish ranging from a 22% decrease in pike to an 85% decrease in perch after 1 year of treatment.

To delineate the processes involved with Hg removal, synchrotron radiation based techniques such as X-ray absorption near edge spectroscopy (XANES) and extended X-ray absorption fine structure (EXAFS) can be used to determine the valence state and local molecular structure of an element of interest within a compound. These techniques have been used to characterize Hg speciation in mine wastes (Kim et al., 2000) and contaminated soils (Santoro et al., 2010), and to characterize the coordination geometry during treatment of aqueous Hg (Chen et al., 2004; Kim et al., 2004; Weisener et al., 2005).

In this study, laboratory-based batch experiments were used to evaluate the removal of aqueous Hg(II) from a simulated groundwater using methods of adsorption and co-precipitation by a variety of treatment materials. Micro-X-ray fluorescence (μ-XRF) and micro-X-ray absorption (μ-XAS) techniques were used to quantify the presence and form of

immobilized Hg on the materials. Treatment of aqueous Hg(II) by granular zero valent Fe was evaluated in the presence of aqueous Se(VI) to determine the effect of Se(VI) on Hg(II) removal. The results from these experiments give insight to the mechanisms involved with the removal of aqueous Hg, which will be important for optimizing low-cost treatment technologies.

4.3 Materials and Methods

4.3.1 Reactive Materials

The potential treatment materials were selected to evaluate the removal by adsorption and co-precipitation mechanisms. Two different sources of granular Fe^0 were used in the batch experiments: Connelly iron (obtained from Connelly-GPM, Inc., Chicago, IL), and H_2Omet^{TM} – 56 grade (45 – 600 μm) iron (Quebec Metal Powders Ltd., Sorel-Tracy, QC). Elemental sulfur was obtained from Georgia Gulf Sulfur Corp. (Valdosta, GA, USA). Other materials included elemental copper (fine powder), granular charcoal (10-18 mesh), and powdered attapulgite (palygorskite) clay. Separate samples of the attapulgite clay were pretreated with two different thiol-functionalized thiadiazole compounds: 2-amino-5-thiol-1,3,4-thiadiazole and 2,5-dimercapto-1,3,4-thiadiazole (W.D. Gould, CANMET, National Resources Canada). The thiadiazole compounds were received as fine powders. A 10 g sample of each compound was dissolved in 100 mL of ethanol, mixed with 100 g of attapulgite clay, and allowed to stabilize overnight in a fume hood. The treated clay was then rinsed with 200 mL of deionized water and allowed to dry.

4.3.2 Mercury Removal in the Absence/Presence of Aqueous Selenium

Separate input solutions were prepared containing either 4 mg L^{-1} Hg(II) (prepared by dissolving $HgCl_2$ in $CaCO_3$ saturated deionized water) or a mixture of 4 mg L^{-1} Hg(II) and 10 mg L^{-1} Se(VI) (prepared from Na_2SeO_4). The $CaCO_3$-saturated water was first purged in an anaerobic chamber with ultra high purity $Ar_{(g)}$ for 24 h prior to use to remove traces of dissolved oxygen. The sample bottles (100 mL amber glass Wheaton serum bottles) were first acid washed in 20% ACS grade HCl in deionized water, followed by three repeated rinses in DI water. The bottles were then baked in an oven at 250 ºC for 2 hours and autoclaved at 121 ºC for 30 minutes. The butyl rubber septa and crimp tops used to seal the bottles were also autoclaved.

Connelly Fe^0 was used as a reactive material for these tests. The granular iron was first sieved to 500 to 1000 μm. Brown oxidation deposits were removed by rinsing the iron three times with 6 M HCl followed by three repeated rinses with a solution of 1 M NH_2OH-HCl + 1 M HCl. The iron was stored in a solution of 1 M NH_2OH-HCl + 1 M HCl and transferred to an anaerobic chamber, where it was rinsed several times with methanol. A green precipitate (likely an Fe(II) compound) formed on the surface of the iron during the methanol rinse. The iron was allowed to dry exposed in the glove box. After drying the green precipitate became loosely bound. The iron was resieved at 325 μm for 10 minutes to remove the precipitate. The resulting cleaned iron was then riffle-split and 5.00 g portions were weighed into sample bottles for each experiment. Aliquots (100 mL) of the Hg(II) or Hg(II) + Se(VI) input solutions were added to several identical bottles which were then crimp sealed, hand shaken, and placed on an orbital shaker at 60 revolutions per minute. Individual bottles were sampled at 3, 6, 12,

24, 48, 96, and 192 hours reaction time, with triplicate samples at 48 and 192 hours. Control samples (containing input solution with no treatment media) were obtained at 3 and 192 hours. At the sampling time, one of the sample bottles was randomly selected from the set, removed from the orbital shaker, and hand shaken again. The solutions were decanted into latex free HSW Norm-Ject 30 mL syringes with the plunger removed to minimize potential contamination during sampling. A small portion of the unfiltered solution was immediately analyzed for pH and Eh determinations. The pH was measured using an Orion Ross combination electrode (model 815600) calibrated with NIST-traceable standard buffer solutions at pH 4, 7, and 10, and Eh was measured using an Orion platinum redox electrode (model 96-78BN) checked against ZoBell's solution following the procedure of Nordstrom (1977). Alkalinity was measured on samples filtered through an Acrodisc® single-use syringe filter with a 0.45 μm Supor® membrane. Samples for mercury analysis were filtered through Millipore single-use syringe filters with 0.2 μm PTFE membranes (IC-Millex-LG) and preserved with 12M HCl (Baker Instra-Analyzed). Mercury concentrations were determined with a Tekran Model 2500 CVAFS Mercury Detector (Tekran Instruments Corporation, Toronto, ON) following EPA Method 1631 (U.S. EPA, 2002). The remaining bulk reactive material samples at 192 h reaction time for the two batches were vacuum filtered in an anaerobic chamber and dried in a vacuum desiccator prior to preparation as 26 x 46 mm polished thin sections (Vancouver Petrographics Ltd., Langley, BC) for subsequent analysis by X-ray fluorescence and absorption spectroscopy techniques.

4.3.3 Mercury Removal using Bulk Reactive Materials

In a separate set of experiments, mercury removal was evaluated in the presence of different reactive materials. A 4 mg L^{-1} solution of Hg(II) was prepared as above. The following materials were evaluated: attapulgite clay, attapulgite treated with amino-functionalized thiadiazole, attapulgite treated with dimercapto-functionalized thiadiazole, granular activated carbon, elemental copper (Cu^0) plus elemental sulfur (S^0), and QMP granular iron plus elemental sulfur. Larger volumes of input solution (200 mL) and smaller masses of reactive material (1.00 g) were used to enhance the total amount of mercury present on the reactive material. For the Cu+S and Fe+S mixtures, 0.50 g of each material was used to obtain a total of 1.00 g. To accommodate the larger volumes, pre-washed 250 mL amber glass bottles were used (VWR TraceClean with PTFE lined closed caps). The sample bottles were manually shaken 4 times a day over a 192 h period. All reactive materials were vacuum filtered and dried in a vacuum desiccator in an anaerobic chamber. The materials were prepared for bulk XAS measurements by placing a small amount of dried material in an aluminum sample mount sealed with Kapton tape. The sample mount was stored in a portable anaerobic canister until required for analysis.

4.3.4 Bulk and Micro-X-ray Absorption Spectroscopy Measurements

The thin sections and bulk samples were analyzed at Beamline 13-BMD-GSECARS at the Advanced Photon Source (Argonne National Laboratory, Argonne, IL). A 13 element germanium detector was used to collect fluorescence spectra from the bulk treatment media. A Vortex ME-4 4 element detector was used to collect spectra from the thin sections containing Connelly iron. Micro-X-ray Absorption Near Edge Structure (μ-XANES) and micro-X-ray

Fluorescence (μ-XRF) measurements were obtained for the thin sections using a focused beam of ~10 μm. Two-dimensional XRF maps were obtained from the Fe Kα, Hg Lα, and Se Kα fluorescence lines to identify the distribution of Hg and Se on the surface of the iron grains. Hg L_{III} edge and Se K edge spectra were obtained on spots that were identified by XRF to be elevated in these elements. A defocused beam approximately 1 mm wide was used for bulk-XANES and -XRF measurements on the bulk sample material and reference materials. Cinnabar [α-HgS], metacinnabar [β-HgS], and tiemannite [HgSe] mineral specimens were obtained from Excalibur Mineral Corp. (Peekskill, NY). Laboratory grade samples of $HgCl_2$ and trigonal Se^0 were obtained from commercially available sources. Mercury(II) oxide standard was previously prepared by the beamline staff. Data normalization and averaging was performed with the program ATHENA, and EXAFS modeling was performed with the program ARTEMIS (Ravel and Newville, 2005). EXAFS spectra were given a k weighting of 3 to enhance weak oscillations. A k range of 2 to 12 Å was used during the Fourier transform of the standard materials with the exception of the Hg EXAFS signal on tiemannite, where a k range of 2 to 10 Å was used to eliminate interferences from the Se K edge. A narrower k range of 3 to 8 Å was used for the treatment materials to eliminate high *k* noise from weak spectra. Coordination numbers were kept invariant during refinement of the first shell for the reference materials to obtain measurements of the passive electron reduction factor (S_0^2) and static disorder (σ^2). These variables were then kept invariant during refinement of the first shell for the treatment media to obtain coordination numbers. Unless otherwise stated, ΔE_0 values were < 10 eV for all fitting models. The EXAFS R factors (where $R = \Sigma(\text{data-fit})^2/\Sigma\text{data}^2$) ranged from 0.03 to 0.07 for the standard materials and from 0.006 to 0.23 for the treatment media. The R factors for the EXAFS fitting of treatment media tended to be larger for the weakest X-

ray absorption spectra (e.g., untreated attapulgite), indicating a poorer statistical fit compared to fits performed on stronger absorption spectra.

4.4 Results and Discussion

4.4.1 Hg+Se Treatment – Aqueous Geochemistry

The pH, Eh, and alkalinity data for the treatment of aqueous Hg(II) alone (labelled "Hg") and the treatment of aqueous Hg(II) mixed with aqueous Se(VI) (labelled "Hg+Se") using Connelly granular iron followed similar trends versus reaction time (Figure 4.1). The pH decreased slightly over the course of each treatment, reaching values of 7.6 for the Hg batches and 7.8 for the Hg+Se batches, compared to the input pH which was approximately 8.1. Redox potential ranged from -300 to -400 mV in the two treatments, indicating that reducing conditions were maintained during the experiment. Alkalinity decreased in both treatments from 58 - 80 mg L^{-1} to ~20 mg L^{-1} $CaCO_3$. Mercury concentrations decreased rapidly in both treatments, dropping to ~0.4 mg L^{-1} after 3 h reaction time and to 0.2 mg L^{-1} after 192 h reaction time from an input concentration of between 3 and 4 mg L^{-1}. Selenium concentrations in the Hg+Se mixture declined at a slower initial rate, although an overall higher removal was observed with concentrations dropping to 2 mg L^{-1} after 24 h reaction time and 0.05 mg L^{-1} after 192 h. Selenium concentrations were at background levels in the Hg only treatment. Rapid removal of Hg in the presence of granular iron also was observed by Weisener et al. (2005), where column influent Hg concentrations ranging from 18 to 42.5 μg L^{-1} decreased to < 0.1 μg L^{-1} in the column effluent after ~4 days or one pore volume of flow. The observed effectiveness of granular iron to remove aqueous Se(VI) is comparable to other reports in the literature (Zhang et al., 2005; Sasaki et al., 2008a).

4.4.2 Hg+Se Treatment – Micro-XRF/XANES

Micro X-ray fluorescence maps were obtained from different locations on the reactive material thin sections for both the treatment of aqueous Hg(II) only (Figure 4.2) and the treatment of a mixture of aqueous Hg(II) and Se(VI) (Figure 4.3). The location of Fe grains in the thin section was indicated by the Fe Kα fluorescence. Mercury was sparsely distributed along the margins of the iron. Individual spots containing the highest concentrations of Hg based on the fluorescence counts were selected for μ-XANES measurements. In the absence of Se(VI), the separate spots showed nearly identical Hg L-edge spectra, although the EXAFS spectra were slightly out of phase (Fig. 4.2). The Fourier transforms of the EXAFS spectra were modeled to the first two scattering paths of HgO at 2.04 and 2.07 Å, respectively. The resulting peaks were fit at 2.13 and 2.16 Å for spot 1 and 2.19 and 2.21 Å for spot 2. When corrected for phase shift to the Hg-O bond, both spectra showed a smaller peak between 3.0 and 3.5 Å that was not identified in the current EXAFS modeling. Kim et al. (2004) investigated Hg(II) sorption on goethite [α-FeOOH] and proposed a bonding configuration of a bidentate inner-sphere complex, with Hg bonded to two singly coordinated O atoms at 2.03 Å and Hg bonded to central Fe atoms at an average distance of 3.28 Å. This conceptual model matched their EXAFS fitting analysis. Although the Hg-O bond distances obtained by the EXAFS fits in the current study appear to be longer than expected, the unknown peak falls within the range expected for a Hg-Fe bond on goethite, which is a corrosion product of granular iron (Roh et al., 2000).

For Hg(II) mixed with Se(VI), both Hg and Se were concentrated along the margin of an iron grain (Fig. 4.3). The Hg L-edge spectrum was nearly identical to the spectra shown in

Figure 4.2. Interferences with the Se K-edge prevented the collection of Hg EXAFS data beyond ~10 Å, therefore the resulting Fourier transform could not be modeled accurately. Instead, the EXAFS spectrum from the Se K-edge measurement was compared to the theoretical models for HgSe and Se^0. A bond distance of 2.36 Å was obtained when modeled with the first scattering path of trigonal Se^0, compared to the theoretical length of 2.37 Å. This implies that the selenium found in this location was elemental selenium and was not bound to mercury as HgSe. The similarity between the Hg L-edge spectrum and the spectra shown in Fig. 4.2 suggests that the Hg present on the Fe grain was likely in the same chemical state. Earlier results from Weisener et al. (2005) showed effective treatment of aqueous Hg with granular iron. The removal mechanism was attributed to the formation of a HgS mineral associated with the concomitant reduction of aqueous SO_4. The current results show that granular iron may also be an effective treatment medium in SO_4-poor environments, where the removed Hg is apparently bound to Fe oxides on the margins of the corroded granular iron. Mercury oxide is highly insoluble in water, thus the binding of Hg to Fe oxides is expected to be relatively stable. Sarkar (2003) investigated the solubility of elemental Hg in water and observed a decrease in Hg^0 solubility in the presence of Fe oxides including magnetite [Fe_2O_4], hematite [Fe_2O_3], goethite [FeOOH], and "limonite" [nominally $2Fe_2O_3 \cdot 3H_2O$]. The removal was attributed to oxidation of Hg^0 and subsequent sorption of Hg(II) ions to the Fe oxides, although the presence of Cl decreased Hg retention due to complex formation. Barrow and Cox (1992) tested Hg(II) sorption onto goethite and observed that the pH of maximum adsorption increased in the presence of Cl. With regard to the removal of aqueous Se, comparable studies that used EXAFS analyses to characterize the removal of Se(VI) by Fe have also shown that reduction to Se(0) can occur (Myneni et al, 1997; Sasaki et al., 2008b, Hayashi et al., 2009).

4.4.3 Bulk Treatment – Aqueous Geochemistry

The aqueous geochemistry results for the bulk treatment experiments performed over a reaction time of 192 h were variable (Figure 4.4). The pH values for the thiadiazole-treated clays were similar at 6.8, compared to the value of 8.2 measured in the untreated clay. The treatment involving the activated carbon produced the highest measured pH value of 8.8. The Cu+S and Fe+S treatment resulted in pH values of 8.1 and 7.6, respectively. Oxidation-reduction potentials (Eh) also varied greatly through the different treatments. The untreated attapulgite sample had a relatively high Eh of approximately +400 mV, while the treated clays had relatively low Eh values (+80 to +120 mV). The Eh of the activated carbon treatment was -4 mV. The two metal+sulfur treatments had Eh readings of -380 to -400 mV, indicating that reducing conditions were maintained in these samples.

The attapulgite experiments were performed at a separate time from the activated carbon and metal+sulfur treatments and there were slight differences in the input solution concentrations. As a result, the Hg results in Fig. 4.4 are reported as relative percent concentrations; i.e., C/C_0 x 100 where C is the measured concentration of Hg in the sample and C_0 is the concentration of the input solution. Addition of untreated attapulgite clay resulted in removal of ~29 % relative to the initial mass of Hg, whereas removal using the amino-functionalized clay was 69 % and the dimercapto-functionalized clay was over 99 % of the initial Hg. The addition of thiol-groups to attapulgite clay greatly enhanced the removal of aqueous Hg. For the second group of samples, the addition of activated carbon resulted in removal of ~78 % of the initial Hg, and the Cu+S and Fe+S treatments resulted in removal of 90 % and 94 %, respectively.

4.4.4 Bulk Treatment – XANES/EXAFS

The normalized Hg L-edge spectra for attapulgite and GAC are similar, with a small peak present on the absorption edge (Figure 4.5). A smaller shoulder was also present on the amino-functionalized sample. In contrast, the absorption edge for the clay mixed with dimercapto-functionalized thiadiazole was smoother with no evidence of the shoulder observed in the amino-functionalized sample. The spectra for the Cu+S and Fe+S mixtures appear to be similar, suggesting that the valence state of Hg is similar in both treatments.

The untreated attapulgite sample (ATP) was modeled with the first scattering path of $HgCl_2$. The resulting peak was located at 2.27 Å, compared to 2.29 Å for the theoretical model. Modeling with the first two paths for HgO resulted in bond distances of approximately 0.09 Å longer than the theoretical model and a large ΔE_0 shift of +17 eV, indicating a poor fit. In a similar experiment, Alvarez-Puebla et al. (2004) mixed copper (II) chloride with a palygorskitic clay. EXAFS measurements suggested the formation of atacamite, which is a copper hydroxychloride mineral of the formula $Cu_2Cl(OH)_3$. Although the adsorption of an aqueous mercury hydroxychloride species could explain the Hg-Cl model in the current work, the dominant form of mercury is expected to be aqueous $Hg(OH)_2$ with only a minor amount of aqueous HgClOH given the pH and Eh values measured in the untreated clay sample (Allard and Arsenie, 1991). Therefore, it is unlikely that the adsorption of HgClOH was the dominant removal process in the untreated clay even though EXAFS modeling the Hg-Cl bond produced an acceptable fit.

The results for the amino- and thiol-functionalized clay (+amino) and dimercapto-functionalized clay (+dimercapto) were each modeled with the first path of cinnabar, which has

a theoretical bond distance of 2.37 Å. Modeling with this path resulted in distances of 2.40 Å and 2.48 Å for the amino and dimercapto samples, respectively. Both the coordination number and the modeled atomic distance for the first shell appeared to increase with the increasing number of functionalized thiol groups for the three clay samples (see Table 4.1). The longer bond distance was likely due to different bonding characteristics for Hg on the functional groups on the thiadiazole compounds compared to the Hg-S bond found in cinnabar, although no appropriate standard was available to model the Hg-thiol bond expected to occur in the treated clay samples. A surface complexation model could explain the longer bond distances. Wolfenden et al. (2005) determined a theoretical first shell distance of 2.61 Å for Hg bound to S in sulfide minerals as a surface complex, and reported a Hg-S distance of 2.53 Å on oxidized mackinawite. Genin et al. (2001) studied Hg vapour interactions on galena and found that Hg became oxidized to Hg(II) and bound to S with a bond length of 2.62 Å. Therefore, a bond distance of 2.48 Å for Hg bound to the dimercapto-functionalized thiadiazole compound may be reasonable. Another thiol-based ligand that has been used for treatment of aqueous Hg is benzene-1,3-diamidoethanethiol ($BDETH_2$). Matlock et al. (2001) applied $BDETH_2$ to a solution of 50 mg L^{-1} Hg and observed 99.97 % removal after 6 hours of reaction time, indicating the effectiveness of the thiol-functional groups for attenuating aqueous Hg. Zaman et al. (2007) used several different spectroscopic techniques, including XANES/EXAFS, to investigate the nature of Hg binding to $BDETH_2$. Results from the EXAFS fitting resulted in a Hg-S bond distance of 2.42 Å, which is similar to the results in the current work.

The activated carbon sample was initially modeled with the first path of $HgCl_2$ resulting in a modeled distance of 2.16 Å, compared to the expected distance of 2.29 Å. When modeled with the first two paths for HgO, bond distances of 2.02 Å and 2.05 Å were found

compared to the expected distances of 2.04 Å and 2.07 Å. The error bars on the coordination number, bond distances, and ΔE_0 calculations were also smaller for the HgO model, indicating a better statistical fit. Li et al. (2002) investigated the effect of surface moisture on the adsorption of elemental Hg by activated carbon. X-ray absorption experiments indicated that mercury was bound to surface oxygen complexes associated with water sorbed to the carbon. The results presented in the current research are consistent with the observations by Li et al. (2002).

Although the Hg L-edge spectra for the Cu+S and Fe+S samples appeared to be similar, differences were observed in the EXAFS spectra. The Cu+S sample matched well with the first path for cinnabar with a bond distance of 2.35 Å, compared to the theoretical distance of 2.37 Å. When the Fe+S sample was modeled with cinnabar or metacinnabar, unreasonably large ΔE_0 shifts of -17 eV were produced. Given the poor fits to Hg-S, the aqueous Hg(II) in the current study was likely sorbed to an iron (hydr)oxide formed as a corrosion product of the granular iron. A better fit was found when modeled with HgO, although the bond distances of 2.12 Å and 2.15 Å were 0.08 Å higher than the theoretical values. These distances compare well to the modeling results from the Connelly iron treatment (Fig. 4.2).

4.5 Conclusions

The addition of various reactive materials resulted in the removal of aqueous Hg(II). Removal with granular Fe in the absence of aqueous SO_4 appeared to be due to a Hg-O complex, though the bond distances found through EXAFS modeling are 0.08 to 0.15 Å longer than the theoretical distance. Removal in the presence of aqueous Se(VI) had no apparent effect on the removal of Hg, with EXAFS modeling showing the presence of Se^0 on the surface of the iron.

Treatment with attapulgite clay was greatly enhanced with the addition of thiol-functionalized thiadiazole compounds, with higher removal observed in the presence of dimercapto-functionalized thiadiazole. The addition of S^0 to Cu^0 produced a Hg-S bond similar to cinnabar, while the sulfur had no apparent effect on removal in the presence of granular iron. Removal by granular activated carbon was attributed to a Hg-O complex, likely related to the sorption of water on the carbon material. The selection of an appropriate treatment media will likely depend on redox conditions at the contamination source. The removal of Hg(II) in the presence of granular Fe appears to be due to binding to Fe-oxides. In contrast, sulfur-based treatment media may be more stable under reducing conditions because cinnabar is susceptible to oxidation reactions.

TABLE 4.1
EXAFS analysis of batch treatment samples.

sample	scatterer	CN	r_{eff} (Å)	R (Å)	S_0^2	σ^2 (Å^2)	R factor
CZVI-Hg (1)	Hg-O1	1.1 ± 0.3	2.04	2.13 ± 0.05	1.04[a]	0.008[a]	0.09
	Hg-O2		2.07	2.15 ± 0.05			
CZVI-Hg (2)	Hg-O1	1.3 ± 0.2	2.04	2.19 ± 0.01	1.04[a]	0.008[a]	0.10
	Hg-O2		2.07	2.21 ± 0.01			
CZVI-Se	Se-Se	1.7 ± 0.1	2.37	2.36 ± 0.01	1.11[a]	0.004[a]	0.006
ATP	Hg-Cl	0.8 ± 0.1	2.29	2.27 ± 0.03	1.00[a]	0.004[a]	0.23
ATP+amino	Hg-S (α)	1.3 ± 0.2	2.37	2.40 ± 0.04	0.77[a]	0.001[a]	0.10
ATP+dimercapto	Hg-S (α)	1.6 ± 0.2	2.37	2.48 ± 0.02	0.77[a]	0.001[a]	0.08
GAC	Hg-O1	0.8 ± 0.1	2.04	2.02 ± 0.03	1.04[a]	0.008[a]	0.10
	Hg-O2		2.07	2.05 ± 0.03			
Cu+S	Hg-S (α)	2.0 ± 0.3	2.37	2.35 ± 0.04	0.77[a]	0.001[a]	0.07
Fe+S	Hg-O1	2.4 ± 0.5	2.04	2.12 ± 0.04	1.04[a]	0.008[a]	0.11
	Hg-O2		2.07	2.15 ± 0.04			

[a] values fixed during structure modeling; CN = coordination number; r_{eff} = actual bond length; R = modeled bond length; S_0^2 = passive electron reduction factor; σ^2 = mean-square displacement of bond length; R factor = fitting statistic

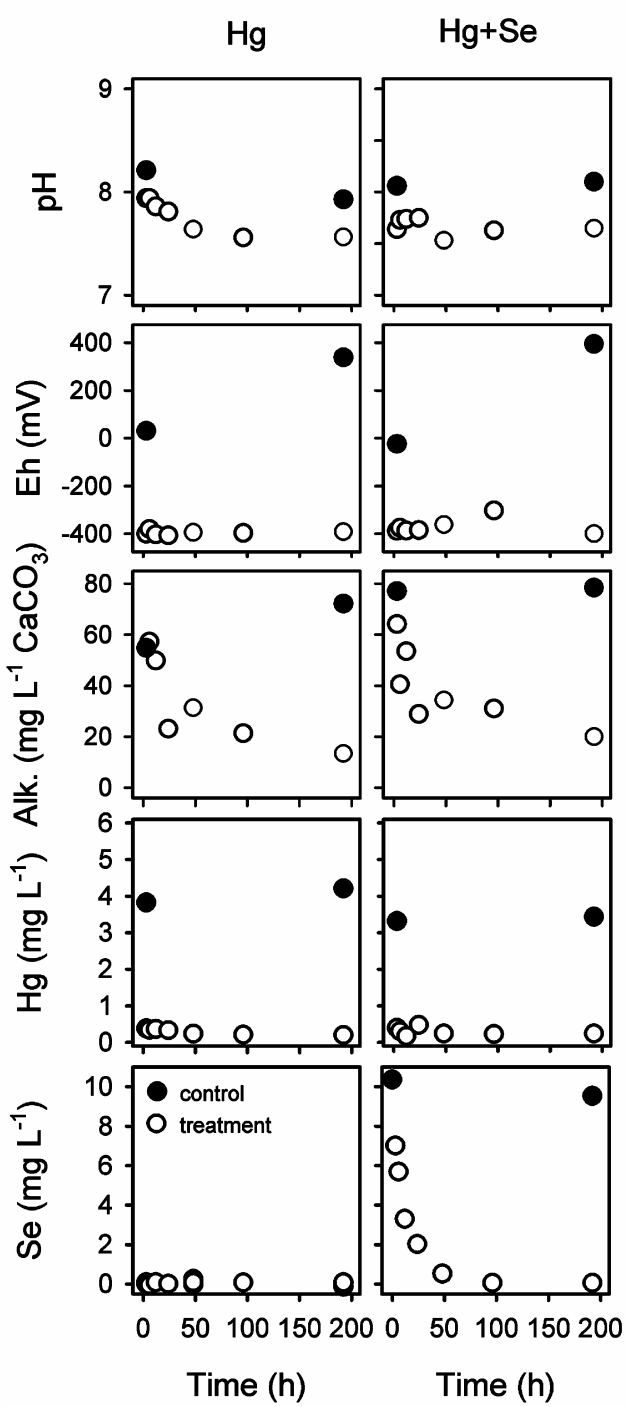

FIGURE 4.1 Comparisons of aqueous geochemistry, Hg, and Se concentration data as a function of time from batch experiments of aqueous Hg(II) (Hg) and aqueous Hg(II) mixed with aqueous Se(VI) (Hg+Se) after treatment with Connelly GI.

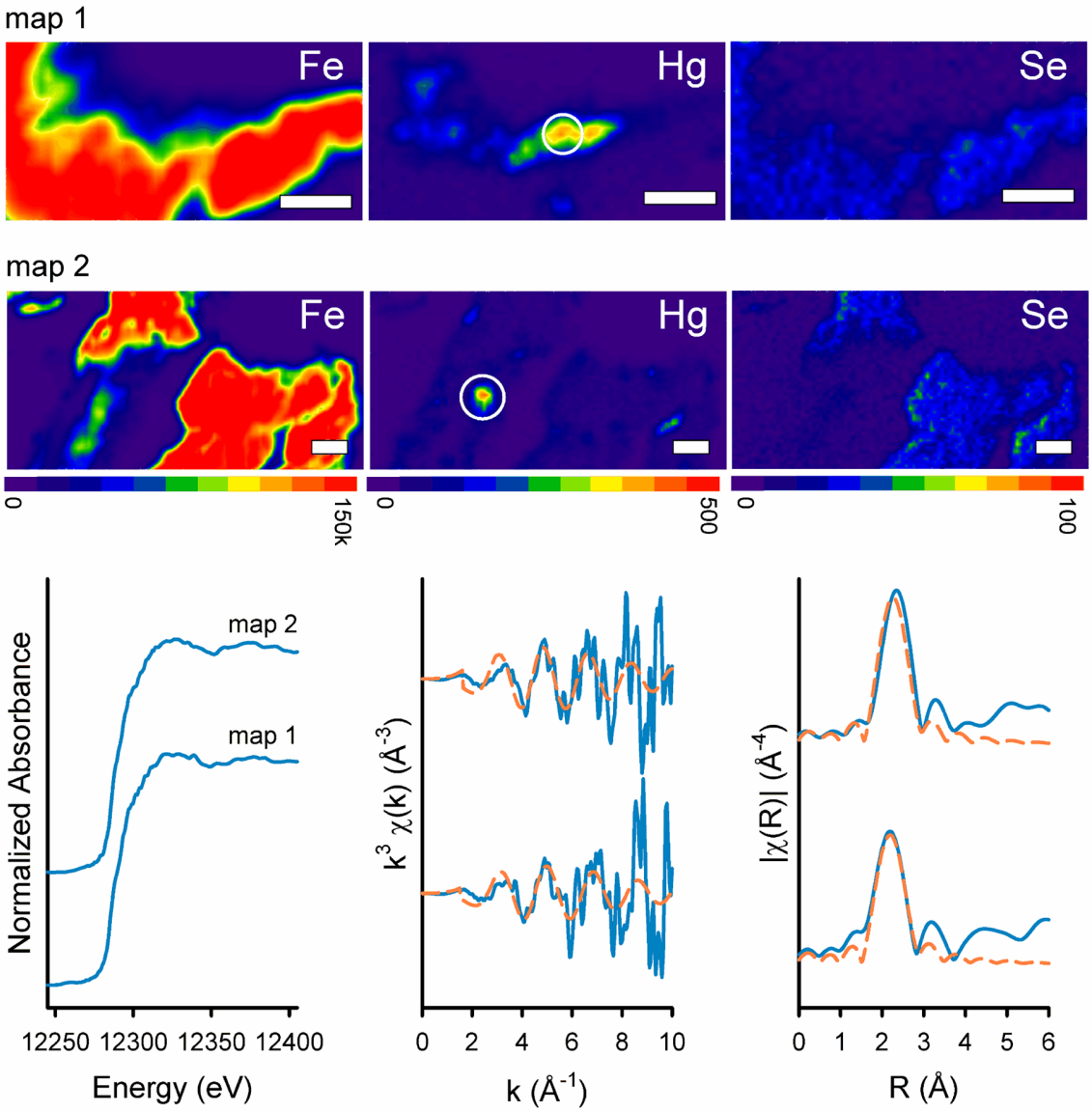

FIGURE 4.2 Separate 2D maps of Fe Kα, Hg Lα, and Se Kα X-ray fluorescence on grains of Connelly GI after 8 days reaction with 4 μg L^{-1} Hg(II) (upper figure). Horizontal colour bars represent XRF intensity in counts per second. White scale bars represent 100 μm. Lower figure shows the measured XANES and EXAFS data obtained from the circled spots in upper figure (solid, blue line), along with the EXAFS fit (dashed, orange line). Fourier transform data are corrected for phase shift.

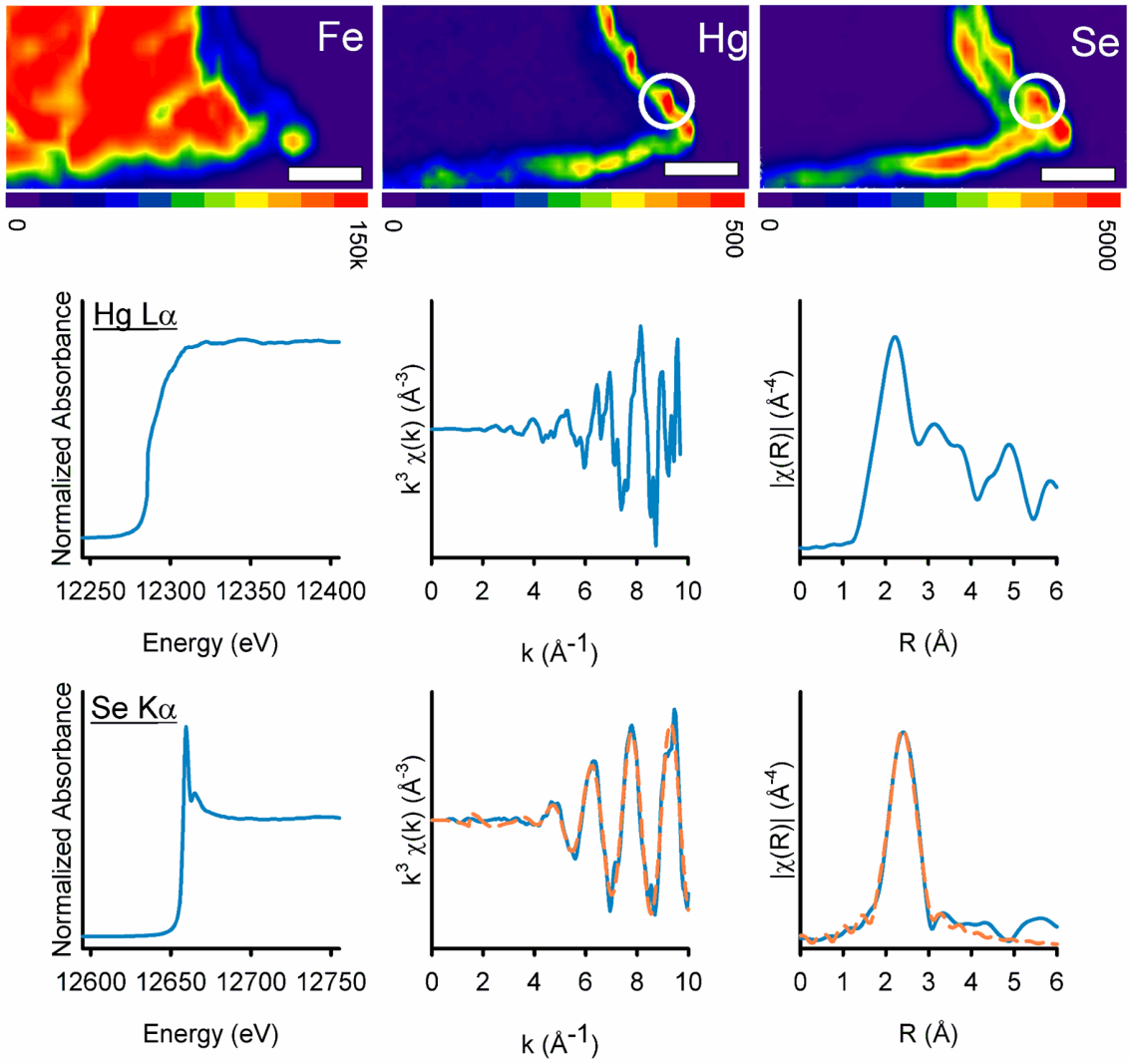

FIGURE 4.3 Map of Fe Kα, Hg Lα, and Se Kα X-ray fluorescence on grains of Connelly GI after 8 days reaction with a mixture of 4 μg L^{-1} Hg(II) and 10 μg L^{-1} Se(VI) (upper figure). Horizontal colour bars represent XRF intensity in counts per second. White scale bars represent 100 μm. Lower figure shows the measured XANES and EXAFS data obtained from the circled spots in upper figure (solid, blue line), along with the EXAFS fit (dashed, orange line). Fourier transform data are corrected for phase shift.

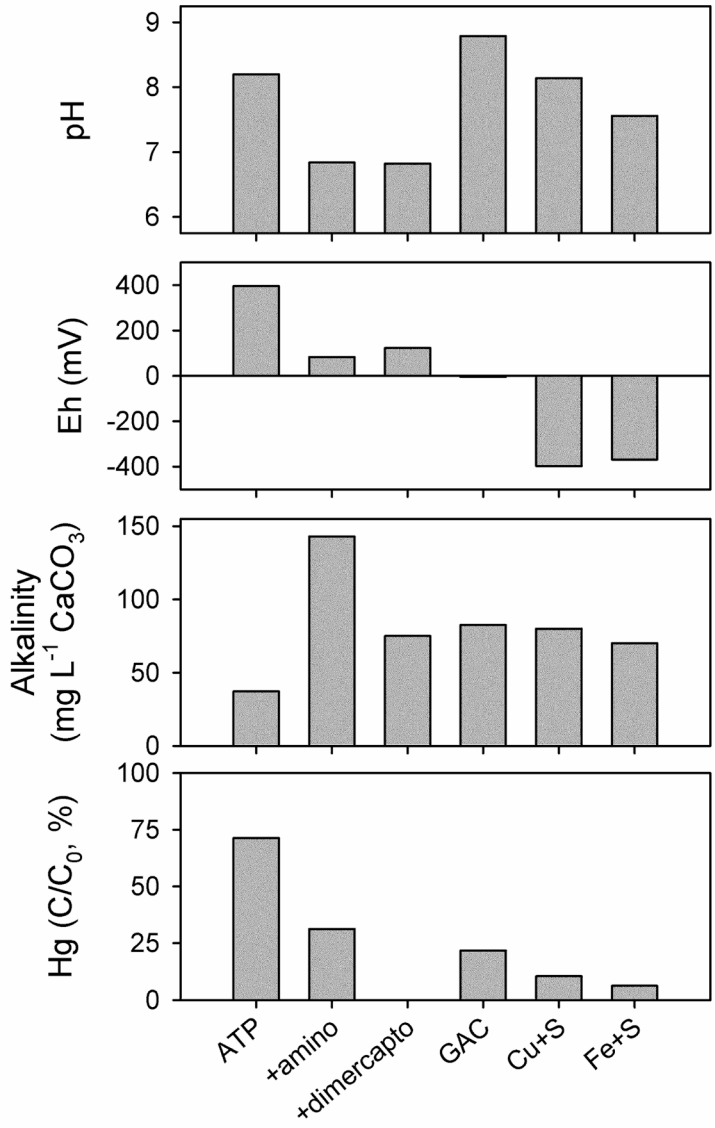

FIGURE 4.4 Comparisons of aqueous geochemistry and relative Hg concentrations from batch experiments of aqueous Hg(II) mixed with: attapulgite clay (ATP), attapulgite clay mixed with amino- and thiol-functional thiadiazole (+amino), attapulgite clay mixed with dimercapto-functional thiadiazole (+dimercapto), granular activated carbon (GAC), a 50:50 w/w mixture of elemental copper and elemental sulfur (Cu+S), and a 50:50 w/w mixture of QMP granular iron and elemental sulfur (Fe+S).

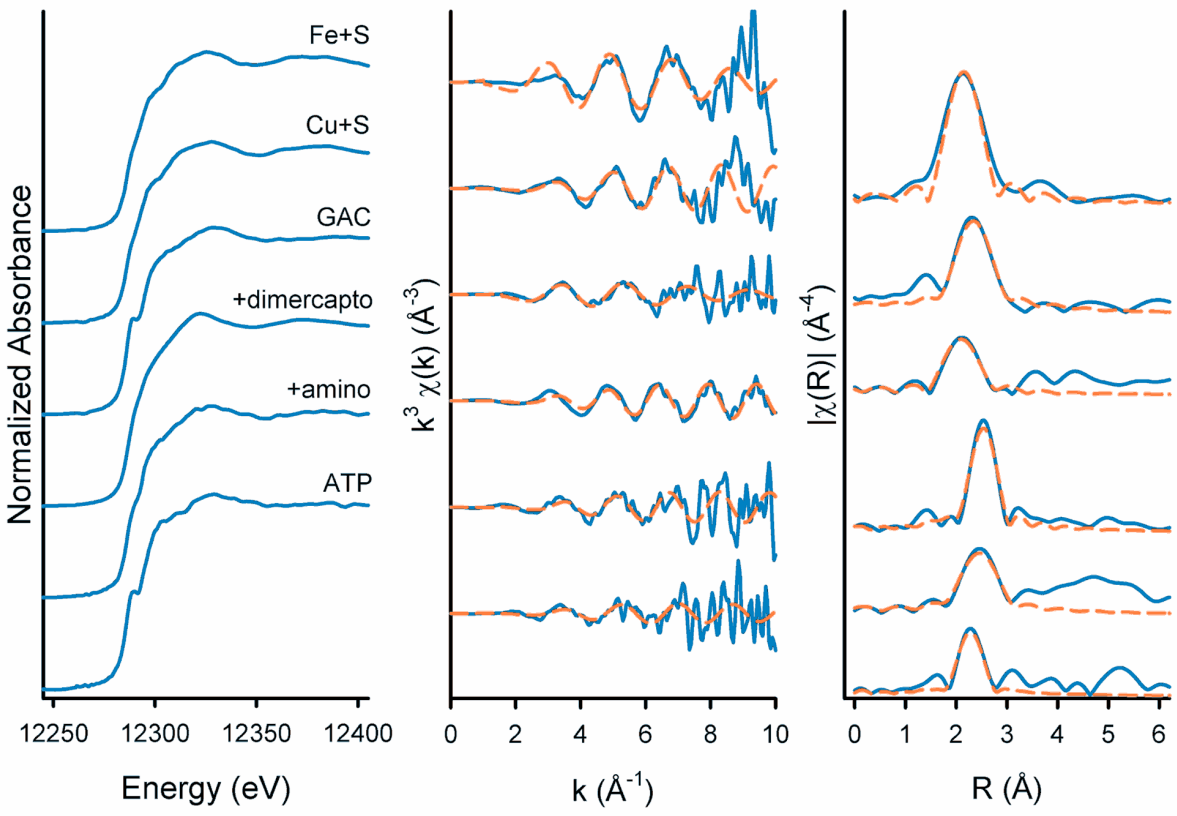

FIGURE 4.5. Normalized XANES and EXAFS spectra for the attapulgite and activated carbon amended treatment experiments. Fitting data (dashed, orange line) are compared to measured spectra (solid, blue line). Fourier transform data are corrected for phase shift.

Chapter 5:

Isotope Fractionation during Sulfate Reduction in Permeable Reactive Barriers: Reactive Transport Modeling

5.1 Executive Summary

Uniquely delineating the sequence of reaction processes in subsurface remediation systems is challenging because of the difficulties associated with retrieving and characterizing reaction products. Isotope ratio measurements provide a tool for indicating the relative significance of biogeochemical reactions and for constraining estimates of the extent and rate of these reactions. In this paper, the reactive transport model MIN3P is used to evaluate sulfur isotope fractionation in previously published column experiments designed to simulate treatment of contaminated water by microbially mediated sulfate reduction occurring within organic carbon-based and iron and carbon-based permeable reactive barriers. A mass dependent fractionation model was used to determine reaction rates for ^{32}S and ^{34}S containing compounds during reduction, precipitation, and dissolution reactions and to track isotope-dependent mass transfer during sulfate removal. Optimal isotopic fractionation factors (α) were determined from the model simulations following a least-squares fitting approach. The $\delta^{34}S$ values obtained from the MIN3P model were similar to those obtained from the Rayleigh equation, indicating that there was not a significant difference between the conceptual models. Differences between the MIN3P derived α value and the Rayleigh equation derived value were attributed to minor changes in the dissolution and precipitation rate of gypsum. Mathematical differences in the fitting models may also contribute to differences in the calculated fractionation factors. The results indicated that the prediction of $\delta^{34}S$ was fairly insensitive to differences in the fractionation factor at the concentration ranges measured in the current study. However, more significant differences would be expected at low sulfate conditions where much larger $\delta^{34}S$ values are predicted due to increases in sulfur isotope fractionation.

5.2 Introduction

Mine wastes often contain elevated levels of sulfide minerals. Oxidation of these minerals can lead to the release of acidic drainage containing high concentrations of dissolved metals and sulfate into the surrounding groundwater. A potential treatment approach is to place a permeable reactive barrier (PRB) in the subsurface ahead of the plume of contaminated water. Materials within the PRB react with contaminants in the groundwater to form less toxic, stable by-products. One treatment alternative is to promote the growth of sulfate reducing bacteria (SRB), and sulfate reduction, through the addition of organic carbon as an electron donor (Blowes et al., 2000; Benner et al., 2002):

(*5.1*) $$2CH_2O_{(s)} + SO^{2-}_{4(aq)} \rightarrow 2CO^{-}_{3(aq)} + HS^{-}_{(aq)} + 3H^{+}_{(aq)}$$

The sulfide produced through Reaction (5.1) can react with dissolved metals to form insoluble metal sulfides that will precipitate within the barrier:

(*5.2*) $$Me^{2+}_{(aq)} + HS^{-}_{(aq)} \rightarrow MeS_{(s)} + H^{+}_{(aq)}$$

Some sulfate reducing bacteria can also utilize molecular hydrogen as an electron donor. The addition of zero valent iron to a PRB system can produce hydrogen through the reduction of water, which is then utilized by SRB to reduce sulfate and produce HS^- for metal removal (Lindsay et al., 2008):

(*5.3*) $$Fe^{0}_{(s)} + 2H_2O_{(l)} \rightarrow Fe^{2+}_{(aq)} + H_{2(g)} + 2OH^{-}_{(aq)}$$

(*5.4*) $$SO_{4(aq)}^{2-} + 4H_{2(g)} + H_{(aq)}^{+} \rightarrow HS_{(aq)}^{-} + 4H_2O_{(l)}$$

Mass dependent fractionation of sulfur isotopes will occur during microbially mediated sulfate reduction, resulting in sulfide that is depleted in ^{34}S and residual aqueous sulfate that is enriched in ^{34}S (Canfield, 2001). A conceptual model of the sulfur isotope system within SRB is presented by Brunner and Bernasconi (2005), after a revision of the bacterial sulfur isotope fractionation model developed by Rees (1973):

(*5.5*) $$SO_{4(out)}^{2-} \xrightarrow{3‰} \left(SO_{4(in)}^{2-} \xrightarrow{0‰} APS \xrightarrow{-25‰} SO_3^{2-} \underset{-5‰}{\overset{-53‰}{\rightleftharpoons}} H_2S \right) \xrightarrow{0‰} H_2S$$

where $SO_4^{2-}{}_{(out)}$ to $SO_4^{2-}{}_{(in)}$ represents the transfer of sulfate across the cell walls (denoted by brackets). The internal sulfate is then converted to adenosine-5'-phosphosulfate (APS) reductase, which undergoes reduction to sulfite and H_2S. The theoretical maximum of sulfur isotope fractionation that could occur during SRB activity is equal to the sum of all isotope shifts during each step in Reaction 5.5, leading to large depletions of ^{34}S in the aqueous hydrogen sulfide and enrichments of ^{34}S in the residual sulfate pool. In a closed system, SRB activity decreases due to decreasing SO_4 concentrations, the total fractionation occurring at each step will diminish until the only active transfer of sulfate is $SO_4^{2-}{}_{(out)}$ to $SO_4^{2-}{}_{(in)}$, which results in a theoretical minimum of fractionation.

Assuming that sulfate will be converted to sulfide via the above mechanism with no other sources or sinks of sulfate or sulfide, the resulting isotopic fractionation in the shrinking sulfate pool can be described using a Rayleigh fractionation model:

(*5.6*)
$$\left(\frac{\delta^{34}S + 1000}{\delta^{34}S_0 + 1000}\right) = f^{(\alpha_k - 1)}$$

where $\delta^{34}S$ and $\delta^{34}S_0$ are the measured isotope ratios in aqueous sulfate relative to a reference standard at times t and t=0, respectively, f is the fraction remaining of the initial sulfate at time t (i.e., $[SO_4]_t$ / $[SO_4]_{t=0}$), and α_k is the kinetic fractionation factor.

The application of the Rayleigh fractionation model to groundwater treatment systems must also account for the effects of dispersion, sorption, and secondary reactions such as mineral precipitation or dissolution that may affect the calculation of the kinetic fractionation factor (Van Breukelen et al., 2004; 2007; 2008). For example, the metal sulfides formed through Reaction (5.2) derive their sulfur isotope signature from the ^{34}S depleted hydrogen sulfide produced from Reactions (5.1) or (5.4). Reoxidation of metal sulfides will produce aqueous sulfate with the same isotopic signature of the parent sulfide, thus replenishing the reaction pool with sulfate enriched in ^{32}S (Knöller et al., 2008; Knöller et al., 2010). Oxidation of aqueous sulfide will also result in a small fractionation (Balci et al., 2007). Aqueous sulfate can also be removed from the initial reaction pool through sulfate mineral precipitation (e.g., as anhydrite or gypsum). Gypsum precipitation may induce a small fractionation in measured $\delta^{34}S$ values (< 2 ‰ at 25 °C; Thode and Monster, 1965) while at the same time reducing the amount of sulfate available for reduction, thus affecting the measurement of the 'f' term in Reaction (5.6).

A potential approach to describing changes in sulfur isotope ratios in aquifers is to model isotope fractionation using a reactive transport model, where the above geochemical changes are accounted for within the sulfur cycling model. Van Breukelen et al. (2004) used

the 1D transport model PHREEQC to model carbon fractionation in a landfill leachate plume by adding ^{12}C and ^{13}C containing compounds as separate species in the model database. The individual oxidation rates related to oxidative degradation of the compounds studied were determined from the overall oxidation rate (fitted to observed data) and the kinetic fractionation factor, α_k, as determined from observations by Grossman et al. (2002). This work was later extended to model carbon fractionation during chlorinated ethene degradation (Van Breukelen et al., 2005).

In this paper, we employ a similar approach to the carbon fractionation model developed by van Breukelen et al. (2004), implemented using the reactive transport model MIN3P (Mayer et al., 2002) to model sulfur fractionation occurring within column experiments performed previously (Waybrant et al., 2002; Guo and Blowes, 2009). The purpose of this study is to investigate the potential controls on measured sulfur isotope ratios in a complex geochemical environment.

5.3 Description of Previously Performed Column Experiments

The datasets used in the current modeling study were obtained from previously performed laboratory experiments. Waybrant et al. (2002) conducted column studies to simulate the treatment of acid mine drainage using an organic carbon PRB. The study investigated the rates of sulfate reduction and metal removal treatment using simulated acid mine drainage water and different organic carbon mixtures to promote SRB activity. Two column experiments were performed in 40 cm long columns with a 5 cm inner diameter. The columns consisted of a 5 cm non-reactive bottom layer (at the influent end), a 33.5 cm middle reactive layer containing different organic carbon mixtures for the two columns, and a 1.5 cm non-reactive top layer at

the effluent end. The initial input solution (feed 0) contained only elevated levels of sulfate, whereas the other eight feed solutions contained varying levels of sulfate and dissolved metals. Samples for total sulfate and H_2S analyses were collected at regular intervals from the column influent and effluent. As the experiment was not originally designed to investigate isotope fractionation, the isotope dataset is limited. Isotope measurements were available for the column effluent from feeds 2, 3, 4, and 7. For each of these feeds, between 2 to 4 individual effluent samples were combined to provide a sufficient sample volume for $\delta^{34}S$ measurements. In a similar experiment, Guo and Blowes (2009) assessed the differences in sulfate reduction rates in a granular-iron bearing carbon (FeOC) column. This column experiment was performed in a 41 cm long column with a 7.6 cm inner diameter. The column contained 20 vol. % leaf mulch and 10 vol. % granular iron. The input solution consisted of simulated groundwater, with a composition similar to a groundwater sample collected from monitoring well MMW5 at the Getchell gold mine, Nevada (Tempel et al., 2000). Samples for total aqueous sulfate were collected at the influent, at sampling ports along the length of the column, and at the column effluent. The experiment was conducted over a period of 17 months. Total aqueous sulfate and aqueous $\delta^{34}S_{SO4}$ samples were also collected along the column profile between 372 and 432 days.

5.4 Conceptual Isotope Model

The column experiments conducted by Waybrant et al. (2002) were previously simulated by Amos et al. (2004) using the reactive transport model MIN3P without considering isotope fractionation. The conceptual model considered the microbially-mediated reduction of sulfate by organic carbon oxidation as per Reaction (5.1), mineral dissolution/precipitation reactions,

and aqueous complexation and hydrolysis reactions. The microbially-mediated sulfate reduction reaction was modeled through use of a Monod-type rate expression and was assumed to be kinetically-controlled and irreversible. Additional sources and sinks of sulfur included mackinwite [FeS], millerite [NiS], sphalerite [(Zn,Fe)S], and gypsum [$CaSO_4 \cdot 2H_2O$]. Iron was also assumed to be attenuated through the formation of siderite [$FeCO_3$], which may form with increases in dissolved carbonate. Mineral dissolution and precipitation was assumed to be kinetically controlled and reversible. The kinetic rate of sulfate reduction was assumed to be constant throughout the simulations and was calibrated by matching the modeled sulfate concentrations to the observed data.

To model sulfur isotope fractionation in the laboratory experiments, all instances of sulfur species in the MIN3P database (including all aqueous species and sulfide minerals) were modified to include separate entries for both heavy (^{34}S) and light (^{32}S) sulfur components. Reaction (5.1) was redefined as separate kinetically controlled irreversible reactions to model the rates of sulfate reduction occurring in the two organic carbon columns conducted by Waybrant et al. (2002):

(*5.7*) $$CH_2O + 0.5\,^{32}SO_4^{2-} \rightarrow CO_3^{2-} + 0.5H\,^{32}S^- + 1.5H^+$$

(*5.8*) $$CH_2O + 0.5\,^{34}SO_4^{2-} \rightarrow CO_3^{2-} + 0.5H\,^{34}S^- + 1.5H^+$$

To model the hydrogen-utilizing sulfate reduction occurring in the iron-bearing carbon column described by Guo and Blowes (2009), Reactions (5.3) and (5.4) were combined and redefined in terms of both heavy and light sulfur:

(*5.9*) $$Fe^0 + 0.25\,{}^{32}SO_4^{2-} + 2.25H^+ \rightarrow Fe^{2+} + 0.25H\,{}^{32}S^- + H_2O$$

(*5.10*) $$Fe^0 + 0.25\,{}^{34}SO_4^{2-} + 2.25H^+ \rightarrow Fe^{2+} + 0.25H\,{}^{34}S^- + H_2O$$

Input concentrations of $^{32}SO_4$ and $^{34}SO_4$ were calculated from measured $\delta^{34}S$ and total SO_4 measurements as follows:

(*5.11*) $$R_{sam} = \left(\frac{{}^{34}SO_4}{{}^{32}SO_4}\right)_{sam} = \left[\left(\frac{\delta^{34}S_{SO_4}}{1000}\right) + 1\right] * R_{std}$$

(*5.12*) $$[{}^{34}SO_4] = \frac{R_{sam} * SO_{4(tot)}}{R_{sam} + 1}$$

(*5.13*) $$[{}^{32}SO_4] = [SO_4]_{tot} - [{}^{34}SO_4]$$

where R_{sam} is the sulfur isotope ratio of the sample, R_{std} is the accepted sulfur isotope ratio of the standard Cañon Diablo troilite (CDT) reference material, and $\delta^{34}S_{SO4}$ is the measured isotope shift in aqueous sulfate relative to CDT. A R_{std} value of 0.045005 was used to facilitate comparison to the previously obtained $\delta^{34}S_{SO4}$ values. Equation (5.13) assumes that the total aqueous sulfate concentration is equal to the sum of $^{32}SO_{4(aq)}$ and $^{34}SO_{4(aq)}$. Although there are four stable isotopes of sulfur, the sum of the ^{34}S and ^{32}S masses accounts for over 99% of the

natural abundance of sulfur and thus gives a good estimation to the total aqueous concentration.

The mass-dependent rate constants ^{34}k and ^{32}k are a function of the kinetic isotope fractionation factor, α_k, and the isotope ratio of the substrate, $^{34}R_s$. The isotope ratio of the instantaneously derived product, $^{34}R_p$, is given by:

(*5.14*)
$$^{34}R_P = \frac{^{34}k_p}{^{32}k_p} = \frac{-^{34}k_s}{-^{32}k_s} = \alpha_k \, ^{34}R_S$$

where the subscripts p and s refer to the reaction products and substrate, respectively. Given that the sum of ^{34}k and ^{32}k is equal to k_{eff}, the overall reaction rate constant, the following relations are derived for the rate of reactions 5.7-5.10:

(*5.15*)
$$^{34}k = \frac{k_{eff}}{1+\left(\frac{1}{\alpha_k \, ^{34}R_S}\right)}$$

(*5.16*)
$$^{32}k = \frac{k_{eff}}{1+\left(\alpha_k \, ^{34}R_S\right)}$$

Because the kinetic fractionation factor follows a power series, both the Rayleigh equation and the current version of the model presented here will predict large $\delta^{34}S_{SO4}$ values when the fraction of SO_4 remaining approaches zero. This conflicts with the model presented by Brunner and Bernasconi (2005), which has been confirmed experimentally by other researchers. Harrison and Thode (1958) showed no change in the extent of isotope fractionation at SO_4 concentrations greater than ~1 mmol L^{-1}. The apparent fractionation factor

decreased when concentrations fell below this level, and at very low levels (< 10 μmol L^{-1}) the fractionation factor inverted as $^{34}SO_4$ reacted faster than $^{32}SO_4$ by 3‰. Ingvorsen et al. (1984) studied the kinetics of sulfate uptake by *Desulfobacter postgatei* and found that sulfate uptake by these bacteria ceased at concentrations lower than 20 μmol L^{-1}. Canfield (2001) reported similar results at SO_4 concentrations down to 2 mmol L^{-1}, and noted that no attempt had yet been made in the literature to quantify the simultaneous influence of low SO_4 concentrations on both sulfate reduction rates and isotope fractionation, either in laboratory cultures or in natural populations of SRB. These results suggest that the conceptual isotope model presented in the current study is likely not valid at very low SO_4 concentrations. However, a more sophisticated approach was not warranted as no isotope data were available during periods when SO_4 concentrations approached these levels. For the cases where isotope data were available, the SO_4 concentrations were sufficiently high to assume the complete conversion of SO_4 to H_2S as described by Reaction (5.5).

5.5 Model Parameters

All parameters used in the Waybrant et al. (2002) column simulations (with the exception of the kinetic fractionation factors) were consistent with the parameters used by Amos et al. (2004). Columns were modeled as a 40 cm long 1D solution domain discretized into 1 cm long control volumes. The initial volume fraction of organic carbon was arbitrarily set to 0.1 to account for an excess of available carbon for sulfate reduction. The volume fraction of calcite was adjusted to fit the modeled data. The other components of the columns (including the silica sand layers) were considered to be non-reactive and were not included in the model. The column temperature was assumed to be 25°C. Eighteen components were used to describe the

geochemical system: Ar(aq), Br, Ca, CO_3, Cl, Fe(II), H^+, K, Mg, Mn, Na, Ni, O_2(aq), and Zn, as well as the four mass-dependent sulfur species: $^{32}SO_4$, $^{34}SO_4$, $H_2{}^{32}S$, and $H_2{}^{34}S$. A total of 92 aqueous species and 14 mineral species were included. Minerals solubilities were determined based on the WATEQ4F (Ball and Nordstrom, 1991) and MINTEQA2 (Allison et al., 1991) databases.

The Guo and Blowes column was simulated in a similar manner with the following exceptions. The column was modeled as a 41 cm long 1D solution domain discretized into 1 cm long control volumes. The initial value of organic carbon was adjusted to model SRB inactivity due to a loss of available carbon (see Results and Discussion). Ten components were used to describe the geochemical system: Ca, Na, K, Mg, Fe, CO_3, H_3AsO_4, $Sb(OH)_3$, H^+, and $H_{2(aq)}$, in addition to $^{32}SO_4$, $^{34}SO_4$, $H_2{}^{32}S$, and $H_2{}^{34}S$. A total of 44 aqueous species and 14 mineral species were included.

Mineral dissolution and precipitation reactions for both simulations were modeled as kinetically-controlled reversible reactions and were calibrated to, and constrained by, measured geochemical data. Important geochemical reactions that were considered include calcite dissolution and siderite, gypsum, and sulfide mineral precipitation. The mass-dependent sulfate reduction reactions were initially modeled by Amos et al. (2004) with a simplified Monod-type rate expression. In this study, the same approach was extended to account for the reaction rates of both heavy and light sulfur isotopes:

$$R_{CH_2O-{}^{32}SO_4} = -{}^{32}k_{SO_4}\left[\frac{[SO_4]}{K_s + [SO_4]}\right] \quad (5.17)$$

(*5.18*)
$$R_{CH_2O-^{34}SO_4} = -^{34}k_{SO_4}\left[\frac{[SO_4]}{K_s + [SO_4]}\right]$$

where $R(CH_2O\text{-}^{32}SO_4)$ and $R(CH_2O\text{-}^{34}SO_4)$ are the rates of overall reaction progress, K_s is the half-saturation constant, and $[SO_4]$ is the total sulfate concentration. This formulation was used for both columns types (i.e., OC and Fe-bearing OC). The substrate, either OC or H_2, was considered to always be in excess in both simulations and thus does not appear in the rate expressions. Half-saturation constants reported in the literature range from 34 μmol L^{-1} in oligohaline sediments (Roden and Tuttle, 1993) to 1.62 mmol L^{-1} in marine sediments (Boudreau and Westrich, 1984). Experiments have also shown that the rate of sulfate reduction is independent of dissolved SO_4 at concentrations >1-3 mmol L^{-1} (Boudreau and Westrich, 1984; Roychoudhury et al., 1998). In the column experiments described by Waybrant et al. (2002), effluent SO_4 concentrations only approach zero during the initial stage of the experiment (feed 1) and thus the modeled SO_4 results are not expected to be sensitive to changes in K_s during the period when sulfur isotope measurements were made. Simulations in this study were performed at K_s values of 1.62 mmol L^{-1} to be consistent with the results reported by Amos et al. (2004).

5.6 Results and Discussion

5.6.1 Determination of α_k From Rayleigh Equation

Average kinetic fractionation factors (α_k) based on the Rayleigh equation and measured values of SO_4 and $\delta^{34}S$ were calculated for the two Waybrant et al. (2002) columns (referred to as "Waybrant 1" and "Waybrant 2" for the remainder of the paper) and the iron-bearing Guo and Blowes (2009) column ("Guo 1"). Alpha values were calculated from Eq. 5.6 by fitting a

power law regression of the form $y = a*x^b$, where the 'a' term was set to 1 to force the regression curve through (1,1) and the 'b' term is equal to (α-1). Evaluation of the data produced α_k values of 0.9616 Waybrant 1 and 0.9579 for Waybrant 2, and 0.9784 for Guo 1.

5.6.2 Determination of α_k From Model Sensitivity Analysis

Model simulations were performed at a range in α_k values to determine the sensitivity of the model to changes in the fractionation factor. The effective overall rate constants for the Waybrant 1 (6.9×10^{-9} mol L^{-1} bulk s^{-1}) and Waybrant 2 (1.5×10^{-8} mol L^{-1} bulk s^{-1}) were previously optimized to model observed SO_4 concentrations (Amos et al., 2004). Plots of simulated $\delta^{34}S$ vs. time compared to the observed effluent $\delta^{34}S$ values are shown in Figure 5.1. During periods of relatively low SO_4 concentrations at the effluent (e.g., 345 to 396 days), the predicted $\delta^{34}S$ values were more sensitive to changes in the fractionation factor compared to periods of higher SO_4 concentrations (e.g., from 135 to 255 days). To determine the optimal α_κ values, residual values were calculated between modeled $\delta^{34}S$ and observed $\delta^{34}S$ for a range of α_κ values. The optimal α_κ values for the two columns described by Waybrant et al. (2002) were determined by finding the minimum of the residual sum of squares (RSS) for the four feeds where isotope data were available. This method resulted in α_k values of 0.9602 for Waybrant 1 and 0.9631 for Waybrant 2. A similar procedure was applied to the Guo 1 column (Figure 5.2). Because the OC fraction in the Guo 1 column lost reactivity after 135 days and the available isotope data was obtained after 360 days of flow, the fractionation due to OC was not considered in the simulations. Therefore, the sensitivity analysis was performed using α_{Fe0} only and resulted in an optimal fractionation factor of 0.9735.

5.6.3 Sulfate Reduction and Isotope Fractionation

Breakthrough curves of modeled SO_4 and $\delta^{34}S_{SO4}$ for the two Waybrant columns using MIN3P were compared to measured effluent values (Figure 5.3). Periods of decreasing SO_4 correspond to periods of increasing $\delta^{34}S_{SO4}$ for both columns. The column profile data from the iron:carbon treatment experiments described by Guo and Blowes (2009) shows a similar trend, with a gradual decrease in SO_4 corresponding to an increase in $\delta^{34}S_{SO4}$ (Figure 5.4). Isotope data during periods of very low SO_4 concentrations (0-125 d) for the Waybrant 1 and 2 columns (Figure 5.3) were not plotted because very large and likely incorrect $\delta^{34}S_{SO4}$ values were predicted by the model and no isotope data were available to effectively apply and evaluate a more sophisticated conceptual model. The smoothness of the modeled curves compared to the step-wise pattern of the influent measurements was attributed to dispersion effects.

The significance of the deviation between the Rayleigh equation derived α_k and MIN3P derived α_k values for predicting either the isotope ratio or the fraction of substrate remaining was determined by comparing predicted $\delta^{34}S_{SO4}$ values with each model (Table 5.1). Optimal $\delta^{34}S_{SO4}$ values for the Rayleigh equation were calculated by substituting α_k into Equation 5.6 and fixing the f value from the observed data. Residual values were determined as the difference between the newly calculated $\delta^{34}S_{SO4}$ values and the measured values. The residual values determined in this manner for the three column simulations were similar to the residual values obtained from the MIN3P derived $\delta^{34}S_{SO4}$ values, indicating that either model resulted in similar error in the residuals of the calculated isotope values, though this difference is dependent on the progress of the modeled reaction. Due to the exponential relationship between the fraction of SO_4 remaining and the $\delta^{34}S$ value in kinetically controlled isotope

fractionation (e.g., Equation 5.6), a large change in f when f is close to 1 (i.e., near the reaction start) results in a small increase in $\delta^{34}S_{SO4}$. As the reaction proceeds and f approaches 0, small changes in f will result in much higher $\delta^{34}S_{SO4}$ values. The relative differences in the calculated α_k values are thus less important in the region close to the initial conditions. The importance of these differences for predicting the residual amount of substrate can be approximated by substituting the α_k values into Equation 5.6 and calculating f at fixed $\delta^{34}S_{SO4}$ values. For the Waybrant 1 simulations, the difference between the two α_k values is small and thus the difference in calculated f values is minor even at relatively large $\delta^{34}S_{SO4}$ values; for example, at $\delta^{34}S_{0\text{-}SO4}$ = 0 ‰ and $\delta^{34}S_{SO4}$ = 25 ‰, the f calculated from the Rayleigh derived α_k, is 0.526 compared to 0.538 for the MIN3P derived factor. These differences are more pronounced for the Guo column simulations because the larger α_k, values result in predicted f values that are closer to 0 for the same $\delta^{34}S_{SO4}$ value. Using the above values for $\delta^{34}S_{0\text{-}SO4}$ and $\delta^{34}S_{SO4}$ results in f values of 0.390 from the Rayleigh derived α_k, and 0.464 from the MIN3P derived value. However, these differences are within the acceptable range of error given the objectives of the study, which was to establish the utility of this modeling approach..

Deviations between the conceptual isotope models and the experimental conditions potentially affected the accuracy of the predicted fractionation factors. For both models, the initial values of $\delta^{34}S_{SO4}$ and SO_4 were assumed to be constant but variations in the composition of the input solution may have induced a change in the observed $\delta^{34}S_{SO4}$ values that were not accounted for in the conceptual models. Conceptual differences between the two models may also account for some of the deviation between observed and predicted $\delta^{34}S_{SO4}$. The Rayleigh equation assumes that no other sources or sinks of sulfate or sulfide are present. However, simulations of the Waybrant columns predicted minor changes in the saturation index and

dissolution/precipitation rates for gypsum (Amos et al., 2004). The precipitation of gypsum would reduce the amount of sulfate available for reduction to sulfide via Reactions 5.1 and 5.4, whereas dissolution would add an additional source of sulfate to the reaction pool.

Mathematical differences between the model fitting routines could also affect the accuracy of the calculated fractionation factors. For the Rayleigh model, Equation 5.6 was used to calculate α_k from the available isotope data, which consisted of 4 data points for the two Waybrant columns and 8 data points for the Guo column. The MIN3P model was first calibrated to all of the available sulfate effluent data before refining α_k to fit the isotope data through a least squares regression analysis. The Rayleigh equation was not as sensitive to changes in data as the least squares fit was. For example, if the two largest $\delta^{34}S_{SO4}$ values from Guo 1 (Fig. 5.4) are removed from the Rayleigh model, the newly calculated α_k, value is 0.9789, compared to 0.9784 when all data are included. If these data points are removed from the least squares analysis from the MIN3P model, α_k, changes to 0.9779 compared to the initial value of 0.9735 when all data points are incorporated in the analysis.

5.7 Conclusions

A conceptual sulfur isotope fractionation model based on a mass-dependent rate constant approach was successfully integrated into the reactive transport model MIN3P and used to track isotope fractionation occurring within previously performed column experiments. The model simulations show that the predicted $\delta^{34}S_{SO4}$ values in the residual aqueous SO_4 are more sensitive to changes in the kinetic fractionation factor (α_k), half-saturation constant (K_s), and the effective rate constant (k_{eff}) when SO_4 concentrations approach low levels. When a high rate constant is used, the predicted $\delta^{34}S_{SO4}$ values exceed the fractionation limit predicted by

theoretical studies. This apparent limit on sulfur fractionation occurs because sulfate reducing bacteria become less selective towards utilizing ^{32}S over ^{34}S when SO_4 concentrations approach very low levels. Similarly high $\delta^{34}S_{SO4}$ values would also be predicted by the Rayleigh equation, due to the power law relationship between the observed $^{34}S/^{32}S$ ratio and the fraction of SO_4 remaining as f approaches 0. More detailed research is required to better define the sulfur isotope system occurring during sulfate reduction at low SO_4 concentrations, after which a future version of the reactive transport model could potentially be modified to account for the change in fractionation at low sulfate levels.

TABLE 5.1
Comparison of Rayleigh equation and MIN3P derived fractionation factors

Waybrant			Rayleigh equation					MIN3P simulations			
column 1	$\delta^{34}S_{in}$ (‰ CDT)	$\delta^{34}S_{eff}$ (‰ CDT)	A	f	$\delta^{34}S$ (‰ CDT)	r	Σr^2	α	$\delta^{34}S$ (‰ CDT)	r	Σr^2
feed 2 (163.3 d)	1.7	13.8	0.9616	0.71	15.1	1.3	15.31	0.9602	8.9	-4.9	26.70
feed 3 (198.6 d)	2.0	10.2		0.82	9.5	-0.7			9.9	-0.3	
feed 4 (244.1 d)	1.7	9.0		0.77	11.8	2.8			9.2	0.2	
feed 7 (384.1 d)	4.8	25.1		0.63	22.8	-2.3			26.7	1.6	
column 2											
feed 2 (163.3 d)	1.7	16.0	0.9579	0.69	17.7	1.7	30.18	0.9631	15.7	-0.3	23.95
feed 3 (198.6 d)	2.0	20.0		0.63	21.8	1.8			17.6	-2.4	
feed 4 (244.1 d)	1.7	20.4		0.59	24.2	3.8			16.5	-3.9	
feed 7 (384.1 d)	4.8	55.1		0.34	52.0	-3.1			56.8	1.7	
Guo and Blowes	$\delta^{34}S_{pro}$										
influent (0.0 cm)	4.4		0.9784	1.00	4.4	0.0	15.08	0.9735	4.7	0.3	24.82
P2 (5.5 cm)	6.4			0.89	6.9	0.5			6.4	0.0	
P4 (10.5 cm)	8.2			0.84	8.2	-0.1			8.2	0.0	
P7 (15.5 cm)	9.3			0.81	9.0	-0.4			10.1	0.8	
P8 (20.5 cm)	10.7			0.78	9.8	-0.9			12.1	1.5	
P10 (25.5 cm)	13.1			0.61	15.2	2.1			14.2	1.1	
P12 (30.5 cm)	18.3			0.50	19.5	1.2			16.3	-2.0	
P14 (35.5 cm)	20.3			0.54	17.8	-2.5			18.2	-2.2	
eff. (41.0 cm)	14.8			0.66	13.4	-1.4			18.3	3.5	

N.B. $\delta^{34}S_{in}$ = column influent $^{34}S/^{32}S$ isotope values in aqueous SO_4, $\delta^{34}S_{eff}$ = column effluent $^{34}S/^{32}S$ isotope values in aqueous SO_4 from Waybrant et al. (2002); $\delta^{34}S_{pro}$ = column profile $^{34}S/^{32}S$ isotope values in aqueous SO_4, including effluent (eff.) from Guo and Blowes (2009); α = fractionation factor; f = fraction SO_4 remaining (i.e., $[SO_4]/[SO_4]_0$); r = residual value (i.e., $\delta^{34}S_{modeled} - \delta^{34}S_{observed}$); Σr^2 = residual sum of squares (i.e., $(r_1^2 + r_2^2 + ... r_x^2)$)

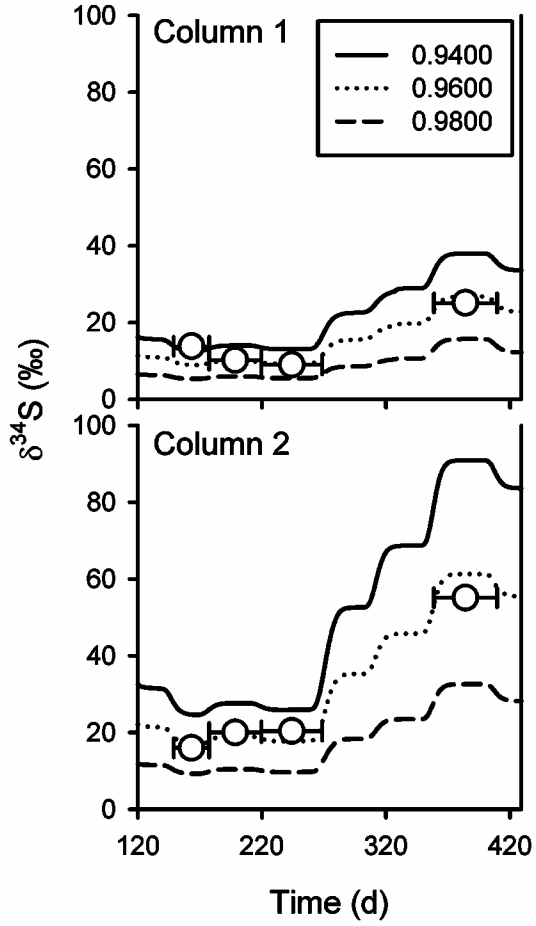

FIGURE 5.1 Plots of simulated effluent $\delta^{34}S_{SO4}$ versus. time at different α values for Waybrant 1 and 2, compared to measured column effluent (○). Horizontal error bars represent the extent of the effluent for feeds 2, 3, 4, and 7. Modeled effluent data prior to 120 days have been removed since no experimental data was available during this time.

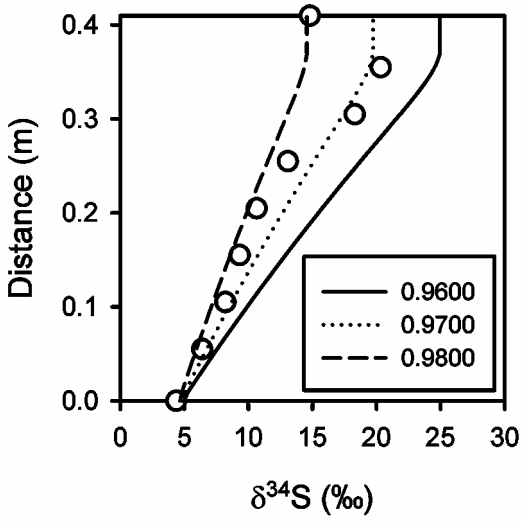

FIGURE 5.2 Plots of simulated effluent $\delta^{34}S_{SO4}$ versus distance at different α values for Guo column 1, compared to measured column profile data (○).

.

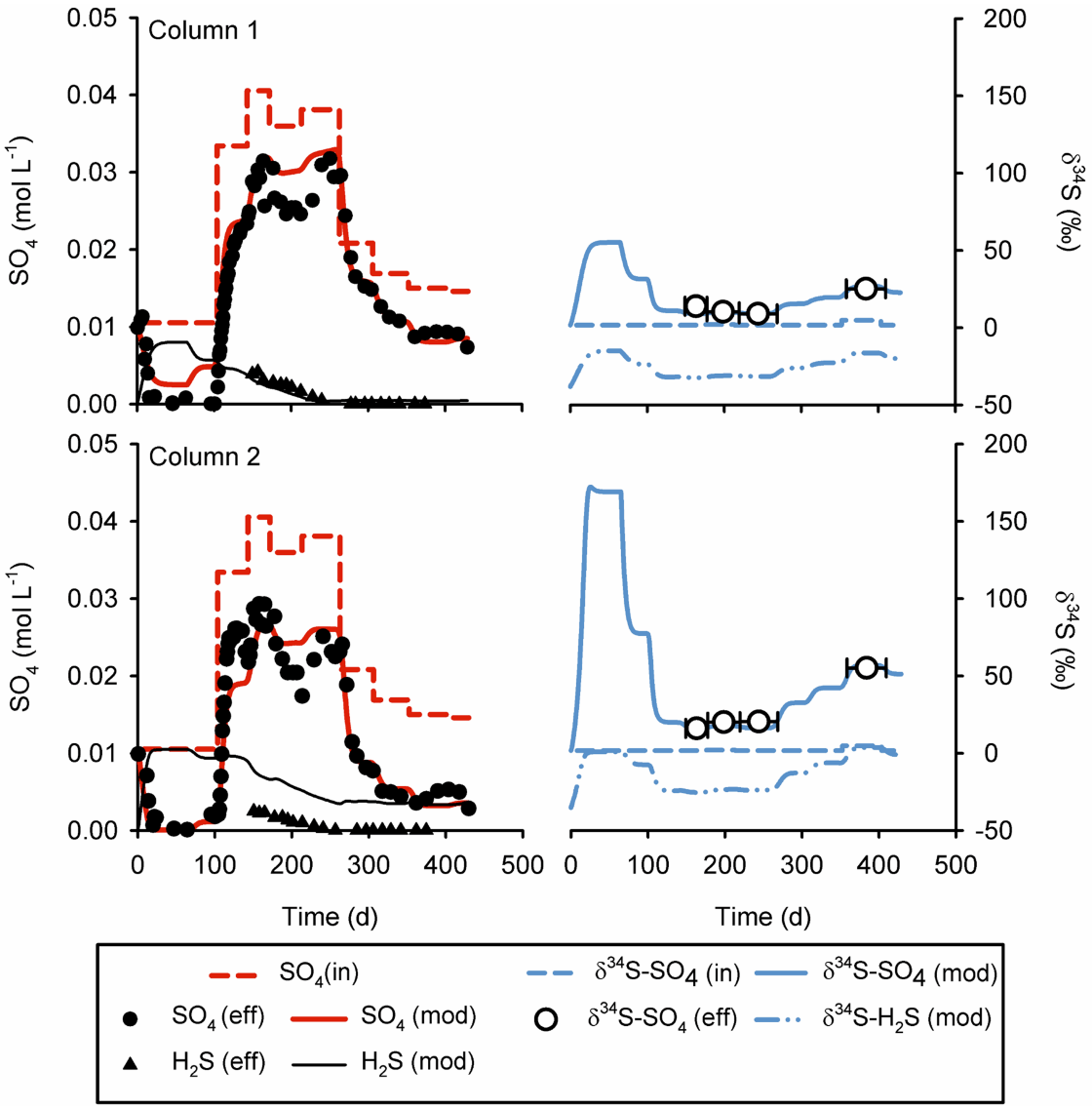

FIGURE 5.3 Comparison of modeled SO_4 and $\delta^{34}S$ data for Waybrant columns 1 and 2. Shown are: influent SO_4 (red dashed line) and $\delta^{34}S$ (blue dashed line); effluent SO_4 (●), H_2S (▲) and $\delta^{34}S$ (○); modeled SO_4 (red solid line), H_2S (black solid line), $\delta^{34}S$-SO_4 (blue solid line), and $\delta^{34}S$-H_2S (blue solid-dotted line). Modeled SO_4 data were obtained from Amos et al. (2004).

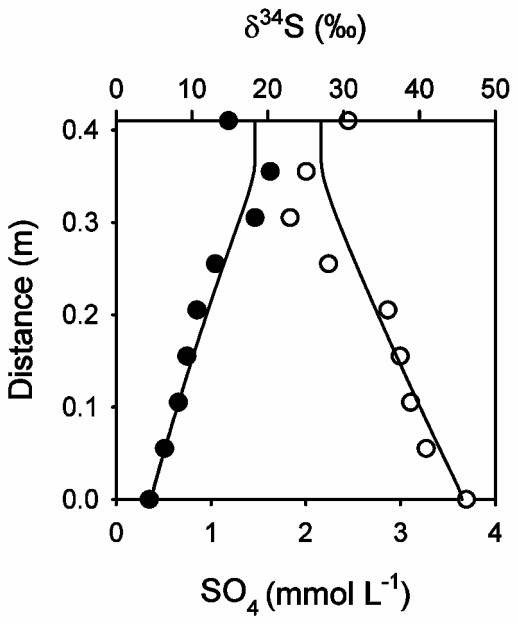

FIGURE 5.4 Comparison of column profile measurements and model predictions in the iron:carbon mixed treatment column (● - measured SO_4, ○ - measured $\delta^{34}S_{SO4}$, solid line – modeled data) described by Guo and Blowes (2009).

Chapter 6:

Conclusions

6.1 Summary of Findings

A variety of different analytical methods were employed to assist in the interpretation of sediment characterization and water treatment studies. In Chapter 3, several different analytical techniques were used to characterize a lake sediment contaminated with Hg and to predict the potential for Hg release. Mercury concentrations in 10 separate sediment cores samples ranged from 20 to 340 μg g^{-1}, and the highest Hg concentrations were found closest to the point of discharge. Total sediment digestion showed a statistically significant positive correlation between Hg and other chalcophilic elements, such as Cu, Pb, and Se. Sequential extraction analyses showed that the majority of Hg was extractable as the F4 or F5 fraction in 9 of the 10 sediment core locations. The possible presence of HgS, CuS, and HgSe was confirmed through elemental XRF mapping and XANES analysis. These results showed that a majority of the Hg present in the sediment is likely in a chemically stable form. However, resuspension tests performed in oxic and anoxic conditions indicated that oxidative release of Hg occurs, possibly due to oxidative degradation of organic carbon or oxidative dissolution of sulfides. Therefore, implementation of strategies to minimize either mixing of the sediment with oxic surface water in the lake during dredging or minimizing release of contaminated water resulting from dredging is recommended.

X-ray absorption spectroscopy techniques were also used to characterize the solid phase reactions products formed during treatment of aqueous Se (Chapter 2) and aqueous Hg (Chapter 4), and this information was used to add additional information to the aqueous geochemistry results. Micro-XANES analysis of Connelly Fe^0 thin sections showed that removal of Se from an artificial groundwater was due to the reduction of Se(VI) to an insoluble reduced phase, either Se(0) or Se(-II), with Se(IV) occurring as an intermediate reaction product. While the use of organic carbon did not appear to be effective for promoting biologically mediated reduction based on the aqueous geochemistry results, X-ray absorption spectra identified Se(VI) with minor amounts of Se(IV) and Se(0) or Se(-II), indicating that some reduction had occurred. The geochemistry results showed that the addition of granular Fe^0 to organic carbon improved removal of Se compared to only organic carbon, though removal was lower compared to the pure granular Fe^0 case. Analysis of both Fe^0 and carbon grains in the reaction mixture showed evidence of both Se(IV) and either Se(0) or Se(-II) on both the organic carbon material and Fe grains with no evidence of Se(VI). This indicated that the presence of Fe^0 was enhancing reduction of Se by organic carbon. This information would be difficult to obtain without the use of XAS techniques.

The importance of XAS techniques to add additional geochemical information was more apparent with the Hg treatment investigations (Chapter 4). While traditional geochemical measurements were used to track the reaction progress, XAS techniques including extended X-ray absorption fine structure (EXAFS) analysis were required to distinguish the different mechanisms of removal. For example, Weisener et al. (2005) previously used columns containing Connelly granular Fe to remove aqueous Hg from contaminated groundwater containing SO_4, and XAS techniques were used to characterize the reaction products as either

cinnabar [α-HgS] or metacinnabar [β-HgS]. In the current study, the efficacy of Connelly Fe^0 to remove aqueous Hg(II) in the absence of SO_4 was evaluated to assess the potential for Hg treatment by granular Fe^0 in SO_4-poor environments. EXAFS analysis indicated that Hg was bound to oxygen on the margins of Fe grains, likely to an Fe oxide corrosion product. The addition of aqueous Se(VI) to aqueous Hg(II) did not appear to mediate the removal of Hg as HgSe, as EXAFS analysis showed that Se was present as Se^0 on the grain margin. The influence of additional treatment materials on Hg stabilization was characterized by bulk XAS techniques: untreated attapulgite (palygorskite) clay, attapulgite clay treated with 2-amino-5-thiol-1,3,4-thiadiazole, attapulgite clay treated with 2,5-dimercapto-1,3,4-thiadiazole, granular activated carbon, elemental copper (Cu^0) mixed with elemental sulfur (S^0), and a second type of granular iron (QMP) mixed with S^0. Although the untreated attapulgite was successful in removing ~30% of the aqueous Hg, pre-treatment of the clay with thiol- and dimercato-functionalized thiadiazole compounds increased Hg removal to 69% and greater than 99%, respectively. EXAFS analysis showed an apparent increase in coordination and bond length with increasing amount of functionalized thiol groups, with Hg bound to S on the treated clays. Mercury removal was similar in the granular $Fe+S^0$ and Cu^0+S^0 mixtures, though EXAFS analysis indicated different removal mechanisms. The addition of S^0 to Cu^0 appeared to induce the formation of a cinnabar-like structure, with a modeled bond length of 2.35 Å compared to the theoretical length of 2.37 Å for cinnabar. In contrast, the addition of S^0 to granular QMP Fe^0 appeared to have no effect on Hg removal, as the EXAFS spectrum was more similar to the spectra obtained with the Connelly Fe^0 treatment with structure modeling suggesting the formation of Hg-O. Granular activated carbon also was effective at removing aqueous Hg(II), with the structure model indicating the formation of Hg-O bonds. The formation of Hg-O is

likely due to the binding of Hg(II) to oxygen complexes on the carbon surface created by the sorption of water, as observed by Li et al. (2002).

The integration of a kinetic stable isotope fractionation model to the reactive transport model MIN3P was investigated in Chapter 5. Kinetic isotope fractionation is governed by the Rayleigh equation (Equation 5.6), which does not consider other geochemical processes that may affect the measured fractionation such as dispersion, sorption, and secondary mineral precipitation or dissolution reactions. Through integration of the conceptual isotope fractionation model it is possible to account for these geochemical processes and more accurately track S isotope fractionation occurring during PRB treatment studies. Although the model becomes inaccurate at low SO_4 conditions because it does not properly account for the deactivation of SRB that occurs when SO_4 approaches very low levels, the conceptual model could potentially be modified to account for fractionation at these conditions provided that more experimental data describing the changes in $\delta^{34}S_{SO4}$ at low concentrations become available.

6.2 Scientific Contributions

The research presented in this thesis has contributed information to passive treatment studies involving Hg and Se, sediment characterization studies, and model simulation of isotope fractionation due to SO_4 reduction reactions during dynamic flow conditions. The scientific contributions include:

- Demonstrating that granular Fe is highly effective for treating elevated concentrations (e.g., 300 mg L^{-1}) of aqueous Se(VI) under anoxic conditions, and characterization of

the removal mechanism as reduction to insoluble Se^0 through synchrotron radiation-based XAS methods.

- Designing a modified sediment resuspension test to incorporate extended mixing in oxic and anoxic environments to delineate reaction mechanisms during resuspension, and demonstrating the potentially adverse effect of oxic mixing with a Hg-contaminated lake sediment, which was previously unknown at the contamination site.
- Investigating several treatment materials for treating aqueous Hg(II), and applying synchrotron radiation-based XAS methods to characterize the reaction products.
- Developing a conceptual model for predicting isotope fractionation during SO_4 reduction under dynamic transport conditions and providing a framework for modeling other stable isotope systems.

6.3 Recommendations

Granular Fe^0 was shown to be effective in promoting the reduction of relatively high concentrations of Se(VI) to insoluble Se(0) under conditions expected to occur in anoxic groundwater environments. This treatment approach has potential applications in passive treatment systems such as permeable reactive barriers, where treatment media are placed within the flow path of contaminated groundwater. Iron may also be a useful addition to organic carbon based treatment systems designed to promote Se(VI) reduction by anaerobic selenate-reducing bacteria (SeRB). Under oxic conditions, the effectiveness of granular Fe^0 is expected to be greater than under anoxic conditions due to the increased formation of iron oxides capable of either adsorbing or chemically reducing Se(VI). Irrigation-induced Se contamination is a concern in localities where soil is derived from marine sedimentary

deposits, such as the Great Plains area located between the Mississippi River and the Rocky Mountains and extending from the Prairie Provinces in Canada to the state of Texas in the United States, as well as in San Joaquin Valley, California. A granular Fe^0-based system may be more effective than a carbon-based system for treating well-oxygenated irrigation wastewater, due to the reducing conditions required to promote SeRB activity.

With regard to potential restoration strategies for the Hg contaminated lake sediment, monitored natural attenuation may be effective given the sediment sulfur concentrations and the evidence for Hg sulfide species as a sink for aqueous Hg, though additional experiments to monitor Hg concentrations in the water column would need to be performed. The resuspension tests indicated that some sample locations will likely release unwanted levels of Hg into the surrounding water during sediment disturbance events and thus mechanical dredging, which is generally poorly rated for sediment resuspension, is not recommended. Hydraulic dredges that are designed to remove sediment with minimal disturbance may be more appropriate in this case, though the water removed along with the sediment would likely contain elevated levels of aqueous Hg and Pb and thus proper treatment strategies would need to be developed to both stabilize the contaminated sediment and treat the contaminated dredging water. In situ capping may be an appropriate treatment strategy to isolate the sediment from the benthic environment and to prevent resuspension. The cap material could be amended with some of the materials tested in this work to help prevent the release of Hg to the lake water column. The addition of sulfur, either through thiol-functionalized compounds or as S^0, may help to stabilize Hg as Hg sulfide. The presence of reduced sulfur also would help to inhibit methylating bacteria, although redox conditions would need to be monitored to ensure that re-oxidation of sulfides is not occurring. Amendment with granular Fe^0 in the absence of SO_4 appears to induce the

removal of Hg through binding to Fe oxides. This may be a preferable treatment option in more oxic regions as increased oxidation may result in enhanced Hg removal due to the increased formation of Fe oxides. For anoxic conditions, amendment with sulfur may be more appropriate.

6.4 Future Work

Granular Fe^0 was an effective treatment medium for Se(VI) although it is more expensive per unit mass than the organic carbon amendments used to promote SeRB activity. A cost effective treatment medium may be a mixture of Fe^0 and organic carbon, although the field application would be dependent on the contamination source. Selenium contamination in irrigation wastewater is common in certain localities and presents a different challenge compared to the treatment of groundwater, due to the oxic nature of irrigation water. Granular Fe^0 will rapidly consume dissolved oxygen, which may be sufficient to maintain anaerobic conditions necessary for SeRB activity. The application of granular Fe^0 alone under oxic conditions may also produce differences in the removal mechanisms observed in this thesis, due to the increased formation of Fe(III) hydroxides or oxyhydroxides. Future laboratory experiments should include the long-term evaluation of granular Fe^0 mixtures under both oxic and anoxic conditions to simulate potential field applications. The evaluation of different types of granular Fe^0 should also be tested, with regard to reactivity, effect of grain size, and cost effectiveness. Smaller grain sizes would be expected to have increased reactivity due to a larger surface area. Ponder et al. (2000) observed an increase in removal rates of aqueous Cr(VI) and Pb(II) using nanoparticulate Fe^0 particles in batch experiments, compared to treatment using Fe^0 filings and powder with larger surface areas. However, in passive treatment systems that are expected to

continually treat contaminated groundwater for several decades the benefit of increased reactivity may not be as significant as treatment is also limited by the natural flow of groundwater through the system. Therefore, column experiments should also be performed to evaluate the cost effectiveness of smaller grain sizes over longer reaction times.

The addition of a dimercapto-functionalized thiadiazole compound to attapulgite clay greatly enhanced the removal of Hg compared to untreated clay. The ability of other common treatment materials to remove Hg also may be enhanced by the addition of functionalized thiadiazole compounds. A potential use is in sediment caps, where treatment media such as activated carbon or clay could be pre-treated with these compounds prior to deployment in the field. There also is potential to apply these compounds directly to contaminated areas, such as exposed river bank sediment, although the stability of the treatment in more oxic areas is not known at this time. Future research should investigate the benefits of pre-treating other types of media with these compounds, and the material should be evaluated under different geochemical conditions to determine the long-term stability under both oxic and anoxic conditions.

Tracking the isotope fractionation occurring during treatment of Se and Hg may help to further characterize the treatment mechanism, as removal by mineral precipitation is expected to result in a different fractionation than removal through sorption or ion exchange processes. Biologically mediated treatment may also induce an isotope fractionation that is distinguishable from abiotic mechanisms. This information can be incorporated into the modified MIN3P code to predict fractionation changes occurring from certain mechanisms. The current version of the code successfully modeled isotope fractionation occurring at higher SO_4 concentrations, but failed to give reasonable results at very low concentrations. This was

attributed to a failure of the conceptual model to adequately approximate changes in microbiological activity at low concentrations. Further research would be necessary to better characterize the fractionation occurring at these levels before the model can be modified; however, this characterization is limited by detection limits of the available instrumentation. At the time of writing this thesis, the Environmental Isotope Laboratory at the University of Waterloo required a minimum of 1 mg S for $\delta^{34}S$ measurements. In batch and column studies that utilize SRB activity to remove contaminants from water, total aqueous S concentrations may fall well below this level and thus make it difficult to properly interpret changes in fractionation. Future experimental designs should take the limitations of X-ray absorption and isotope ratio techniques into consideration; namely, relatively large initial masses are required that may not accurately match much lower field concentrations. For isotope ratio analyses, a combined technique of analyzing both the residual aqueous phase and the accumulating solid phase product may be required to fully characterize the isotope fractionation system.

References

Allard, B., Arsenie, I., 1996. Abiotic reduction of mercury by humic substances in aquatic system – an important process for the mercury cycle. Water Air Soil Pollut. 56, 457-464.

Allison, J.D., Brown, D.S., Novo-Gradac, K.L., 1990. MINTEQA2/PRODEFA2, A Geochemical Assessment Model for Environmental Systems, Version 3.0 User's Manual. Environmental Research Laboratory, Office of Research and Development, US EPA, Athens, GA.

Alpers, C.N., Hunerlach, M.P., Marvin-DiPasquale, M.C., Antweiler, R.C., Lasorsa, B.K., De Wild, J.F., Snyder, N.P., 2006. Geochemical data for mercury, methylmercury, and other constituents in sediments from Englebright Lake, California, 2002, U.S. Geological Survey Data Series 151, 95 p.

Alshawabkeh, A.N., Rahbar, N., Sheahan, T., 2005. A model for contaminant mass flux in capped sediment under consolidation. J. Contam. Hydrol. 78, 147-165.

Alvarez-Puebla, R.A., Aisa, C., Blasco, J., Echeverría, J.C., Mosquera, B., Garrido, J.J., 2004. Copper heterogeneous nucleation on a palygorskitic clay: an XRD, EXAFS and molecular modeling study. Appl. Clay Sci. 25, 103-110.

Amos, R.T., Mayer, K.U., Blowes, D.W., Ptacek, C.J., 2004. Reactive transport modeling of column experiments for the remediation of acid mine drainage. Environ. Sci. Technol. 38, 3131-3138.

Amyot, M., Mierle, G., Lean, D.R.S., McQueen, D.J., 1994. Sunlight-induced formation of dissolved gaseous mercury in lake waters. Environ. Sci. Technol. 28, 2366-2371.

Arbestain, M.C, Rodríguez-Lado, L., Bao, M., Macias, F., 2009. Assessment of mercury-polluted oils adjacent to an old mercury-fulminate production plant. Appl. Environ. Soil Sci. 2009, 1-8.

Balci, N., Shanks III, W.C., Mayer, B., Mandernack, K.W. 2007. Oxygen and sulfur isotope systematics of sulfate produced by bacterial and abiotic oxidation of pyrite. Geochim. Cosmochim. Acta 71, 3796-3811.

Balistrieri, L.S., Chao, T.T., 1990. Adsorption of selenium by amorphous iron oxyhydroxide and manganese dioxide. Geochim. Cosmochim. Acta 54, 739-751.

Ball, J.W., Nordstrom, D.K., 1991. User's manual for WATEQ4F with revised thermodynamic database and test cases for calculating speciation of major, trace and redox elements in natural waters, U.S. Geol. Surv. Open-File Rep. 91-183.

Barkay, T., Gillman, M., Turner, R.R., 1997. Effects of dissolved organic carbon and salinity on bioavailability of mercury. Appl. Environ. Microbiol. 63, 4267-4271.

Barnett, M.O., Harris, L.A., Turner, R.R., Henson, T.J., Melton, R.E., Stevenson, R.J., 1995. Characterization of mercury species in contaminated floodplain soils. Water Air Soil Pollut. 80, 1105-1108.

Barrow, N.J., Cox, C., 1992a. The effects of pH and chloride concentration on mercury sorption. I. By goethite. J. Soil Sci. 43, 295-304.

Barrow, N.J., Cox, V.C., 1992b. The effects of pH and chloride concentration on mercury sorption. II. By a soil. J. Soil Sci. 43, 305-312.

Benner, S.G., Blowes, D.W., Gould, W.D., Herbert Jr., R.B., Ptacek, C.J., 1999. Geochemistry of a permeable reactive barrier for metals and acid mine drainage. Environ. Sci. Technol. 33, 2793-2799.

Benner, S.G., Blowes, D.W., Ptacek, C.J., Mayer, K.U., 2002. Rates of sulfate reduction and metal sulfide precipitation in a permeable reactive barrier. Appl. Geochem. 17, 301-320.

Bernhaus, A., Gaona, X., van Ree, D., Valiente, M., 2006. Determination of mercury in polluted soils surrounding a chlor-alkali plant. Direct speciation by X-ray absorption spectroscopy techniques and preliminary geochemical characterization. Anal. Chim. Acta 565, 73-80.

Bloom, N.S., Preus, E., Katon, J., Hiltner, M., 2003. Selective extractions to assess the biogeochemically relevant fractionation of inorganic mercury in sediments and soils. Anal. Chim. Acta 479, 233–248.

Blowes, D.W., Ptacek, C.J., Benner, S.G., McRae, C.W.T., Bennet, T.A., Puls, R.W., 2000. Treatment of inorganic contaminants using permeable reactive barriers. J. Contam. Hydrol. 45, 123-137.

Blowes, D.W., Ptacek, C.J., Jambor, J.L., Weisener, C.G., 2003. The geochemistry of acid mine drainage. Treatise Geochem. 9, 179-204.

Blue, L.Y., Jana, P., Atwood, D.A., 2010. Aqueous mercury precipitation with the synthetic dithiolate, $BDTH_2$. Fuel 89, 1326-1330.

Bonnissel-Gissinger, P., Alnot, M., Lickes, J-P., Ehrhardt, J-J., Behra, P., 1999. Modeling the adsorption of mercury(II) on (hydr)oxides II: α-FeOOH (Goethite) and amorphous silica. J. Colloid Interface Sci. 215, 313-322.

Boszke, L., Kowalski, A., Siepak, J., 2004. Grain size partitioning of mercury in sediments of the Middle Odra River (Germany/Poland). Water Air Soil Pollut. 159, 125-138.

Boszke, L., Kowalski, A., Szczuciński, W., Rachlewicz, G., Lorenc, S., Siepak, J., 2006. Assessment of mercury mobility and bioavailability by fractionation method in sediments from coastal zone inundated by the 26 December 2004 tsunami in Thailand. Environ. Geol. 51, 527-536.

Boszke, L., Kowalski, A., Astel, A., Barański, A., Gworek, B., Siepak, J., 2008. Mercury mobility and bioavailability in soil from contaminated area. Environ. Geol. 55, 1075-1087.

Boudreau, B.P., Westrich, J.T., 1984. The dependence of bacterial sulfate reduction on sulfate concentration in marine sediments. Geochim. Cosmochim. Acta 48, 2503-2516.

Brunner, B., Bernasconi, S.M., 2005. A revised isotope fractionation model for dissimilatory sulfate reduction in sulfate reducing bacteria. Geochim. Cosmochim. Acta 69, 4759-4771.

Caetano, M., Madureira, M-J., Vale, C., 2003. Metal remobilization during resuspension of anoxic contaminated sediment: short-term laboratory study. Water Air Soil Pollut. 143, 23-40.

Campbell, K.Y., Ford, C.J., Levine, D.A., 1998. Mercury distribution in Poplar Creek, Oak Ridge, Tennessee, USA. Environ. Toxicol. Chem. 17, 1191-1198.

Canfield, D.E., 2001. Isotope fractionation by natural populations of sulfate-reducing bacteria. Geochim. Cosmochim. Acta 65, 1117-1124.

Caron, S. and Lucotte, M., 2008. Regional and seasonal inputs of mercury into Lake St. Pierre (St. Lawerence River), a major commercial and sport fisheries in Canada. Water Air Soil Pollut. 195, 85-97.

Chang, T.C., Yen, J.H., 2006. On-site mercury-contaminated soils remediation by using thermal desorption technology. J. Hazard. Mater. B128, 208-217.

Chen, C-C., McKimmy, E.J., Pinnavaia, T.J., Hayes, K.F., 2004. XAS study of mercury(II) ions trapped in mercaptan-functionalized mesostructured silicate with a wormhole framework structure. Environ. Sci. Technol. 38, 4758-4762.

Chen, H. and Wang, A., 2007. Kinetic and isothermal studies of lead ion adsorption onto palygorskite clay. J. Colloid Interface Sci. 307, 309-316.

Clark, I., Fritz, P., 1997. Environmental Isotopes in Hydrogeology. CRC Press, New York, NY. 328 pp.

Clarkson, T.W. and Magos, L., 2006. The toxicology of mercury and its chemical compounds. Crit. Rev. Toxicol. 36, 609-662.

Combs, G.F., Garbisu, C., Yee, B.C., Yee, A., Donald, D.E., Smith, N.R., Magyarosy, A.C., Leighton, T., Buchanan, B.B., 1996. Bioavailability of selenium accumulated by selenite-reducing bacteria. Biol. Trace Elem. Res. 52, 209-225.

Compeau, G.C. and Bartha, R., 1984. Methylation and demethylation of mercury under controlled redox, pH, and salinity conditions. Appl. Environ. Microbiol. 48, 1203-1207.

Compeau, G.C. and Bartha, R., 1985. Sulfate-reducing bacteria: principal methylators of mercury in anoxic estuarine sediment. Appl. Environ. Microbiol. 50, 498-502.

DeHobre, M.M.M., Nobre, R.C.M., Galvaõ, A.S.S., 2006. Remediation of mercury contaminated groundwater using a permeable reactive barrier. 5th ICEG Environmental Geotechnics: Opportunities, Challenges, and Responsibilities for Environmental Geotechnics – Proceedings of the ISSMGE 5th International Congress. Volume I, 213-220.

Dhillon, K.S. and Dhillon, S.K., 1999. Adsorption-desorption reactions of selenium in some soils of India. Geoderma 93, 19-31.

Dmytriw, R., Mucci, A., Lucotte, M., Pichet, P., 1995. The partitioning of mercury in the solid components of dry and flooded forest soils and sediments from a hydroelectric reservoir, Quebec (Canada). Water Air Soil Pollut. 80, 1099-1103.

Domagalski, J.L., Alpers, C.N., Slotton, D.G., Suchanek, T.H., Ayers, S.M., 2004. Mercury and methylmercury concentrations and loads in the Cache Creek watershed, California. Sci. Total Environ. 327, 215-237.

Duc, M., Lefevre, G., Fédoroff, M., 2006. Sorption of selenite ions on hematite. J. Colloid Interface Sci. 298, 556-563.

Ellis, A.S., Johnson, T.M., Bullen, T.D., 2002. Chromium isotopes and the fate of hexavalent chromium in the environment. Science 295, 2060-2062.

Elwood, J.W., 1984. Mercury contamination in Polar Creek and the Clinch River. ORNL/TM-8893, Oak Ridge National Laboratory, Oak Ridge, TN, USA.

Farrah, H., Pickering, W.F., 1978. The sorption of mercury species by clay minerals. Water Air Soil Pollut. 9, 23-31.

Fitzgerald, W.F., Clarkson, T.W., 1991. Mercury and monomethylmercury: present and future concerns. Environ. Health Perspect. 96, 159-166.

Fleming, E.J., Mack, E.E., Green, P.G., Nelson, D.C., 2006. Mercury methylation from unexpected sources: molybdate-inhibited freshwater sediments and an iron-reducing bacterium. Appl. Environ. Microbiol. 72, 457-464.

Flemming, B.W., 2000. A revised textural classification of gravel-free muddy sediments on the basis of ternary diagrams. Cont. Shelf Res. 20, 1125-1137.

Friedli, H.R., Arellano, A.F., Cinnirella, S., Pirrone, N., 2009. Initial estimates of mercury emissions to the atmosphere from global biomass burning. Environ. Sci. Technol. 43, 3507-3513.

Fuhrmann, M., Melamed, D., Kalb, P.D., Adams, J.W., Milian, L.W., 2002. Sulfur polymer solidification/stabilization of elemental mercury waste. Waste Manage. 22, 327-333.

Genin, F., Alnot, M., Ehrhardt, J.J., 2001. Interaction of vapours of mercury with PbS(0 0 1): a study by X-ray photoelectron spectroscopy, RHEED and X-ray absorption spectroscopy. Appl. Surf. Sci. 173, 44-53.

Génin, J-M.R., Refait, P., Bourrié, G., Abdelmoula, M., Trolard, F., 2001. Structure and stability of the Fe(II)-Fe(III) green rust "fougerite" mineral and its potential for reducing pollutants in soil solutions. Appl. Geochem. 16, 559-570.

Gilmour, C.C., Henry, E.A., 1991. Mercury methylation in aquatic systems affected by acid deposition. Environ. Pollut. 71, 131-169.

Gilmour, C.C., Henry, E.A., Mitchell, R., 1992. Sulfate stimulation of mercury methylation in freshwater sediments. Environ. Sci. Technol. 26, 2281-2287.

Goh, K.-H., Lim, T.-T., 2004. Geochemistry of inorganic arsenic and selenium in a tropical soil: effect of reaction time, pH, and competitive anions on arsenic and selenium adsorption. Chemosphere 55, 849-859.

Grossman, E.L., Cifuentes, L.A., Cozzarelli, I.M., 2002. Anaerobic methane oxidation in a landfill-leachate plume. Environ. Sci. Technol. 36, 2436-2442.

Guo, Q., Blowes, D.W., 2009. Biogeochemistry of two types of permeable reactive barriers, organic carbon and iron-bearing organic carbon for mine drainage treatment: Column experiments. J. Contam. Hydrol. 107, 128-139.

Habicht, K.S., Canfield, D.E., 1997. Sulfur isotope fractionation during bacterial sulfate reduction in organic-rich sediments. Geochim. Cosmochim. Acta 61, 5351-5361.

Harrison, A.G., Thode, H.G., 1958. Mechanism of the bacterial reduction of sulphate from isotope fractionation studies. Trans. Faraday Soc. 54, 84-92.

Hayashi, H., Kanie, K., Shinoda, K., Muramatsu, A., Suzuki, S., Sasaki, H., 2009. pH-dependence of selenate removal from liquid phase by reductive Fe(II)-Fe(III) hydroxysulfate compound, green rust. Chemosphere 76, 638-643.

Herbich, J.B., 1995. Removal of contaminated sediments: equipment and recent field studies. In: Demars, K.R., Richardson, G.N., Yong, R.N., Chaney, R.C. (Eds.), Dredging, Remediation, and Containment of Contaminated Sediments, ASTM STP 1293, American Society for Testing and Materials, Philadelphia, pp. 77-111.

Hockin, S.L., Gadd, G.M., 2003. Linked redox precipitation of sulfur and selenium under anaerobic conditions by sulfate-reducing bacterial biofilms. Appl. Environ. Microbiol. 69, 7063-7072.

Hojdová, M., Navrátil, T., Rohovec, J., Penížek, V., Grygar, T., 2009. Mercury distribution and speciation in soils affected by historic mercury mining. Water Air Soil Pollut. 200, 89-99.

Holley, E.A., McQuillan, A.J., Craw, D., Kim, J.P., Sander, S.G., 2007. Mercury mobilization by oxidative dissolution of cinnabar (α-HgS) and metacinnabar (β-HgS). Chem. Geol. 240, 313-325.

Hopkinson, Jr., C.S., 1985. Shallow-water benthic and pelagic metabolism: evidence of heterotrophy in the nearshore Georgia Bight. Mar. Biol. 87, 19-32.

Howard III, J.H. 1977. Geochemistry of selenium: formation of ferroselite and selenium behavior in the vicinity of oxidizing sulfide and uranium deposits. Geochim. Cosmochim. Acta 41, 1665-1678.

Hunerlach, M.P., Alpers, C.N., Marvin-DiPasquale, M.C., Taylor, H.E., De Wild, J.F. 2004. Geochemistry of fluvial sediment impounded behind Daguerre Point Dam, Yuba River, California, U.S. Geological Survey Scientific Investigations Reports 2004-5165, 66 p.

Ingvorsen, K., Zehnder, A.J.B., Jørgensen, B.B., 1984. Kinetics of sulfate and acetate uptake by Desulfobacter postgatei. Appl. Environ. Microbiol. 47, 403-408.

Jackson, T.A., 1989. The influence of clay minerals, oxides, and humic matter on the methylation and demethylation of mercury by micro-organisms in freshwater sediments. Appl. Organomet. Chem. 3, 1-30.

Jay, J.A., Morel, F.M.M., Hemond, H.F., 2000. Mercury speciation in the presence of polysulfides. Environ. Sci. Technol. 34, 2196-2200.

Johnson, D.B., Hallberg, K.B., 2005. Acid mine drainage remediation options: a review. Sci. Total Environ. 338, 3-14.

Kelly, C.A., Rudd, J.M.W., Holoka, M.H., 2003. Effect of pH on mercury uptake by an aquatic bacterium: implications for Hg cycling. Environ. Sci. Technol. 37, 2941-2946.

Kerin, E., Gilmour, C.C., Roden, E., Suzuki, M.T., Coates, J.D., Mason, R.P. 2006. Mercury methylation among the dissimilatory iron-reducing bacteria. Appl. Environ. Microbiol. 72, 7919-7921.

Kim, C.S., Brown, Jr., G.E., Rytuba, J.J., 2000. Characterization and speciation of mercury-bearing mine wastes using X-ray absorption spectroscopy. Sci. Total Environ. 261, 157-168.

Kim, C.S., Rytuba, J.J., Brown Jr., G.E., 2004. EXAFS study of mercury (II) sorption to Fe- and Al-(hydr)oxides I. Effects of pH. J. Colloid Interface Sci. 270, 9-20.

King, J.K., Kostka, J.E., Frischer, M.E., Saunders, F.M., 2000. Sulfate-reducing bacteria methylate mercury at variable rates in pure culture and in marine sediments. Appl. Environ. Microbiol. 66, 2430-2437.

King, J.K., Kostka, J.E., Frischer, M.E., Saunders, F.M., Jahnke, R.A., 2001. A quantitative relationship that demonstrates mercury methylation rates in marine sediments are based on the community composition and activity of sulfate-reducing bacteria. Environ. Sci. Technol. 35, 2491-2496.

Knocke, W.R., Hemphill, L.H., 1981. Mercury(II) sorption by waste rubber. Water Res. 15, 275-282.

Knöller, K., Vogt, C., Feisthauer, S., Weise, S.M., Weiss, H., Richnow, H.-H. 2008. Sulfur cycling and biodegradation in contaminated aquifers: insights from stable isotope investigations. Environ. Sci. Technol. 42, 7807-7812.

Knöller, K., Schubert, M. 2010. Interaction of dissolved and sedimentary sulfur compounds in contaminated aquifers. Chem . Geol. 276, 284-293.

Kocman, D., Horvat, M., Kotnik, J. 2004. Mercury fractionation in contaminated soils from the Idrija mercury mine region. J. Environ. Monit. 6, 696-703.

Kucharski, R., Zielonka, U., Sas-Nowosielska, A., Kuperberg, J.M., Worsztynowicz, A., Szdzuj, J., 2005. A method of mercury removal from topsoil using low-thermal application. Environ. Model. Assess. 104, 341-351.

Kunkel, A.M., Seibert, J.J., Elliott, L.J., Kelley, R.L., Katz, L.E., Pope, G.A. 2006. Remediation of elemental mercury using in situ themral desorption (ISTD). Environ. Sci. Technol. 40, 2384-2389.

Lezzi, A., Cobianco, S., Roggero, A., 1994. Synthesis of thiol chelating resins and their adsorption properties toward heavy metal ions. J. Polym. Sci., Part A: Polym. Chem. 32, 1877-1883.

Li, Y.H., Lee, C.W., Gullet, B.K., 2002. The effect of activated carbon surface moisture on low temperature mercury adsorption. Carbon 40, 65-72.

Lindsay, M.B.J., Ptacek, C.J., Blowes, D.W., Gould, W.D., 2008. Zero-valent iron and organic carbon mixtures for remediation of acid mine drainage: batch experiments. Appl. Geochem. 23, 2214-2225.

Lindsay, M.B.J., Blowes, D.W., Condon, P.D., Ptacek, C.J., 2009. Managing pore-water quality in mine tailings by inducing microbial sulfate reduction. Environ. Sci. Technol. 43, 7086-7091.

Liu, C., Jay, J.A., Ika, R., Shine, J.P., Ford, T.E., 2001. Capping efficiency for metal-contaminated marine sediment under conditions of submarine groundwater discharge. Environ. Sci. Technol. 35, 2334-2340.

Liu, G., Cabrera, J., Allen, M., Cai, Y., 2006. Mercury characterization in a soil sample collected nearby the DOE Oak Ridge Reservation utilizing sequential extraction and thermal desorption method. Sci. Total Environ. 369, 384.392.

Lo, S.-L., Chen, T.-Y., 1997. Adsorption of Se(IV) and Se(VI) on an iron-coated sand from water. Chemosphere 35(4), 919-930.

Loring, D.H., 1975. Mercury in the sediments of the Gulf of St. Lawerence. Can. J. Earth Sci. 12, 1219-1237.

MacLeod, C.L., Borcsik, M.P., Jaffé, P.R., 1996. Effect of infiltrating solutions on the desorption of mercury from aquifer sediments. Environ. Technol. 17, 465-475.

Marvin-DiPasquale, M.C. and Oremland, R.S., 1998. Bacterial methylmercury degradation in Florida Everglades peat sediment. Environ. Sci. Technol. 32, 2556-2563.

Marvin-DiPasquale, M., Agee, J., McGowan, C., Oremland, R.S., Thomas, M., Krabbenhoft, D., Gilmour, C.C., 2000. Methyl-mercury degradation pathways: a comparison among three mercury-impacted ecosystems. Environ. Sci. Technol. 34, 4908-4916.

Masscheleyn, P.H., Delaune, R.D., Patrick, Jr., W.H., 1990. Transformations of selenium as affected by sediment oxidation-reduction potential and pH. Environ. Sci. Technol. 24, 91-96.

Matheson, L.J., Tratnyek, P.G., 1994. Reductive dehalogenation of chlorinated methanes by iron metal. Environ. Sci. Technol. 28, 2045-2053.

Matlock, M.M., Howerton, B.S., Atwood, D.A. 2001. Irreversible precipitation of mercury and lead. J. Hazard. Mat. B 84, 73-82.

Mayer, K.U., Frind, E.O., Blowes, D.W., 2002. Multicomponent reactive transport modeling in variably saturated porous media using a generalized formulation for kinetically controlled reactions. Water Resour. Res., 38, 1174, 21 pp.

Menheer, M.A., 2004. Development of a benthic-flux chamber for measurement of ground-water seepage and water sampling for mercury analysis at the sediment-water interface. U.S. Geological Survey Scientific Investigation Report 2004-5298, 14 pp.

Meschede, T., Vogelsberger, R., 1995. Remediation of a mercury-contaminated site in Egypt. In Van den Brink, W.J., Arendt, F. (eds.). Contaminated Soil ’95. Kluwer, Dordrecht, pp. 237-238.

Mikac, N., Foucher, D., Niessen, S., Lojen, S., Fischer, J.-C., 2003. Influence of chloride and sediment matrix on the extractability of HgS (cinnabar and metacinnabar) by nitric acid, Anal. Bioanal. Chem. 377, 1196-1201.

Moo-Young, H., Myers, T., Tardy, B., Ledbetter, R., Vanadit-Ellis, W., Sellasie, K., 2001. Determination of the environmental impact of consolidation induced convective transport through capped sediment. J. Hazard. Mater. 85, 53-72.

Mucci, A., Lucotte, M., Montgomery, S., Plourde, Y., Pichet, P., Van Tra, H., 1995. Mercury remobilization from flooded soils in a hydroelectric reservoir of northern Quebec, La Grande-2: results of a soil resuspension experiment. Can. J. Fish. Aquat. Sci. 52, 2507-2517.

Myneni, S.C.B., Tokunaga, T.K., Brown, Jr., G.E., 1997. Abiotic selenium redox transformations in the presence of Fe(II,III) oxides. Science 278, 1106-1109.

Narasingarao, P., Häggblom, M.M., 2007. Identification of anaerobic selenate-respiring bacteria from aquatic sediments. Appl. Environ. Microbiol. 73, 3519-3527.

Navarro, A., Cañadas, I., Martinez, D., Rodriguez, J., Mendoza, J.L., 2009. Application of solar thermal desorption to remediation of mercury-contaminated soils. Sol. Energy 83, 1405-1414.

Nelson, D.C., Casey, W.H., Sison, J.D., Mack, E.E., Ahmad, A., Pollack, J.S., 1996. Selenium uptake by sulfur-accumulating bacteria. Geochim. Cosmochim. Acta 60, 3531-3539.

Nordstrom, D.K., 1977. Thermochemical redox equilibria of ZoBell's solution. Geochim. Cosmochim. Acta 41, 1835-1841.

Nordstrom, D.K., 2007. Modeling low-temperature geochemical processes. Treatise Geochem. 5, 1-38.

O’Neil, J.R., 1986. Theoretical and experimental aspects of isotopic fractionation. In: Valley, J.W., Taylor, Jr., H.P., O’Neil, J.R. (Eds.) Stable Isotopes in High Temperature Geological Processes, Rev. Mineral. 16, 1-40.

Oremland, R.S., Hollibaugh, J.T., Maest, A.S., Presser, T.S., Miller, L.G., Culbertson, C.W., 1989. Selenate reduction to elemental selenium by anaerobic bacteria in sediments and culture: biogeochemical significance of a novel, sulfate-independent respiration. Appl. Environ. Microbiol. 55, 2333-2343.

Oremland, R.S., Culbertson, C.W., Winfrey, M.R., 1991. Methylmercury decomposition in sediments and bacterials cultures: involvement of methanogens and sulfate reducers in oxidative demethylation. Appl. Environ. Microbiol. 57, 130-137.

Oremland, R.S., Miller, L.G., Dowdle, P., Connel, T., Barkay, T., 1995. Methylmercury oxidative degradation potentials in contaminated and pristine sediments of the Carson River, Nevada. Appl. Environ. Microbiol. 61, 2745-2753.

Oremland, R.S., Herbel, M.J., Blum, J.S., Langley, S., Beveridge, T.J., Ajayan, P.M., Sutto, T., Ellis, A.V., Curran S., 2004. Structural and spectral features of selenium nanospheres produced by Se-respiring bacteria. Appl. Environ. Microbiol. 70, 52-60.

Oubagaranadin, J.U.K., Sathyamurthy, N., Murthy, Z.V.P., 2007. Evaluation of Fuller's earth for the adsorption of mercury from aqueous solutions: A comparative study with activated carbon. J. Hazard. Mater. 142, 165-174.

Pak, K.-R., Bartha, R., 1998. Mercury methylation and demethylation in anoxic lake sediments and by strictly anaerobic bacteria. Appl. Environ. Microbiol. 64, 1013-1017.

Paquette, K., Helz, G., 1995. Solubility of cinnabar (red HgS) and implications for mercury speciation in sulfidic waters. Water Air Soil Pollut. 80, 1053-1056.

Paul, M.C., Toia, R.F., von Nagy-Felsobuki, E.I., 2003. A novel method for the determination of mercury and selenium in shark tissue using high-resolution inductively coupled plasma-mass spectrometry. Spectrochim. Acta Part B 58, 1687-1697.

Paulsson, K., Lundbergh, K., 1989. The selenium method for treatment of lakes for elevated levels of mercury in fish. Sci. Total Environ. 87/88, 495-507.

Paulsson, K., Lundbergh, K., 1991. Treatment of mercury contaminated fish by selenium addition. Water Air Soil Pollut. 56, 833-841.

Plant, J.A., Kinniburgh, D.G., Smedley, P.L., Fordyce, F.M., Klinck, B.A. in Treatise on Geochemistry (eds Holland, H.D. & Turekian, K.K.) Vol. 9, Environmental Geochemistry (ed. Lollar, B.S.) 17-66 (Elsevier-Pergamon, Oxford, 2003).

Ponder, S.M., Darab, J.G., Mallouk, T.E., 2000. Remediation of Cr(VI) and Pb(II) aqueous solutions using supported, nanoscale zero-valent iron. Environ. Sci. Technol. 34, 2564-2569.

Ravel, B., Newville, M., 2005. ATHENA, ARTEMIS, HEPHAESTUS: data analysis for X-ray absorption spectroscopy using IFEFFIT. J. Synchrotron Rad. 12, 537-541.

Ravichandran, M., Aiken, G.R., Reddy, M.M., Ryan, J,N., 1998. Enhanced dissolution of cinnabar (mercuric sulfide) by dissolved organic matter isolated from the Florida Everglades. Environ. Sci. Technol. 32, 3305-3311.

Ravichandran, M., Aiken, G.R., Ryan, J.N., Reddy, M.M. 1999. Inhibition of precipitation and aggregation of metacinnabar (mercuric sulfide) by dissolved organic matter isolated from the Florida Everglades. Environ. Sci. Technol. 33, 1418-1423.

Ravichandran, M. 2004. Interactions between mercury and dissolved organic matter: a review. Chemosphere 55, 319-331.

Reddy, M.M., Aiken, G.R. 2000. Fulvic acid-sulfide ion competition for mercury ion binding in the Florida Everglades. Water Air Soil Pollut. 132, 89-104.

Rees, C.E., 1973. A steady-state model for sulphur isotope fractionation in bacterial reduction processes. Geochim. Cosmochim. Acta 37, 1141-1162.

Reis, A.T., Rodrigues, S.M., Araújo, C., Coelho, J.P., Pereira, E., Duarte, A.C., 2009. Mercury contamination in the vicinity of a chlor-alkali plant and potential risks to local population. Sci. Total Environ. 407, 2689-2700.

Robertson, W.D., Blowes, D.W., Ptacek, C.J., Cherry, J.A., 2000. Long-term performance of in situ reactive barriers for nitrate remediation. Ground Water 38, 689-695.

Roden, E.E., Tuttle, J.H., 1993. Inorganic sulfur turnover in oligohaline estuarine sediments. Biogeochemistry 22, 81-105.

Roux, M., Sarret, G., Pignot-Paintrand, I., Fontecave, M., Coves, J., 2001. Mobilization of selenite by Ralstonia metallidurans CH34. Appl. Environ. Microbiol. 67, 769-773.

Roychoudhury, A.N., Viollier, E., Van Cappellen, P., 1998. A plug flow-through reactor for studying biogeochemical reactions in undisturbed aquatic sediments. Appl. Geochem. 13, 269-280.

Rudd, J.W.M., Turner, M.A., Furutani, A., Swick, A.L., Townsend, B.E., 1983. The English-Wabigoon river system: I. A synthesis of recent research with a view towards mercury amelioration. Can. J. Fish. Aquat. Sci. 40, 2206-2217.

Ryser, A.L., Strawn, D.G., Marcus, M.A., Fakra, S., Johnson-Maynard, J.L., Möller, G., 2006. Microscopically focused synchrotron X-ray investigation of selenium speciation in soils developing on reclaimed mine lands. Environ. Sci. Technol. 40, 462-467.

Santoro, A., Terzano, R., Blo, G., Fiore, S., Mangold, S., Ruggiero, P., 2010. Mercury speciation in the colloidal fraction of a soil polluted by a chlor-alkali plant: a case study in the South of Italy. J. Synchrotron Radiat. 17, 187-192.

Sarkar, D., 2003. Preliminary studies on mercury solubility in the presence of iron oxides using static headspace analysis. Environ. Geosci. 10, 151-155.

Sasaki, K., Blowes, D.W., Ptacek, C.J., Gould, W.D., 2008a. Immobilization of Se(VI) in mine drainage by permeable reactive barriers: column performance. Appl. Geochem. 23, 1012-1022.

Sasaki, K., Blowes, D.W., Ptacek, C.J., 2008b. Spectroscopic study of precipitates formed during removal of selenium from mine drainage spiked with selenate using permeable reactive materials. Geochem. J. 42, 283-294.

Sayers, D.E., Stern, E.A., Lytle, F.W. 1971. New technique for investigating noncrystalline structures: Fourier analysis of the extended X-ray – absorption fine structure. Phys. Rev. Lett. 27, 1204-1207.

Scheuhammer, A.M., Meyer, M.W., Sanheinrich, M.B., Murray, M.W. 2007. Effects of environmental methylmercury on the health of wild birds, mammals, and fish. Ambio 36, 12-19.

Schuster, E., 1991. The behavior of mercury in the soil with special emphasis on complexation and adsorption processes – a review of the literature. Water Air Soil Pollut. 56, 667-680.

Seiler, R.L., 1995. Prediction of areas where irrigation drainage may induce selenium contamination of water. J. Environ. Qual. 24, 973-979.

Shamberger, R.J., 1981. Selenium in the environment. Sci. Total Environ. 17, 59-74.

Siddique, T., Zhang, Y., Okeke, B.C., Frankenberger, Jr., W.T., 2006. Characterization of sediment bacteria involved in selenium reduction. Bioresour. Technol. 97, 1041-1049.

Simpson, S.L., Pryor, I.D., Mewburn, B.R., Batley, G.E., Jolley, D., 2002. Considerations for capping metal-contaminated sediments in dynamic estuarine environments. Environ. Sci. Technol. 36, 3772-3778.

Skyllberg, U., Bloom, P.R., Qian, J., Lin, C-M., Bleam, W.F., 2006. Complexation of mercury(II) in soil organic matter: EXAFS evidence for linear two-coordination with reduced sulfur groups. Environ. Sci. Technol. 40, 4174-4180.

Stern, E.A., Heald, S.M. Basic principles and applications of EXAFS. In E.E. Koch (ed.) Handbook of synchrotron radiation. Vol. 10. North-Holland, Amsterdam.

Stolz, J.F., Oremland, R.S., 1999. Bacterial respiration of arsenic and selenium. FEMS Microbiol. Rev. 23, 615-627.

Slowey, A.J., Brown Jr., G.E., 2007. Transformations of mercury, iron, and sulfur during the reductive dissolution of iron oxyhydroxide by sulfide. Geochim. Cosmochim. Acta 71, 877-894.

Stordal, M.C., Gill, G.A., Wen, L.-S., Santschi, P.H., 1996. Mercury phase speciation in the surface waters of three Texas estuaries: Importance of colloidal forms. Limnol. Oceanogr. 41, 52-61.

Suchanek, T.H., Mullen, L.H., Lamphere, B.A., Richerson, P.J., Woodmansee, C.E., Slotton, D.G., Harner, E.J., Woodward, L.A., 1998. Redistribution of mercury from contaminated lake sediment of Clear Lake, California. Water Air Soil Pollut. 104, 77-102.

Suchanek, T.H., Cooke, J., Keller, K., Jorgensen, S., Richerson, P.J., Eagles-Smith, C.A., Harner, E.J., Adam, D.P., 2009. A mass balance mercury budget for a mine-dominated lake: Clear Lake, California. Water Air Soil Pollut 196, 51-73.

Tempel, R.N., Shevenell, L.A., Lechler, P., Price, J., 2000. Geochemical modeling approach to predicting arsenic concentrations in a mine pit lake. Appl. Geochem. 15, 475-492.

Thode, H.G., Monster, J., 1965. Sulfur-isotope geochemistry of petroleum, evaporites, and ancient seas. Am. Assoc. Petrol. Geol. Mem. 4, 367-377.

Tiffreau, C., Lützenkirchen, J., Behra, P., 1995. Modeling the adsorption of mercury(II) on (hydr)oxides I: amorphous iron oxide and α-quartz. J Colloid Interface Sci. 172, 82-93.

Tomiyasu, T., Matsuyama, A., Eguchi, T., Fuchigami, Y., Oki, K., Horvat, M., Rajar, R., Akagi, H., 2006. Spatial variations of mercury in sediment of Minamata Bay, Japan. Sci. Total Environ. 368, 283-290.

Tsuda, T., Yorifuji, T., Takao, S., Miyai, M., Babazono, A., 2009. Minamata disease: Catastrophic poisoning due to a failed public health response. J. Pub. Health Pol. 30, 54-67.

Ullrich, S.M., Tanton, T.W., Abdrashitova, S.A., 2001. Mercury in the aquatic environment: a review of factors affecting methylation. Crit. Rev. Environ. Sci. Technol. 31, 241-293.

U.S. EPA. 1983. Method 160.3. Methods for chemical analysis of water and wastes. EPA 600-4-79-020.

U.S. EPA. 1993. Solidification/Stabilization and its Application to Waste Materials. EPA 530-R-93-012.

U.S. EPA. 1996a. Method 1638. Determination of trace elements in ambient waters by inductively coupled plasma – mass spectrometry. EPA 821-R-96-005.

U.S. EPA. 1996b. Test Methods for Evaluating Solid Waste, SW-846, 3rd ed., Office of Solid Waste: Washington, DC.

U.S. EPA. 1996c. Evaluation of dredged material proposed for discharge in waters of the U.S. – Testing Manual. EPA 823-B-98-004.

U.S. EPA. 2002. Method 1631, Revision E: Mercury in water by oxidation, purge and trap, and cold vapor atomic fluorescence spectrometry. EPA 821-R-02-019.

U.S. EPA, Office of Water, 2009. National Primary Drinking Water Regulations. EPA 816-F-09-0004.

Van Breukelen, B.M., Griffioen, J., Röling, W.F.M., van Verseveld, H.W., 2004. Reactive transport modelling of biogeochemical processes and carbon isotope geochemistry inside a landfill leachate plume. J. Contam. Hydrol. 70, 249-269.

Van Breukelen, B.M., Hunkeler, D., Volkering, F., 2005. Quantification of sequential chlorinated ethane degradation by use of a reactive transport model incorporating isotope fractionation. Environ. Sci. Technol. 39, 4189-4197.

Van Breukelen, B.M., 2007. Quantifying the degradation and dilution contribution to natural attenuation of contaminants by means of an open system Rayleigh equation. Environ. Sci. Technol. 41, 4980-4985.

Van Breukelen, B.M., Prommer, H., 2008. Beyond the Rayleigh equation: reactive transport modeling of isotope fractionation effects to improve quantification of biodegradation. Environ. Sci. Technol. 42, 2457-2463.

Wainright, S.C., 1987. Stimulation of heterotrophic microplankton production by resuspended marine sediments. Science 238, 1710-1712.

Wang, Q., Kim, D., Dionysiou, D.D., Sorial, G.A., Timberlake, D., 2004. Sources and remediation for mercury contamination in aquatic systems – a literature review. Environ. Pollut. 131, 323-336.

Waples, J.S., Nagy, K.L., Aiken, G.R., Ryan, J.N., 2005. Dissolution of cinnabar (HgS) in the presence of natural organic matter. Geochim. Cosmochim. Acta 69, 1575-1588.

Waybrant, K.R., Ptacek, C.J., Blowes, D.W., 2002. Treatment of mine drainage using permeable reactive barriers: column experiments. Environ. Sci. Technol. 36, 1349-1356.

Weisener, C.G., Sale, K.S., Smyth, D.J.A., Blowes, D.W., 2005. Field column study using zero valent iron for mercury removal from contaminated groundwater. Environ. Sci. Technol. 39, 6306-6312.

Wolfenden, S., Charnock, J.M., Hilton, J., Livens, F.R., Vaughan, D.J., 2005. Sulfide species as a sink of mercury in lake sediments. Environ. Sci. Technol. 39, 6644-6648.

World Health Organization (WHO). Trace Elements in Human Nutrition and Health. World Health Organization, Geneva, 1996.

Xia, K., Skyllberg, U.L., Bleam, W.F., Bloom, P.R., Nater, E.A., Helmke, P.A., 1999. X-ray absorption spectroscopic evidence for the complexation of Hg(II) by reduced sulfur in soil humic substances. Environ. Sci. Technol. 33, 257-261.

Zaman, K.M., Blue, L.Y., Huggins, F.E., Atwood, D.A. 2007. Cd, Hg, and Pb compounds of benzene-1,3-diamidoethanethiol ($BDETH_2$). Inorg. Chem. 46, 1975-1980.

Zavarin, M., 1999. Sorptive properties of synthetic and soil carbonates for selenium, nickel, and manganese. PhD Thesis, University of California-Berkeley, Berkeley, CA, 279 pp.

Zehr, J.P. and Oremland, R.S., 1987. Reduction of selenate to selenide by sulfate-respiring bacteria: experiments with cell suspensions and estuarine sediments. Appl. Environ. Microbiol. 53, 1365-1369.

Zhang, H. and Lindberg, S.E., 2001. Sunlight and iron(III)-induced photochemical production of dissolved gaseous mercury in freshwater. Environ. Sci. Technol. 35, 928-935.

Zhang, Y., Wang, J., Amrhein, C., Frankenberger, Jr., W.T., 2005. Removal of selenate from water by zerovalent iron. J. Environ. Qual. 34, 487-495.

Zhang, Y. and Frankenberger, Jr., W.T., 2006. Removal of selenate in river and drainage waters by Citrobacter braakii enhanced with zero-valent iron. J. Agric. Food Chem. 54, 152-156.

Zhuang, J.M., Walsh, T., Lam. T., Boulter, D., 2003a. Application of a ferric sludge to immobilize leachable mercury in coils and concrete. Environ. Technol. 24, 1445-1453.

Zhuang, J.M., Walsh, T., Lam, T., 2003b. A new technology for the treatment of mercury contaminated water and soil. Environ. Technol. 24, 897-902.

Zingaro, R.A., Dufner, D.C., Murphy, A.P., Moody, C.D., 1997. Reduction of oxoselenium anions by iron(II) hydroxide. Environ. Int. 23, 299-304.

Appendix A:

Summary of Data Presented in Chapter 2

Table A.1 Summary of general chemistry, cation and anion concentrations, and rate constant calculations from batch experiments.

reactive mixture	time (h)	pH	Eh (mV)	concentration (mg L^{-1})				rate constant (s^{-1})
				Alk ($CaCO_3$)	SO_4	Fe	Se	$\ln(C_0/C)$
GI	0	6.19	-145	8	990	0.1	310	0.00
	6	5.98	-335	23	820	32	230	0.27
	24	7.19	-415	10	820	13	150	0.69
	48	7.65	-420	40	820	7.0	110	1.0
	72	8.34	-440	17	810	1.1	58	1.7
	96	8.44	-430	19	830	1.3	46	2.0
	120	8.67	-435	14	830	0.7	32	2.4
OC	0	6.19	-145	8	990	0.1	310	0.00
	6	7.84	-300	190	1000	0.3	260	0.15
	24	7.94	-230	220	1000	0.3	260	0.16
	48	8.08	-360	210	1000	0.4	270	0.14
	72	8.13	-335	240	1000	0.5	260	0.16
	96	8.13	-340	260	1000	3.2	260	0.17
	120	8.14	-345	240	1000	0.6	260	0.15
GI+OC	0	6.19	-145	8	990	0.1	310	0.00
	6	7.45	-405	160	940	2.8	260	0.15
	24	7.73	-410	n/a	940	3.6	240	0.26
	48	8.14	-420	78	930	3.5	230	0.30
	72	8.24	-425	86	950	3.4	220	0.34
	96	8.35	-430	110	950	2.9	210	0.38
	120	8.23	-390	110	970	3.2	190	0.48

n/a = not analyzed; Alk = alkalinity (mg L^{-1} $CaCO_3$); GI = granular Fe^0; OC = organic carbon; GI-OC = mixture of Fe^0 and organic carbon

Table A.2 Summary of major elemental analysis performed by Thermo iCAP 6000 (ICP-OES). Concentrations are reported at different optical emission wavelengths.

sample	time (h)	concentration (mg L^{-1})							
		Ca (317.9 nm)	Ca (370.6 nm)	K (766.4 nm)	K (769.8 nm)	Mg (279.8 nm)	Mg (285.2 nm)	Na (589.5 nm)	Na (818.3 nm)
MDL	-	0.28	0.25	0.44	0.38	0.098	0.10	0.15	0.14
MQL	-	0.28	0.25	0.44	0.38	0.098	0.10	0.15	0.14
input	0	2.7	3.6	120	120	2.1	1.1	570	580
GI	6	1.1	1.4	54	49	0.22	0.30	570	580
	24	32	32	380	380	11	10	700	710
	48	1.3	1.5	21	17	< 0.098	0.40	570	570
	72	1.2	1.8	16	16	0.35	0.34	560	560
	96	2.1	1.7	10	7.8	0.93	0.50	550	580
	120	5.4	6.6	38	37	2.1	1.3	620	640
OC	6	28	29	23	22	6.6	6.4	630	630
	24	35	35	29	28	8.5	8.1	700	710
	48	160	161	38	33	8.6	8.8	710	740
	72	36	36	21	21	8.1	7.7	690	710
	96	38	39	28	23	8.8	8.2	700	730
	120	41	41	27	25	8.1	8.9	690	710
GI-OC	6	29	30	15	8.5	7.2	6.1	600	610
	24	31	32	12	12	6.8	6.0	660	680
	48	43	43	69	63	16	16	660	670
	72	30	30	14	13	6.4	5.7	590	590
	96	33	33	13	11	6.4	6.0	650	670
	120	66	66	350	340	17	17	720	730

MDL = method detection limit; MQL = method quantitation limit; GI – granular Fe^0; OC = organic carbon; GI-OC = mixture of Fe^0 and organic carbon

Table A.3 Summary of QA/QC data for the Se calibration data obtained by HR-ICP-MS.

isotope	label	actual Se concentration ($\mu g\ L^{-1}$)	reported Se concentration ($\mu g\ L^{-1}$)	% recovery	N	%RSD
77Se	MDL		7	-	-	-
	MQL		24	-	-	-
	blank	-	< 7	-	3	9
	Std1	10	< 7	-58[a]	1	-
	Std2	30	28	94	1	-
	Std3	100	125	125	1	-
	Std4	300	292	97	1	-
	Std5	1000	569	57[a]	1	-
78Se	MDL		8	-	-	-
	MQL		26	-	-	-
	blank	-	< 8	-	3	11
	Std1	10	< 8	-55[a]	1	-
	Std2	30	29	98	1	-
	Std3	100	123	123	1	-
	Std4	300	293	98	1	-
	Std5	1000	565	57[a]	1	-

[a] recovery out of range (75-125%), standards not included in calibration curve; MDL = method detection limit; MQL = method quantitation limit; N = number of samples; %RSD = relative standard deviation

Table A.4 Se K-edge energies (obtained from maxima of normalized 1st derivative XANES plots) for reference materials and treatment samples. Linear combination fitting (LCF) of the XANES region for the treatment media are included.

sample	location	time (h)	energy (eV)			LCF results (%)		
			peak 1	peak 2	peak 3	Se(VI)	Se(IV)	Se(0)
Na_2SeO_4	bulk material	-	12666	-	-	-	-	-
Na_2SeO_3	bulk material	-	12663	-	-	-	-	-
Se^0 (grey)	bulk material	-	12658	-	-	-	-	-
Se^0 (red)	bulk material	-	12658	-	-	-	-	-
Cu_2Se	bulk material	-	12658	-	-	-	-	-
ZnSe	bulk material	-	12659	-	-	-	-	-
SeS_2	bulk material	-	12658	-	-	-	-	-
GI	spot	6	12658	12663	-	1.3	24.7	74.0
	map(1)	6	12658	12663	-	0.0	20.5	79.5
	map(2)	6	12658	12662	-	4.1	35.6	60.3
	map(3)	6	12658	12663	-	3.3	31.1	65.6
	spot	72	12658	-	-	0.0	1.5	98.5
	spot	120	12658	-	-	2.1	10.4	87.5
	map(1)	120	12658	-	-	0.0	7.3	92.7
	map(2)	120	12658	-	-	0.0	4.0	96.0
OC	spot	6	12666	-	-	93.4	6.6	0.0
	map(1)	6	12666	12663	-	100.0	0.0	0.0
	spot	72	12666	12663	-	75.1	9.9	15.0
	spot	120	12666	-	-	88.2	11.8	0.0
	map(1)	120	12666	12663	12658	16.7	12.1	71.3
GI-OC	spot(Fe rich)	6	12658	12663	-	1.3	17.7	81.0
	spot(Fe rich)	72	12658	-	-	0.0	13.1	86.9
	spot(Fe rich)	120	12658	-	-	1.1	8.5	90.4
	spot(OC rich)	6	12658	12663	-	4.5	38.2	57.2
	spot(OC rich)	72	12658	-	-	0.3	8.2	91.6
	spot(OC rich)	120	12658	12663	-	5.2	22.3	72.5

GI = granular Fe^0; OC = organic carbon; GI-OC = mixture of Fe^0 and organic carbon

Appendix B:

Summary of Data Presented in Chapter 3

Table B.1 Summary of general chemistry, anion, nutrient, and total and dissolved organic carbon concentrations from sediment resuspension tests under oxic conditions.

sample	time (h)	pH	Eh (mV)	filtered concentration (mg L^{-1})						unfiltered (mg L^{-1})		
				Alk ($CaCO_3$)	Cl	NO_3	SO_4	NH_3+ NH_4	DOC	TKN	TP	TOC
MDL	-	-	-	-	-	-	-	0.04	0.2	0.05	0.02	0.2
DI	-	-	-	-	-	-	-	0.04	< 0.2	1.6	0.13	0.2
input	0	7.5	640	230	28	6.3	35	0.08	3.8	1.8	0.06	3.7
A	0.5	7.2	675	220	36	3.5	48	0.70	10	17	1.1	340
	6	7.8	660	190	34	4.3	69	0.60	26	16	0.99	430
	24	7.5	665	n/a	35	4.5	98	1.2	38	440	25	500
B	0.5	6.5	665	38	36	4.3	33	2.3	13	64	11	20
	6	6.4	660	n/a	38	5.2	46	1.9	9.1	410	67	81
	24	6.6	675	n/a	36	4.7	54	3.3	5.8	320	55	220
C	0.5	7.3	650	200	42	3.5	30	3.8	5.3	880	120	23
	6	7.1	640	180	42	n/d	35	4.0	23	690	94	20
	24	7.3	575	200	41	n/d	31	5.2	9.5	870	130	15
D	0.5	6.5	495	120	36	4.1	28	2.5	4.1	440	130	5.8
	6	6.8	675	16	39	4.7	38	2.4	6.0	340	100	24
	24	6.7	590	22	38	5.3	88	2.1	41	360	120	75
E	0.5	6.7	275	120	36	3.5	31	1.9	3.6	270	110	6.9
	6	6.9	690	21	36	3.9	38	1.9	5.5	190	78	68
	24	6.8	460	120	36	n/d	32	2.4	4.9	310	110	7.0
F	0.5	6.7	365	160	30	3.3	30	5.2	6.2	140	57	18
	6	6.7	655	160	30	n/d	29	4.8	8.5	130	45	85
	24	7.1	435	21	30	4.5	130	4.8	6.2	140	55	49
G	0.5	6.7	320	160	36	n/d	32	5.0	5.5	140	54	160
	6	6.7	650	100	36	5.1	32	4.9	4.6	130	53	24
	24	6.8	690	51	35	5.7	18	4.4	7.8	160	54	630
H	0.5	6.8	470	230	31	4.0	28	13.2	5.1	360	100	7.0
	6	6.7	265	140	33	n/d	28	11.1	8.8	170	78	15
	24	6.9	270	62	34	n/d	30	11.6	5.4	130	63	32
I	0.5	7.0	275	34	29	4.4	34	3.6	4.8	150	36	20
	6	7.0	285	170	30	n/d	41	3.6	3.8	130	34	43
	24	7.1	315	300	30	1.1	38	4.0	5.3	240	45	81
J	0.5	7.0	330	170	36	4.2	43	1.3	6.8	260	11	160
	6	6.9	670	150	36	5.8	44	1.4	9.6	410	18	350
	24	7.4	600	170	38	7.1	54	1.0	10.3	430	20	250

n/a = not analyzed; n/d = not detected; Alk = alkalinity (mg L^{-1} $CaCO_3$); DOC = dissolved organic carbon; TOC = total organic carbon; TKN = total Kjeldahl nitrogen; TP = total phosphorus; MDL = method detection limit; DI = deionized water

Table B.2 Summary of general chemistry, anion, nutrient, and total and dissolved organic carbon concentrations from sediment resuspension tests under anoxic conditions.

sample	time (h)	pH	Eh (mV)	filtered concentration (mg L^{-1})						unfiltered (mg L^{-1})		
				Alk ($CaCO_3$)	Cl	NO_3	SO_4	NH_3+ NH_4	DOC	TKN	TP	TOC
A	0.5	7.3	195	180	35	2.6	45	1.6	83	510	45	360
	6	7.5	165	290	31	n/d	50	1.7	24	310	26	120
	24	7.9	15	380	35	n/d	60	1.4	11	430	35	390
B	0.5	6.8	155	80	37	4.9	32	4.0	20	490	86	31
	6	6.7	140	89	35	3.7	34	4.4	1.8	290	63	77
	24	6.8	125	51	43	n/d	46	3.9	4.0	240	54	190
C	0.5	7.7	250	170	37	n/d	33	4.0	8.7	190	40	57
	6	7.8	195	140	42	n/d	38	4.1	7.6	220	35	130
	24	7.7	105	120	36	n/d	37	4.5	3.6	160	35	32
D	0.5	6.9	155	71	46	n/d	33	2.3	11	76	43	9.9
	6	6.8	95	100	36	n/d	40	2.9	5.2	62	29	4.3
	24	7.1	130	72	38	n/d	36	2.3	6.8	100	46	5.8
E	0.5	7.1	135	130	33	n/d	33	5.9	6.9	110	36	< 2
	6	7.0	-65	120	35	300	30	4.4	8.4	70	28	30
	24	6.6	-150	49	31	n/d	47	5.2	6.6	78	41	28
F	0.5	7.0	70	130	32	n/d	40	3.1	4.3	39	13	23
	6	7.0	-175	120	30	n/d	36	2.9	5.5	29	8.4	56
	24	7.2	-255	100	29	n/d	43	6.5	6.4	58	16	< 10
G	0.5	6.8	160	85	36	n/d	57	5.6	3.2	120	36	5.4
	6	6.9	75	80	34	6.8	38	6.4	3.0	460	110	4.7
	24	7.1	15	46	37	n/d	34	5.1	6.6	260	67	7.5
H	0.5	6.8	130	93	37	n/d	38	14	3.5	310	96	4.8
	6	6.7	125	110	37	4.6	38	16	4.8	370	140	8.0
	24	7.3	-255	38	37	n/d	36	15	11	360	130	60
I	0.5	7.1	55	140	31	n/d	52	4.6	6.5	280	48	5.4
	6	7.0	-55	56	32	5.6	51	3.1	3.6	110	19	4.7
	24	7.0	-155	32	32	n/d	68	4.9	5.0	300	49	4.6
J	0.5	6.8	110	110	37	2.6	84	1.5	4.2	500	24	27
	6	6.6	-100	57	40	4.6	99	0.8	6.5	490	21	47
	24	7.0	-205	36	38	n/d	109	1.1	8.0	710	33	38

n/a = not analyzed; n/d = not detected; Alk = alkalinity (mg L^{-1} $CaCO_3$); DOC = dissolved organic carbon; TOC = total organic carbon; TKN = total Kjeldahl nitrogen; TP = total phosphorus

Table B.3 Summary of general chemistry, anion, nutrient, and total and dissolved organic carbon concentrations from sediment reoxidation tests.

sample	time (h)	pH	Eh (mV)	filtered concentration (mg L^{-1})						unfiltered (mg L^{-1})		
				Alk ($CaCO_3$)	Cl	NO_3	SO_4	NH_3+ NH_4	DOC	TKN	TP	TOC
A	0.5	7.31	595	200	33	4.4	42	5.2	6.8	38	45	150
	6	7.28	525	230	32	3.8	44	5.3	6.6	37	47	9.2
	24	7.54	685	210	36	5.5	54	5.3	8.8	39	53	98
B	0.5	6.57	350	120	36	5.6	30	4.1	3.8	280	32	12
	6	6.44	315	150	35	5.8	33	4.8	3.5	190	25	9.2
	24	6.31	545	100	38	6.6	36	3.3	5.2	150	23	43
C	0.5	7.2	390	190	38	4.8	34	4.1	4.7	96	16	20
	6	7.15	570	200	39	5.0	33	4.0	3.8	440	57	11
	24	7.23	395	190	42	5.0	42	4.2	5.5	640	87	29
D	0.5	6.65	410	150	36	4.9	35	2.5	2.5	190	66	8.6
	6	6.61	460	130	37	4.4	33	0.9	2.9	190	65	< 6
	24	6.52	360	110	37	5.1	41	1.1	3.3	450	150	< 6
E	0.5	6.87	335	170	33	5.0	30	1.6	1.8	310	66	< 6
	6	6.79	335	140	34	3.6	32	1.6	1.9	290	64	8.4
	24	6.7	300	140	35	4.3	43	2.0	4.5	530	140	14
F	0.5	6.82	255	n/a	29	3.2	31	1.9	3.4	190	40	6.9
	6	6.79	195	210	29	5.8	33	5.8	< 0.6	250	71	6.4
	24	6.69	445	83	34	2.2	48	9.0	10	300	63	12
G	0.5	6.71	430	150	35	5.2	32	4.9	2.1	200	48	18
	6	6.63	380	150	35	5.0	30	5.4	9.6	200	49	8.3
	24	6.43	285	110	36	3.7	39	6.6	3.6	260	74	21
H	0.5	6.78	195	170	34	5.3	29	11	3.6	200	63	< 2
	6	6.69	215	120	35	6.5	30	12	3.6	220	74	3.6
	24	6.5	320	130	44	5.5	41	16	19	270	150	27
I	0.5	7.01	235	160	31	n/d	39	3.9	3.5	260	36	7.4
	6	6.93	215	160	31	3.9	39	3.8	4.9	300	39	8.0
	24	6.87	310	140	34	4.2	66	5.6	14	410	55	14
J	0.5	7	475	160	38	5.2	45	2.2	5.6	460	22	28
	6	6.92	485	160	37	5.3	47	1.7	3.8	440	23	28
	24	7.07	430	130	39	5.3	53	1.6	0.8	710	41	84

n/a = not analyzed; n/d = not detected; Alk = alkalinity (mg L^{-1} $CaCO_3$); DOC = dissolved organic carbon; TOC = total organic carbon; TKN = total Kjeldahl nitrogen; TP = total phosphorus

Table B.4 Summary of metal and cation concentrations from sediment resuspension tests under oxic conditions.

sample	sediment mass (g)	time (h)	concentration (mg L^{-1})				μg L^{-1}					ng L^{-1}
			Ca	K	Mg	Na	Al	Fe	Mn	Pb	Se	Hg
input	-	0	39	1.6	15	13	5.0	50	1	1.1	1.1	7
A	58	0.5	36	1.3	11	79	61	14	13	5.3	1.1	900
	57	6	14	1.1	6	80	410	74	0	36	3.1	7100
	58	24	12	1.1	5	93	970	190	1	55	7.9	5100
B	41	0.5	18	2.9	6	24	40	38	83	6.3	2.0	1600
	41	6	10	2.4	4	40	290	94	4	9.2	1.1	7200
	40	24	11	4.5	4	27	37	16	30	4.4	1.1	6700
C	70	0.5	50	1.0	21	12	36	51	170	3.2	1.8	170
	70	6	45	1.0	19	12	18	13	210	3.6	1.2	200
	70	24	52	1.1	23	14	570	320	220	14	2.3	180
D	45	0.5	31	1.7	11	18	1	490	170	46	2.7	1600
	45	6	15	1.5	5	18	54	65	50	20	1.6	1300
	52	24	19	2.0	6	33	190	200	67	31	4.4	3900
E	40	0.5	38	1.5	13	17	12	1200	210	6.6	2.2	340
	40	6	16	1.4	5	18	120	180	29	29	2.1	2800
	40	24	34	1.8	12	20	0	1300	230	5.1	1.3	400
F	44	0.5	40	1.1	12	14	400	2500	360	4.0	0.0	71
	44	6	43	1.6	14	15	430	5400	510	4.2	0.9	62
	44	24	18	2.1	7	44	620	640	7	7.8	0.7	370
G	40	0.5	40	1.4	17	16	250	3700	400	4.4	0.0	230
	40	6	32	2.6	15	16	220	1100	350	4.3	1.7	310
	40	24	21	2.2	10	34	310	130	19	5.7	0.0	1100
H	41	0.5	46	1.7	15	16	210	5200	830	3.8	0.1	110
	41	6	35	3.2	14	19	190	8400	890	3.5	0.8	160
	40	24	30	1.9	11	19	190	5200	790	7.9	0.0	190
I	40	0.5	41	1.5	15	34	160	570	180	3.6	2.3	130
	40	6	32	2.1	12	37	170	86	110	4.2	0.5	190
	40	24	40	1.8	15	38	140	160	200	3.6	2.7	140
J	40	0.5	47	1.4	22	17	150	49	41	4.7	1.1	440
	40	6	47	2.0	22	17	140	27	33	4.7	1.8	550
	42	24	32	1.1	16	20	130	61	4	3.5	3.5	380

Table B.5 Summary of metal and cation concentrations from sediment resuspension tests under anoxic conditions.

sample	sediment mass (g)	time (h)	concentration (mg L^{-1})				μg L^{-1}					ng L^{-1}
			Ca	K	Mg	Na	Al	Fe	Mn	Pb	Se	Hg
input	-	0	39	1.6	15	13	5.0	50	1	2.6	1.1	7
A	41	0.5	43	2.8	13	58	43	43	14	5.2	2.1	300
	40	6	38	1.3	11	60	5	15	10	6.2	2.2	520
	40	24	28	1.5	8	62	140	38	9	13	5.0	950
B	40	0.5	28	3.5	12	22	13	4600	220	4.0	3.5	440
	41	6	27	3.5	12	17	19	4400	200	4.2	2.1	410
	40	24	20	3.8	8	23	47	1800	140	6.3	1.4	860
C	40	0.5	42	0.9	20	13	35	440	160	4.2	1.8	410
	40	6	42	1.3	20	18	34	59	150	5.2	4.0	220
	42	24	32	1.5	12	19	16	3500	220	8.9	1.4	320
D	40	0.5	36	1.1	17	19	46	80	110	5.1	0.5	260
	40	6	30	1.7	12	19	34	3500	210	15	1.1	1100
	40	24	24	1.8	8	24	70	1600	150	24	2.8	1200
E	40	0.5	38	1.1	12	16	23	2000	290	6.2	0.5	720
	40	6	36	1.1	12	17	43	2000	270	9.3	1.1	760
	41	24	73	2.4	16	22	80	23000	1300	5.7	3.0	1200
F	40	0.5	41	12	14	22	130	9200	460	4.3	1.5	120
	40	6	39	1.3	13	17	99	8500	440	4.2	4.3	120
	41	24	33	7.6	11	22	150	5500	350	3.7	4.3	100
G	41	0.5	32	1.5	14	22	46	4100	360	4.6	1.6	350
	40	6	27	1.8	12	16	350	2800	330	16	1.1	720
	40	24	19	1.5	9	21	130	670	190	9.6	0.9	1100
H	40	0.5	34	2.1	11	20	90	12000	840	4.8	3.9	150
	41	6	33	2.0	11	20	72	10000	800	7.6	3.2	190
	40	24	18	4.7	6	27	440	2500	310	11	2.3	490
I	40	0.5	37	1.8	14	37	44	2600	190	3.7	2.0	140
	41	6	36	1.7	13	36	57	2700	200	7.0	2.3	100
	40	24	26	1.7	10	42	180	340	96	4.9	3.5	1300
J	40	0.5	46	1.3	20	18	61	34	27	3.9	0.0	510
	41	6	45	1.8	19	19	73	41	25	4.7	0.5	370
	41	24	35	1.5	15	21	85	68	21	2.6	0.4	190

Table B.6 Summary of metal and cation concentrations from sediment reoxidation tests.

sample	sediment mass (g)	time (h)	concentration (mg L^{-1})				μg L^{-1}					ng L^{-1}
			Ca	K	Mg	Na	Al	Fe	Mn	Pb	Se	Hg
input	-	0										
A	41	2	45	1.3	14	60	30	38	15	6.4	1.6	100
	40	6	44	1.5	14	60	21	17	13	4.7	3.0	180
	40	24	36	1.4	11	74	83	47	8	11	2.4	350
B	41	2	30	3.1	11	16	5	1100	170	3.9	1.7	240
	41	6	29	3.1	10	16	7	2100	210	4.4	3.7	140
	40	24	28	3.5	10	18	3	555	200	4.4	1.4	390
C	41	2	52	1.0	21	13	10	41200	160	4.0	1.3	81
	40	6	58	1.1	27	14	10	46000	170	4.2	0.5	97
	38	24	51	1.5	20	13	74	90000	140	9.9	1.8	66
D	41	2	40	1.7	12	18	1	o/r	240	5.2	0.9	53
	40	6	37	1.6	11	19	1	o/r	220	4.8	0.8	110
	40	24	36	2.2	11	19	13	o/r	240	12	2.0	170
E	41	2	48	1.0	12	13	4	o/r	310	5.0	0.5	340
	41	6	44	1.4	11	13	7	o/r	270	5.4	1.4	480
	37	24	44	1.2	11	14	12	59000	290	5.9	0.5	160
F	41	2	45	2.6	12	15	700	3300	510	3.5	0.0	44
	41	6	47	2.7	13	14	390	2000	440	3.6	0.0	56
	40	24	37	2.8	11	17	400	650	440	3.8	0.0	56
G	41	2	39	2.8	14	16	390	2200	440	3.6	1.4	57
	41	6	37	2.8	13	16	410	1700	430	4.8	3.7	130
	41	24	35	3.0	13	18	410	340	430	4.3	1.8	54
H	40	2	43	3.3	12	18	390	9100	1100	3.5	1.4	91
	40	6	39	3.2	11	17	400	6100	970	3.8	2.6	32
	36	24	36	4.0	9	20	500	1100	860	4.9	0.7	27
I	40	2	41	3.1	12	33	380	550	210	3.8	0.4	20
	41	6	41	3.1	12	34	410	280	200	5.3	1.0	120
	40	24	38	3.3	12	38	410	78	170	4.1	2.4	58
J	41	2	48	3.2	21	17	370	52	61	4.5	0.5	58
	40	6	49	3.1	21	17	380	32	46	4.6	0.3	420
	41	24	49	3.2	21	18	410	26	39	2.6	2.9	770

o/r = over range

Table B.7 Summary of QA/QC from the oxic resuspension tests obtained by HR-ICP-MS.

label	actual Hg concentration (ng L^{-1})	reported Hg concentration (ng L^{-1})	% recovery	N	%RSD
MDL	-	4	-	-	-
MQL	-	22	-	-	-
blank	-	5	-	9	14
Std1	10	12	122	2	4
Std2	50	52	104	2	11
Std3	100	101	101	2	8
Std4	500	490	98	2	7
Std5	1000	1005	100	2	9

MDL = method detection limit; MQL = method quantitation limit; N = number of samples; %RSD = relative standard deviation (%)

Table B.8 Summary of QA/QC from the anoxic resuspension tests obtained by HR-ICP-MS.

label	actual Hg concentration (ng L^{-1})	reported Hg concentration (ng L^{-1})	% recovery	N	%RSD
MDL	-	8	-	-	-
MQL	-	31	-	-	-
blank	-	11	-	9	24
Std1	10	10	122	2	11
Std2	50	50	104	2	4
Std3	100	100	101	2	8
Std4	500	500	98	2	6
Std5	1000	1000	100	2	10

MDL = method detection limit; MQL = method quantitation limit; N = number of samples; %RSD = relative standard deviation (%)

Table B.9 Summary of QA/QC from the sediment reoxidation tests obtained by HR-ICP-MS.

date	label	actual Hg concentration (ng L^{-1})	reported Hg concentration (ng L^{-1})	% recovery	N	%RSD
05/01/2008	MDL	-	4	-	-	-
	MQL	-	24	-	-	-
	blank	-	17	-	3	8
	Std1	10	20	204	1	-
	Std2	50	56	113	1	-
	Std3	100	80	80	1	-
	Std4	500	503	101	1	-
05/02/2008	MDL	-	2	-	-	-
	MQL	-	16	-	-	-
	blank	-	17	-	7	8
	Std1	10	9	92	2	11
	Std2	50	50	101	2	1
	Std3	100	100	100	2	0
	Std4	500	500	100	2	2
05/05/2008	MDL	-	2	-	-	-
	MQL	-	16	-	-	-
	blank	-	2	-	6	19
	Std1	5	6	110	2	6
	Std2	10	10	96	2	0
	Std3	50	50	100	2	7
	Std4	200	100	50	2	7
	Std5	500	500	100	2	7
05/06/2008	MDL	-	2	-	-	-
	MQL	-	13	-	-	-
	blank	-	7	-	7	8
	Std1	5	11	215	2	6
	Std2	10	15	149	2	0
	Std3	50	43	87	2	7
	Std4	200	94	47	2	7
	Std5	500	502	100	2	7

MDL = method detection limit; MQL = method quantitation limit; N = number of samples; %RSD = relative standard deviation (%)

Table B.10 Summary of synthetic precipitation leaching procedure (SPLP) analyses performed by Brooks Rand Labs (Seattle, WA) for total Hg and total suspended solids.

sample	EPA method	analyte	result	MDL	MRL	units
A	1631	Hg	740	15	40	ng L^{-1}
B	1631	Hg	690	15	40	ng L^{-1}
C	1631	Hg	210	15	40	ng L^{-1}
D	1631	Hg	1100	15	40	ng L^{-1}
E	1631	Hg	1500	15	40	ng L^{-1}
F	1631	Hg	74	3.0	8.0	ng L^{-1}
G	1631	Hg	350	15	40	ng L^{-1}
H	1631	Hg	170	3.0	8.0	ng L^{-1}
I	1631	Hg	82	15	40	ng L^{-1}
J	1631	Hg	300	15	40	ng L^{-1}
A	160.3	% TS	15	0.10	0.33	%
B	160.3	% TS	31	0.10	0.33	%
C	160.3	% TS	20	0.10	0.33	%
D	160.3	% TS	37	0.10	0.33	%
E	160.3	% TS	28	0.10	0.33	%
F	160.3	% TS	42	0.10	0.33	%
G	160.3	% TS	26	0.10	0.33	%
H	160.3	% TS	26	0.10	0.33	%
I	160.3	% TS	25	0.10	0.33	%
J	160.3	% TS	19	0.10	0.33	%

MDL = method detection limit; MRL = method reporting limit

Table B.11 Summary of synthetic precipitation leaching procedure (SPLP) analyses performed by Brooks Rand Labs (Seattle, WA) for total element concentrations.

sample	EPA method	analyte	result	MDL	MRL	units
A	1638 modified	Al 27	190	0.30	1.0	$\mu g\ L^{-1}$
	1638 modified	Ca 44	16000	6.1	30	$\mu g\ L^{-1}$
	1638 modified	Cd 114	0.054	0.004	0.010	$\mu g\ L^{-1}$
	1638 modified	Cu 63	14	0.04	0.20	$\mu g\ L^{-1}$
	1638 modified	Fe 57	82	1.4	5.1	$\mu g\ L^{-1}$
	1638 modified	K 39	610	1.3	4.0	$\mu g\ L^{-1}$
	1638 modified	Mg 24	5200	0.61	3.0	$\mu g\ L^{-1}$
	1638 modified	Mn 55	6.2	0.010	0.051	$\mu g\ L^{-1}$
	1638 modified	Na 23	48000	110	760	$\mu g\ L^{-1}$
	1638 modified	Pb 208	4.3	0.082	0.24	$\mu g\ L^{-1}$
B	1638 modified	Al 27	170	0.61	2.0	$\mu g\ L^{-1}$
	1638 modified	Ca 44	5300	12	61	$\mu g\ L^{-1}$
	1638 modified	Cd 114	0.038	0.008	0.020	$\mu g\ L^{-1}$
	1638 modified	Cu 63	1.7	0.34	1.1	$\mu g\ L^{-1}$
	1638 modified	Fe 57	140	2.8	10	$\mu g\ L^{-1}$
	1638 modified	K 39	1600	2.6	8.1	$\mu g\ L^{-1}$
	1638 modified	Mg 24	2200	1.21	6.1	$\mu g\ L^{-1}$
	1638 modified	Mn 55	110	0.020	0.10	$\mu g\ L^{-1}$
	1638 modified	Na 23	3600	2.1	15	$\mu g\ L^{-1}$
	1638 modified	Pb 208	1.2	0.16	0.49	$\mu g\ L^{-1}$
C	1638 modified	Al 27	100	0.30	1.0	$\mu g\ L^{-1}$
	1638 modified	Ca 44	14000	6.1	30	$\mu g\ L^{-1}$
	1638 modified	Cd 114	0.022	0.004	0.010	$\mu g\ L^{-1}$
	1638 modified	Cu 63	6.0	0.17	0.53	$\mu g\ L^{-1}$
	1638 modified	Fe 57	59	1.4	5.1	$\mu g\ L^{-1}$
	1638 modified	K 39	310	1.3	4.0	$\mu g\ L^{-1}$
	1638 modified	Mg 24	6300	0.61	3.0	$\mu g\ L^{-1}$
	1638 modified	Mn 55	50	0.010	0.051	$\mu g\ L^{-1}$
	1638 modified	Na 23	2500	2.1	15	$\mu g\ L^{-1}$
	1638 modified	Pb 208	1.1	0.082	0.24	$\mu g\ L^{-1}$
D	1638 modified	Al 27	250	0.61	2.0	$\mu g\ L^{-1}$
	1638 modified	Ca 44	7800	12	61	$\mu g\ L^{-1}$
	1638 modified	Cd 114	0.18	0.008	0.020	$\mu g\ L^{-1}$

MDL = method detection limit; MRL = method reporting limit

Table B.11 continued Summary of synthetic precipitation leaching procedure (SPLP) analyses performed by Brooks Rand Labs (Seattle, WA) for total element concentrations.

sample	EPA method	analyte	result	MDL	MRL	units
D	1638 modified	Cu 63	23	0.34	1.1	$\mu g\ L^{-1}$
	1638 modified	Fe 57	160	2.8	10	$\mu g\ L^{-1}$
	1638 modified	K 39	770	2.6	8.1	$\mu g\ L^{-1}$
	1638 modified	Mg 24	2700	1.2	6.1	$\mu g\ L^{-1}$
	1638 modified	Mn 55	160	0.020	0.10	$\mu g\ L^{-1}$
	1638 modified	Na 23	4200	2.1	15	$\mu g\ L^{-1}$
	1638 modified	Pb 208	6.7	0.16	0.49	$\mu g\ L^{-1}$
E	1638 modified	Al 27	140	0.61	2.0	$\mu g\ L^{-1}$
	1638 modified	Ca 44	9700	12	61	$\mu g\ L^{-1}$
	1638 modified	Cd 114	0.051	0.008	0.020	$\mu g\ L^{-1}$
	1638 modified	Cu 63	9.4	0.34	1.1	$\mu g\ L^{-1}$
	1638 modified	Fe 57	120	2.8	10	$\mu g\ L^{-1}$
	1638 modified	K 39	390	2.6	8.1	$\mu g\ L^{-1}$
	1638 modified	Mg 24	2700	1.2	6.1	$\mu g\ L^{-1}$
	1638 modified	Mn 55	170	0.020	0.10	$\mu g\ L^{-1}$
	1638 modified	Na 23	2900	2.1	15	$\mu g\ L^{-1}$
	1638 modified	Pb 208	2.7	0.16	0.49	$\mu g\ L^{-1}$
F	1638 modified	Al 27	46	0.30	1.0	$\mu g\ L^{-1}$
	1638 modified	Ca 44	11000	6.1	30	$\mu g\ L^{-1}$
	1638 modified	Cd 114	0.033	0.004	0.010	$\mu g\ L^{-1}$
	1638 modified	Cu 63	2.3	0.04	0.20	$\mu g\ L^{-1}$
	1638 modified	Fe 57	65	1.4	5.1	$\mu g\ L^{-1}$
	1638 modified	K 39	390	1.3	4.0	$\mu g\ L^{-1}$
	1638 modified	Mg 24	3600	0.61	3.0	$\mu g\ L^{-1}$
	1638 modified	Mn 55	280	0.010	0.051	$\mu g\ L^{-1}$
	1638 modified	Na 23	2500	2.1	15	$\mu g\ L^{-1}$
G	1638 modified	Al 27	100	0.30	1.0	$\mu g\ L^{-1}$
	1638 modified	Ca 44	9800	6.1	30	$\mu g\ L^{-1}$
	1638 modified	Cd 114	0.039	0.004	0.010	$\mu g\ L^{-1}$
	1638 modified	Cu 63	4.2	0.17	0.53	$\mu g\ L^{-1}$
	1638 modified	Fe 57	72	1.4	5.1	$\mu g\ L^{-1}$
	1638 modified	K 39	490	1.3	4.0	$\mu g\ L^{-1}$
	1638 modified	Mg 24	4300	0.61	3.0	$\mu g\ L^{-1}$

MDL = method detection limit; MRL = method reporting limit

Table B.11 continued Summary of synthetic precipitation leaching procedure (SPLP) analyses performed by Brooks Rand Labs (Seattle, WA) for total element concentrations.

sample	EPA method	analyte	result	MDL	MRL	units
G	1638 modified	Mn 55	280	0.010	0.051	$\mu g\ L^{-1}$
	1638 modified	Na 23	4600	2.1	15	$\mu g\ L^{-1}$
	1638 modified	Pb 208	0.80	0.082	0.24	$\mu g\ L^{-1}$
H	1638 modified	Al 27	270	0.30	1.0	$\mu g\ L^{-1}$
	1638 modified	Ca 44	5900	6.1	30	$\mu g\ L^{-1}$
	1638 modified	Cd 114	0.058	0.004	0.010	$\mu g\ L^{-1}$
	1638 modified	Cu 63	6.2	0.04	0.20	$\mu g\ L^{-1}$
	1638 modified	Fe 57	160	1.4	5.1	$\mu g\ L^{-1}$
	1638 modified	K 39	460	1.3	4.0	$\mu g\ L^{-1}$
	1638 modified	Mg 24	1500	0.61	3.0	$\mu g\ L^{-1}$
	1638 modified	Mn 55	280	0.010	0.051	$\mu g\ L^{-1}$
	1638 modified	Na 23	2000	2.1	15	$\mu g\ L^{-1}$
	1638 modified	Pb 208	1.6	0.082	0.24	$\mu g\ L^{-1}$
I	1638 modified	Al 27	160	0.30	1.0	$\mu g\ L^{-1}$
	1638 modified	Ca 44	9500	6.1	30	$\mu g\ L^{-1}$
	1638 modified	Cd 114	0.027	0.004	0.010	$\mu g\ L^{-1}$
	1638 modified	Cu 63	3.8	0.04	0.20	$\mu g\ L^{-1}$
	1638 modified	Fe 57	140	1.4	5.1	$\mu g\ L^{-1}$
	1638 modified	K 39	490	1.3	4.0	$\mu g\ L^{-1}$
	1638 modified	Mg 24	3300	0.61	3.0	$\mu g\ L^{-1}$
	1638 modified	Mn 55	130	0.010	0.051	$\mu g\ L^{-1}$
	1638 modified	Na 23	14000	110	760	$\mu g\ L^{-1}$
	1638 modified	Pb 208	1.0	0.082	0.24	$\mu g\ L^{-2}$
J	1638 modified	Al 27	68	0.30	1.0	$\mu g\ L^{-1}$
	1638 modified	Ca 44	14000	6.1	30	$\mu g\ L^{-1}$
	1638 modified	Cd 114	0.014	0.004	0.010	$\mu g\ L^{-1}$
	1638 modified	Cu 63	1.8	0.04	0.20	$\mu g\ L^{-1}$
	1638 modified	Fe 57	36	1.4	5.1	$\mu g\ L^{-1}$
	1638 modified	K 39	130	1.3	4.0	$\mu g\ L^{-1}$
	1638 modified	Mg 24	5900	0.61	3.0	$\mu g\ L^{-1}$
	1638 modified	Mn 55	8.0	0.010	0.051	$\mu g\ L^{-1}$
	1638 modified	Na 23	2400	2.1	15	$\mu g\ L^{-1}$

MDL = method detection limit; MRL = method reporting limit

Table B.12 Quality control/quality assurance (QA/QC) analyses reported by Brooks Rand Labs (Seattle, WA) from the SPLP analyses.

sample	analyte	sample value	spike value	result	units	% recovery	% recovery limits	duplicate RPD	RPD limits
duplicate	Hg	1460		1530	ng L^{-1}	-	-	5	24
duplicate	Hg	691		649	ng L^{-1}	-	-	6	24
matrix spike	Hg	691	2530	3150	ng L^{-1}	97	71-125		
matrix spike duplicate	Hg	691.0	2530	3150	ng L^{-1}	97	71-125	0.06	24
duplicate	% TS	30.7	-	28.6	%			7	15
duplicate	Al 27	169	-	164	µg L^{-1}	-	-	3	25
	Ca 44	5340	-	4450	µg L^{-1}	-	-	18	25
	Cd 114	0.038	-	0.029	µg L^{-1}	-	-	27	25
	Cu 63	1.73	-	1.71	µg L^{-1}	-	-	1	25
	Fe 57	139	-	134	µg L^{-1}	-	-	4	25
	K 39	1580	-	1310	µg L^{-1}	-	-	19	25
	Mg 24	2220	-	1820	µg L^{-1}	-	-	20	25
	Mn 55	110	-	90.5	µg L^{-1}	-	-	19	25
	Pb 208	1.24	-	1.22	µg L^{-1}	-	-	2	25
duplicate	Al 27	135	-	146	µg L^{-1}	-	-	8	25
	Ca 44	9730	-	10200	µg L^{-1}	-	-	4	25
	Cd 114	0.051	-	0.053	µg L^{-1}	-	-	4	25
	Cu 63	9.35	-	10.2	µg L^{-1}	-	-	8	25
	Fe 57	119	-	136	µg L^{-1}	-	-	13	25
	K 39	391	-	380	µg L^{-1}	-	-	3	25
	Mg 24	2700	-	2620	µg L^{-1}	-	-	3	25
	Mn 55	166	-	176	µg L^{-1}	-	-	6	25
	Pb 208	2.72	-	3.01	µg L^{-1}	-	-	10	25
matrix spike	Al 27	169	12100	11500	µg L^{-1}	93	71-125	-	-
	Ca 44	5340	50500	52200	µg L^{-1}	93	71-125	-	-
	Cd 114	0.038	0.202	0.218	µg L^{-1}	89	71-125	-	-
	Cu 63	1.73	50.5	49.0	µg L^{-1}	94	71-125	-	-
	Fe 57	139	8080	7830	µg L^{-1}	95	71-125	-	-
	K 39	1580	14100	15200	µg L^{-1}	96	71-125	-	-
	Mg 24	2220	24200	25400	µg L^{-1}	96	71-125	-	-
	Mn 55	110	1010	1070	µg L^{-1}	95	71-125	-	-
	Pb 208	1.24	50.5	46.9	µg L^{-1}	90	71-125	-	-
matrix spike	Al 27	135	12100	11900	µg L^{-1}	97	71-125	-	-
	Ca 44	9730	50590	55900	µg L^{-1}	91	71-125	-	-
	Cd 114	0.051	0.202	0.243	µg L^{-1}	95	71-125	-	-
	Cu 63	9.35	50.5	55.9	µg L^{-1}	92	71-125	-	-
	Fe 57	119	8090	7660	µg L^{-1}	93	71-125	-	-
	K 39	391	14190	13700	µg L^{-1}	94	71-125	-	-

Table B.12 continued Quality control/quality assurance (QA/QC) analyses reported by Brooks Rand Labs (Seattle, WA) from the SPLP analyses.

sample	analyte	sample value	spike value	result	units	% recovery	% recovery limits	duplicate RPD	RPD limits
matrix spike	Mg 24	2700	24290	26100	μg L^{-1}	96	71-125	-	-
	Mn 55	166	1010	1140	μg L^{-1}	97	71-125	-	-
	Pb 208	2.72	50.5	50.8	μg L^{-1}	95	71-125	-	-
matrix spike duplicate	Al 27	169	12100	11400	μg L^{-1}	93	71-125	-	-
	Ca 44	5340	50500	53600	μg L^{-1}	96	71-125	-	-
	Cd 114	0.038	0.202	0.212	μg L^{-1}	86	71-125	-	-
	Cu 63	1.73	50.5	49.8	μg L^{-1}	95	71-125	-	-
	Fe 57	139	8080	74.7	μg L^{-1}	91	71-125	-	-
	K 39	1580	14100	15000	μg L^{-1}	95	71-125	-	-
	Mg 24	2220	24200	25400	μg L^{-1}	96	71-125	-	-
	Mn 55	110	1010	1060	μg L^{-1}	94	71-125	-	-
	Pb 208	1.24	50.5	47.3	μg L^{-1}	91	71-125	-	-
matrix spike duplicate	Al 27	135	12100	12000	μg L^{-1}	98	71-125	-	-
	Ca 44	9730	50500	58100	μg L^{-1}	96	71-125	-	-
	Cd 114	0.051	0.202	0.237	μg L^{-1}	92	71-125	-	-
	Cu 63	9.35	50.5	54.2	μg L^{-1}	89	71-125	-	-
	Fe 57	119	8080	7770	μg L^{-1}	95	71-125	-	-
	K 39	391	14100	14000	μg L^{-1}	96	71-125	-	-
	Mg 24	2700	24200	26600	μg L^{-1}	98	71-125	-	-
	Mn 55	166	1010	1140	μg L^{-1}	96	71-125	-	-
	Pb 208	2.72	50.5	49.4	μg L^{-1}	92	71-125	-	-
post spike	Al 27	248	18200	17300	μg L^{-1}	94	71-125	-	-
	Ca 44	7770	75800	75500	μg L^{-1}	89	71-125	-	-
	Cd 114	0.177	0.303	0.442	μg L^{-1}	87	71-125	-	-
	Cu 63	22.8	75.8	87.5	μg L^{-1}	85	71-125	-	-
	Fe 57	162	12100	10800	μg L^{-1}	88	71-125	-	-
	K 39	766	21200	20400	μg L^{-1}	93	71-125	-	-
	Mg 24	2660	36400	36200	μg L^{-1}	92	71-125	-	-
	Mn 55	160	1520	1520	μg L^{-1}	90	71-125	-	-
	Pb 208	6.9	75.8	73.0	μg L^{-1}	87	71-125	-	-

RPD = relative percent difference

Table B.12 continued Quality control/quality assurance (QA/QC) analyses reported by Brooks Rand Labs (Seattle, WA) from the SPLP analyses.

sample	analyte	sample value	spike value	result	units	% recovery	% recovery limits	duplicate RPD	RPD limits
CRM (NIST 1643e)	Al 27		142	139	µg L^{-1}	98	71-125	-	-
	Ca 44		31500	29500	µg L^{-1}	94	71-125	-	-
	Cd 114		3.57	6.25	µg L^{-1}	95	71-125	-	-
	Cu 63		22.2	21.5	µg L^{-1}	97	71-125	-	-
	Fe 57		98.1	121	µg L^{-1}	124	71-125	-	-
	K 39		2030	1950	µg L^{-1}	96	71-125	-	-
	Mg 24		7480	7860	µg L^{-1}	105	71-125	-	-
	Mn 55		39.0	37.5	µg L^{-1}	96	71-125	-	-
	Pb 208		19.2	18.4	µg L^{-1}	96	71-125	-	-
duplicate	Na 23	3620	-	3170	µg L^{-1}	-	-	13	25
duplicate	Na 23	2900	-	3150	µg L^{-1}	-	-	8	25
matrix spike	Na 23	3620	10100	13700	µg L^{-1}	100	75-125	-	-
matrix spike duplicate	Na 23	3620	10100	13500	µg L^{-1}	98	75-125	2	25
CRM (NIST 1640)	Na 23	-	29700	30700	µg L^{-1}	103	75-125	-	-
CRM (NIST 1643e)	Na 23	-	21000	20100	µg L^{-1}	96	75-125	-	-

RPD = relative percent difference

Table B.13 Quality control/quality assurance (QA/QC) analyses reported by the Pacific Northwest National Laboratory - Battelle (Seattle, WA) from the sequential extraction analyses.

sample	fraction extracted (μg g^{-1}, dry weight)							% recovery
	F1	F2	F3	F4	F5	sum	total	
NIST 2711 r1	0.044	0.0027	0.60	3.7	-	4.4	6.0	73
NIST 2711 r2	0.039	0.0025	0.63	3.8	-	4.5	5.9	76
blank r1	0.00013	0.00034	-0.0055	0.0057	-	0.00067	-	-
blank r2	0.00011	0.0010	0.010	0.0027	-	0.014	-	-

Table B.14 Quality control/quality assurance (QA/QC) analyses reported by the Pacific Northwest National Laboratory - Battelle (Seattle, WA) from the sediment resuspension reoxidation analyses. Results are compared to data obtained in this thesis work where available.

sample	time (h)	type	matrix	Hg concentration (ng L^{-1})		% difference
				UW	PNNL	
LCW	0.0	-	filtered water	7	9	19
A	0.5	oxic	filtered water	900	790	13
	6	oxic	filtered water	7100	4900	37
B	0.5	oxic	filtered water	1600	1300	21
	6	oxic	filtered water	7200	8300	14
C	0.5	oxic	filtered water	170	120	34
	6	oxic	filtered water	200	160	22
D	0.5	oxic	filtered water	1600	3500	75
	6	oxic	filtered water	1300	1500	14
E	0.5	oxic	filtered water	340	350	3
	6	oxic	filtered water	2800	2800	0
A	0.5	anoxic	filtered water	300	440	38
	6	anoxic	filtered water	520	650	22
B	0.5	anoxic	filtered water	440	620	34
	6	anoxic	filtered water	410	530	26
C	0.5	anoxic	filtered water	410	430	5
	6	anoxic	filtered water	220	260	17
D	0.5	anoxic	filtered water	260	630	83
	6	anoxic	filtered water	1100	1400	24
E	0.5	anoxic	filtered water	720	1300	57
	6	anoxic	filtered water	770	1200	44
A	24	reoxidation	filtered water	350	790	77
B	24	reoxidation	filtered water	390	510	27
C	24	reoxidation	filtered water	66	270	121
D	24	reoxidation	filtered water	170	320	61
E	24	reoxidation	filtered water	160	810	134
F	24	reoxidation	filtered water	56	53	5
G	24	reoxidation	filtered water	54	360	148
H	24	reoxidation	filtered water	27	140	136
I	24	reoxidation	filtered water	58	180	103
J	24	reoxidation	filtered water	770	760	1
A (unfiltered)	6	oxic	water+sediment	-	95	
B (unfiltered)	6	oxic	water+sediment	-	170	
C (unfiltered)	6	oxic	water+sediment	-	86	
D (unfiltered)	6	oxic	water+sediment	-	450	
E (unfiltered)	6	oxic	water+sediment	-	460	
F (unfiltered)	6	oxic	water+sediment	-	440	
DI	-	deionized water	filtered water	0.39	-	

Table B.15 Summary of total element concentrations from sediment digestion analysis reported by SGS Lakefield Research (Lakefield, ON).

element	sediment concentration ($\mu g\ g^{-1}$)									
	A	B	C	D	E	F	G	H	I	J
Hg	120	79	81	340	240	40	140	51	22	51
Ag	0.50	0.42	0.94	0.89	0.94	0.63	0.73	0.86	0.72	0.13
Al	30000	37000	38000	45000	44000	46000	37000	45000	46000	14000
As	2.5	1.1	3.2	3.3	3.9	2.2	2.2	2.2	3.4	1.4
Ba	200	350	310	390	330	370	280	360	340	160
Be	1.2	1	1.3	1.4	1.3	1.2	1	1.4	1.3	0.45
Bi	0.10	0.09	0.30	0.87	0.48	0.095	0.17	0.14	0.17	0.09
Ca	15000	9000	11000	7200	7000	6700	5600	7300	7500	12000
Cd	1.4	0.37	1.2	2.5	2.9	1.0	1.1	1.1	2.4	0.43
Co	6.8	6.8	9.9	10	10	9.1	7.4	9.9	10	4.4
Cr	66	43	78	65	69	59	55	68	85	26
Cu	480	89	360	1100	660	270	380	260	270	90
Fe	16000	21000	20000	25000	26000	34000	19000	26000	30000	6900
K	6900	14000	9900	13000	12000	16000	9400	12000	12000	3600
Li	9	6.2	16	16	17	12	13	16	19	2.7
Mg	4800	4000	5700	5100	5500	4900	4400	5500	6100	3300
Mn	130	270	360	320	390	410	310	570	320	87
Mo	2	0.95	1.8	0.95	1.2	1.3	0.9	1	1.3	2.2
Na	5400	7700	5600	8200	7000	8200	5700	7500	7400	2300
Ni	21	22	33	27	28	26	23	25	28	13
Pb	310	180	210	640	480	160	230	170	160	82
Sb	1.3	1.8	1.7	2.2	1.9	1.1	1.4	1.1	1.7	0.55
Se	11	0.8	3.5	17	11	2.4	4	1.5	1.9	3.4
Sn	8	19	9.7	25	22	12	13	7.3	7.7	3.8
Sr	75	85	61	90	72	81	63	75	75	33
Ti	1800	3800	2200	2900	2900	4600	2800	2700	3300	820
Tl	0.18	0.23	0.31	0.34	0.35	0.31	0.25	0.32	0.34	0.08
U	5.6	1.7	3.4	2.2	2.5	2.1	2	3.1	2.9	6.7
V	110	69	65	79	77	86	67	73	85	39
Y	28	23	31	24	27	26	21	31	29	13
Zn	170	93	230	290	280	170	190	210	270	72

Table B.16 Summary of results obtained from particle size distribution analysis reported by SGS Lakefield Research (Lakefield, ON).

particle size (mm)	% passing									
	A	B	C	D	E	F	G	H	I	J
1700	100	100	100	100	100	100	100	100	100	100
300	82	66	96	91	95	80	95	99	98	72
75	65	37	79	72	78	58	82	83	89	57
30	37	23	52	49	55	39	59	60	65	32
20	25	17	38	38	42	30	45	47	50	22
15	19	13	30	31	33	24	36	37	40	17
10	12	8.5	19	21	22	17	24	25	26	10
6	5.9	6.1	9.6	12	11	9.4	13	13	13	5.2
4	3.4	2.6	5.7	7.4	6.9	6	7.8	7.8	7.9	3
2	1.5	1.1	2.6	3.4	3.2	2.8	3.5	3.5	3.7	1.6
1	0.6	0.5	1.1	1.5	1.4	1.2	1.5	1.6	1.6	0.6

Appendix C:

Summary of Data Presented in Chapter 4

Table C.1 Summary of general chemistry, mercury, and selenium concentrations from treatment experiments involving Connelly granular iron.

sample	time (h)	pH	Eh (mV)	concentration (mg L^{-1})		
				Alk ($CaCO_3$)	Hg	Se
INP(Hg)	3	8.2	30	55	3.8	0.09
	192	7.9	340	72	4.2	< 0.08
	384	8.2	380	71	9.4	< 0.08
CZVI(Hg)	3	7.9	-400	55	0.38	< 0.08
	6	7.9	-380	57	0.35	< 0.08
	12	7.9	-400	50	0.37	0.09
	24	7.8	-405	23	0.34	< 0.08
	48	7.6	-395	33	0.22	< 0.08
	48	7.7	-390	32	0.26	< 0.08
	48	7.6	-390	29	n/a	0.26
	96	7.6	-395	21	0.22	0.08
	192	7.7	-385	10	0.24	< 0.08
	192	7.5	-395	15	0.20	0.10
	192	7.5	-395	15	0.19	0.08
	384	7.8	-395	8	0.20	< 0.08
INP(Hg+Se)	3	8.1	-25	77	3.3	10
	192	8.1	395	78	3.4	9.5
CZVI(Hg+Se)	3	7.6	-390	64	0.40	7.0
	6	7.7	-375	41	0.31	5.7
	12	7.7	-385	54	0.18	3.3
	24	7.8	-385	29	0.49	2.0
	48	7.6	-300	30	0.20	0.41
	48	7.6	-395	35	0.30	0.87
	48	7.4	-390	38	0.25	0.31
	96	7.6	-305	31	0.23	< 0.08
	192	7.7	-405	19	0.22	< 0.08
	192	7.6	-400	19	0.28	< 0.08
	192	7.6	-395	22	n/a	< 0.08
INP(Se)	3	9.0	-455	80	n/a	10.6
	192	7.9	-390	66	n/a	10.4
	384	7.9	285	63	n/a	10.4
CZVI(Se)	3	8.0	-400	63	n/a	7.0
	6	8.0	-405	52	n/a	5.8
	12	7.9	-400	43	n/a	2.0
	24	7.8	-400	40	n/a	n/a
	48	7.7	-400	45	n/a	0.47
	48	7.8	-400	43	n/a	0.43
	48	7.6	-405	47	n/a	0.61
	96	7.6	-380	29	n/a	0.06
	192	7.7	-410	17	n/a	0.09
	192	7.6	-405	20	n/a	n/a
	192	7.6	-410	24	n/a	n/a
	384	7.8	-355	4	n/a	0.10

n/a = not analyzed; Alk = alkalinity (mg L^{-1} $CaCO_3$)

Table C.2 Summary of general chemistry and mercury concentrations from treatment experiments with bulk treatment material.

sample	time (d)	pH	Eh (mV)	mg L^{-1}	
				Alk ($CaCO_3$)	Hg
INP(1)	0	8.7	350	82	1.8
	8	8.6	390	78	2.2
GAC	8	8.8	-5	83	0.38
Cu+S	8	8.1	-395	80	0.18
QMP+S	8	7.6	-370	70	0.11
INP(2)	0	8.8	550	67	8.0
	8	7.5	435	65	6.9
ATP	8	8.2	395	37	4.9
ATP+amino	8	6.8	85	143	2.2
ATP+dimercapto	8	6.8	125	75	0.03

Alk = alkalinity (mg L^{-1} $CaCO_3$)

Table C.3 Summary of QA/QC from the treatment experiments with Hg(II) in the presence of Connelly Fe^0. Data were obtained from a Tekran Model 2500 cold vapour atomic fluorescence spectrophotometer (CV-AFS).

date	label	actual Hg concentration (ng L^{-1})	reported Hg concentration (ng L^{-1})	% recovery	N	%RSD
10/01/2009	MDL	-	0.7	-	-	-
	MQL	-	2	-	-	-
	blank	-	< 0.7	-	23	20
	Std1	0.5	0	498[a]	3	103
	Std2	1	1	137[a]	3	15
	Std3	2	2	81	3	37
	Std4	5	5	92	3	4
	Std5	10	12	87	3	2
	Std6	25	29	85	3	2
	Std7	50	60	83	3	1
	Std8	100	120	83	3	1
11/29/2009	MDL	-	0.8	-	-	-
	MQL	-	3	-	-	-
	blank	-	0.2	-	13	135
	Std1	0.5	0	147[a]	1	-
	Std2	1	1	73[a]	2	35
	Std3	2	2	94	2	14
	Std4	5	5	102	2	6
	Std5	10	9	105	2	5
	Std6	25	24	105	2	2
	Std7	50	45	111	2	3
	Std8	100	88	113	2	1

[a] recovery out of range (75 – 125%), standards not included in calibration curve; MDL = method detection limit; MQL = method quantitation limit; N = number of samples; %RSD = relative standard deviation

Table C.4 Summary of QA/QC from the treatment experiments with Hg(II) in the presence of bulk treatment materials. Data were obtained from a Tekran Model 2500 cold vapour atomic fluorescence spectrophotometer (CV-AFS).

date	label	actual Hg concentration (ng L^{-1})	reported Hg concentration (ng L^{-1})	% recovery	N	%RSD
11/02/2009	MDL	-	1.3	-	-	-
	MQL	-	4	-	-	-
	blank	-	< 1.3	-	19	141
	Std1	0.5	< 1.3	194[a]	2	-
	Std2	1	1	105	3	3
	Std3	2	2	110	3	5
	Std4	5	5	97	3	7
	Std5	10	11	94	3	8
	Std6	25	26	95	3	7
	Std7	50	53	94	3	9
	Std8	100	108	92	3	6
03/15/2010	MDL	-	0.9	-	-	-
	MQL	-	3	-	-	-
	blank	-	1.2	-	22	25
	Std1	0.5	< 0.9	151[a]	1	-
	Std2	1	1	93	2	6
	Std3	2	2	103	2	5
	Std4	5	5	101	2	6
	Std5	10	10	99	2	6
	Std6	25	24	103	2	6
	Std7	50	50	101	2	6
	Std8	100	99	101	2	7

[a] recovery out of range (75 – 125%), standards not included in calibration curve; MDL = method detection limit; MQL = method quantitation limit; N = number of samples; %RSD = relative standard deviation

Table C.5 Summary of QA/QC data for the Se 206.3 nm optical emission line obtained from Thermo iCAP 6000 (ICP-OES).

label	actual Se concentration (mg L^{-1})	reported Se concentration (mg L^{-1})	% recovery
MDL	-	0.08	-
MQL	-	0.27	-
blank	0	< 0.08	-
Std1	1	1.0	103
Std2	5	5.1	102
Std3	10	10.0	100
Std4	15	14.9	99
Std5	25	25.0	100

MDL = method detection limit; MQL = method quantitation limit

Table C.6 Extended X-ray absorption fine structure analysis of mercury and selenium reference standards.

sample	scatterer	CN	r_{eff} [Å]	R [Å]	S_0^2	σ^2 [Å^2]	ΔE [eV]	R factor
$HgCl_2$	Hg-Cl	2.0	2.29	2.29 ± 0.01	1.00 ± 0.09	0.004	9.0 ± 1.0	0.05
HgO	Hg-O1	1.0	2.04	2.01 ± 0.04	1.04 ± 0.37	0.008	9.0 ± 4.1	0.06
	Hg-O2		2.07	2.04 ± 0.04				
α-HgS	Hg-S	2.0	2.37	2.36 ± 0.01	0.77 ± 0.09	0.001	8.1 ± 1.3	0.05
β-HgS	Hg-S	4.0	2.54	2.44 ± 0.02	0.56 ± 0.08	0.003[a]	-9.1 ± 4.8	
	Hg-O1	1.0	2.04	2.00 ± 0.03	1.10 ± 0.21	0.003[a]	1.1 ± 4.8	0.07
	Hg-O2		2.07	2.03 ± 0.03				
HgSe	Se-Hg	4.0	2.63	2.60 ± 0.01	0.62 ± 0.07	0.007	2.0 ± 0.6	0.03
	Se-Se	12.0	4.30	4.29 ± 0.05	0.49 ± 0.38	0.020	6.5 ± 1.7	
Se^0	Se-Se	2.0	2.37	2.38 ± 0.01	1.11 ± 0.18	0.004	6.5 ± 1.7	0.04

[a] values fixed during structure modeling; CN = coordination number; r_{eff} = actual bond length; R = modeled bond length; S_0^2 = passive electron reduction factor; σ^2 = mean-square displacement of bond length; R factor = fitting statistic

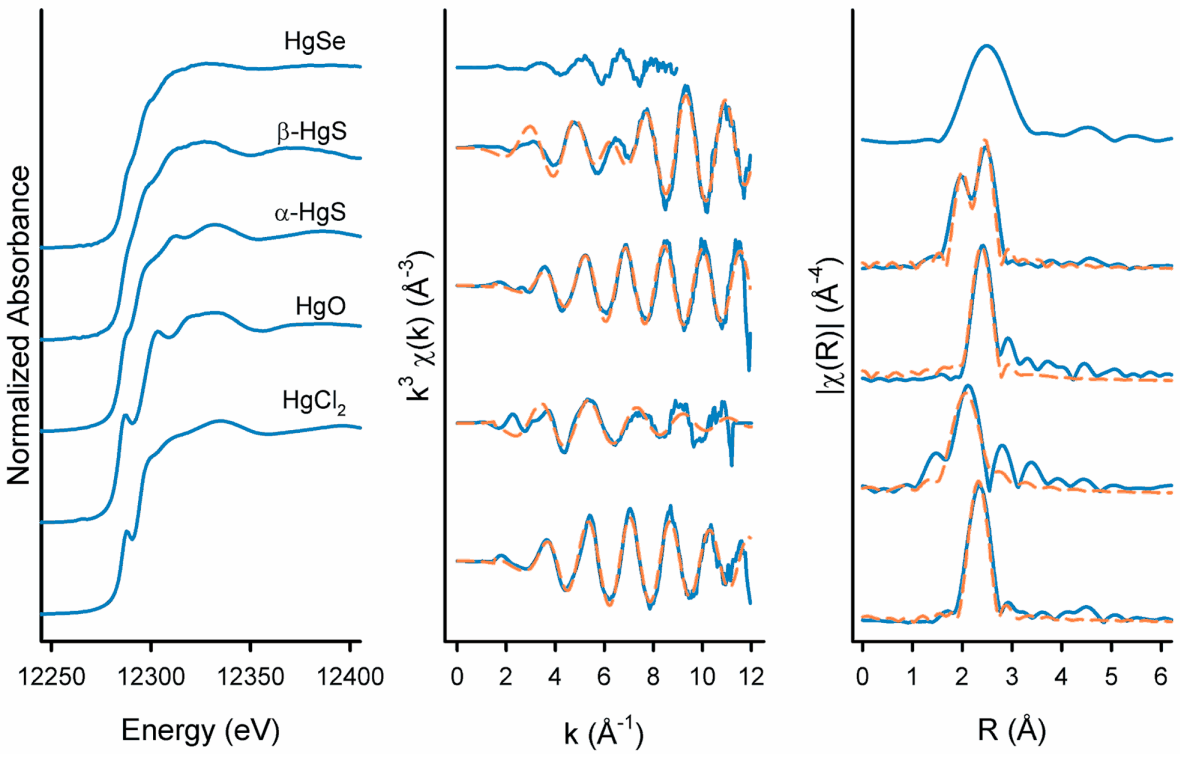

Figure C.1 Plot of measured (solid, blue line) and modeled (dashed, orange line) XANES and EXAFS data for the Hg reference materials.

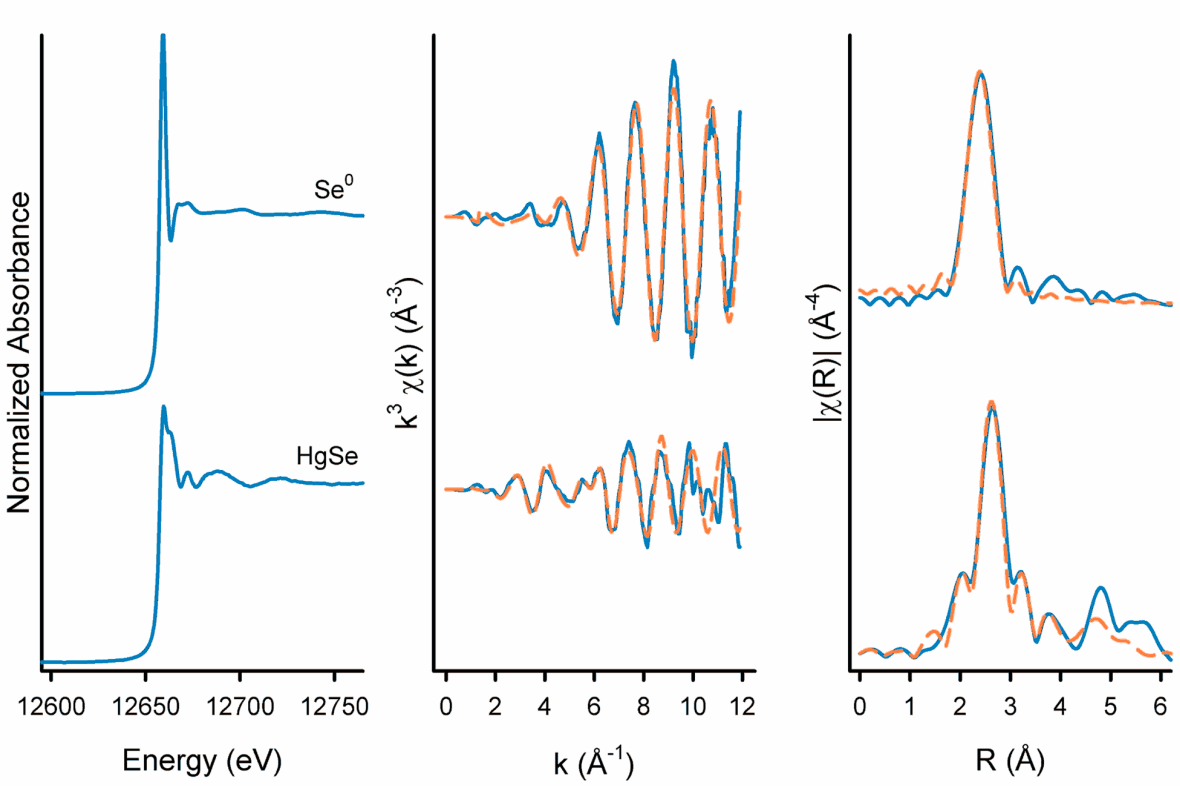

Figure C.2 Plot of measured (solid, blue line) and modeled (dashed, orange line) XANES and EXAFS data for the Se reference materials.

Appendix D:

Summary of Data Presented in Chapter 5

Derivation of Equations

The equations used to calculate the individual rates of sulfate reduction ($^{32}k_s$ for ^{32}S and $^{34}k_s$ for ^{34}S) are derived as follows:

Derivation of Equation (5.15)

(1) $$\frac{^{34}k_s}{^{32}k_s} = \alpha_k \, ^{34}R_S$$

(2) $$k_{eff} = {}^{34}k_s + {}^{32}k_s$$

(3) $$^{32}k_s = k_{eff} - {}^{34}k_s$$

(4) $$^{34}k_s = {}^{32}k_s \cdot \alpha_k \cdot {}^{34}R_S$$

(5) $$^{34}k_s = \left(k_{eff} - {}^{34}k_s\right) \cdot \alpha_k \cdot {}^{34}R_S$$

(6) $$^{34}k_s = k_{eff} \cdot \alpha_k \cdot {}^{34}R_S - {}^{34}k_s \cdot \alpha_k \cdot {}^{34}R_S$$

(7) $$^{34}k_s + {}^{34}k_s \cdot \alpha_k \cdot {}^{34}R_S = k_{eff} \cdot \alpha_k \cdot {}^{34}R_S$$

(8) $$^{34}k_s\left(1 + \alpha_k \cdot {}^{34}R_S\right) = k_{eff} \cdot \alpha_k \cdot {}^{34}R_S$$

(9) $$^{34}k_s = \frac{k_{eff} \cdot \alpha_k \cdot {}^{34}R_S}{1 + \left(\alpha_k \cdot {}^{34}R_S\right)}$$

(10) $$^{34}k_s = \frac{k_{eff}}{1 + \left(\frac{1}{\alpha_k \cdot {}^{34}R_S}\right)}$$

Derivation of Equation (5.16)

(1) $$\frac{{}^{34}k_s}{{}^{32}k_s} = \alpha_k \, {}^{34}R_S$$

(2) $${}^{32}k_s = \frac{{}^{34}k_s}{\alpha_k . {}^{34}R_s}$$

(3) $${}^{32}k_s = \frac{\left(k_{eff} - {}^{32}k_s\right)}{\alpha_k . {}^{34}R_s}$$

(4) $${}^{32}k_s \cdot \alpha_k . {}^{34}R_s = k_{eff} - {}^{32}k_s$$

(5) $${}^{32}k_s + {}^{32}k_s \cdot \alpha_k . {}^{34}R_s = k_{eff}$$

(6) $${}^{32}k_s \left(1 + \alpha_k . {}^{34}R_s\right) = k_{eff}$$

(7) $${}^{32}k_s = \frac{k_{eff}}{1 + \left(\alpha_k . {}^{34}R_s\right)}$$